Własności fizyczne i kwantowe przejścia fazowe w układach silnie skorelowanych elektronów w ramach ścisłej diagonalizacji połączonej z obliczeniami *ab initio*

Adam Rycerz

Rozprawa doktorska
Promotor: Prof. dr hab. Józef Spałek

Uniwersytet Jagielloński
Instytut Fizyki im. Mariana Smoluchowskiego
Zakład Teorii Materii Skondensowanej

Kraków, maj 2003

Physical properties and quantum phase transitions in strongly correlated electron systems from a combined exact diagonalization – *ab initio* approach

ADAM RYCERZ

Ph.D. Thesis
under the supervision of
Prof. Józef Spałek

Jagiellonian University
Marian Smoluchowski Institute of Physics
Condensed Matter Theory Department

Kraków, May 2003

Abstract

We describe and implement the recently proposed approach combining *exact diagonalization* in the Fock space with an *ab initio* method (EDABI). Namely, we apply it to the description of correlated nanochains, fermionic ladders, and clusters. In particular, the microscopic parameters are determined and the evolution of the system properties is traced in a systematic manner as a function of the interatomic distance. Both ground–state and dynamical correlation functions are discussed within a single scheme. The principal physical results of the thesis are: (i) the appearance of the metallic and insulating features for a *one–dimensional* nanochain in the *half–filled* band case, (ii) the transformation from *highly–conducting* nanometal to the charge–ordered nanoinsulator away from the half–filling; (iii) an absolute stability of the hydrogen molecular clusters and ladders, and (iv) the molecule disintegration for the large densities; (v) the presence of the *dielectric catastrophe* for the fermionic ladder when the system crosses over from the band to the Mott–Hubbard insulating state. The analysis is performed using the Gaussian $1s$–like basis and includes *long–range* Coulomb interactions.

Contents

Acknowledgments

I would like to express my gratitude to Prof. Józef Spałek for directing the work, establishing the method of approach (EDABI), and for many discussions. I also thank to Profs. Peter Prelovšek (Ljubljana), Fakher F. Assaad (Stuttgart) and Yuri A. Izyumov (Yekaterinburg) for informative discussions during the conference SCES '2002 (Kraków) and VII Training Course in Vietri sul Mare (Italy). Discussions with Prof. Krzysztof Rościszewski and my colleagues: Marcin Mierzejewski, Maciej Maśka, Jan Kurzyk, Robert Podsiadły, and Marcin Raczkowski are appreciated.

The work was partly supported by the Committee for Scientific Research (KBN) of Poland, Grant Nos. 2 P03B 064 22 and 2 P03B 050 23. The support from the Foundation for Polish Science (FNP) is also acknowledged.

Chapter 1

Introduction

The theoretical understanding of the electrical and mechanical properties of nanometer–scale systems containing $N = 1 \div 100$ atoms is crucial from the two principal prospectives.

First, as the size of microelectronic devices continues to shrink, interest is focused on the nature of electron transport through essentially one–dimensional devices, such as nanowires and quantum point contacts, with properties that are qualitatively different from those of larger size. For instance, it has been discovered five years ago, that the gold nanowires evolve spontaneously into chains of single atoms (Yanson, Rubio Bollinger, van der Brom, Agraït and van Ruitenbeek, 1998; Ochnishi, Kondo and Takayanagi, 1998), which are surprisingly stable, have nearly ideal quantum values of the conductance $2e^2/h$ (≈ 12.9 kΩ^{-1}), and are able to sustain enormous current densities. Similar properties are present in all the $5d$ noble metals, such as Ir, Pt, and Au, but absent in the corresponding elements of the $4d$ series: Rh, Pd, and Ag (Smit, Untiedt, Yanson and van Ruitenbeek, 2001). Although the formation of freely suspended chains of atoms by itself has been explained within density functional theory calculations by Bahn and Jacobsen (2001), the theoretical understanding of electron–transport aspects of this phenomena is still lacking. The latter problem is studied with particular interest for Na nanowires formed on surface (Tsukamoto and Kikuji, 2002; Ahn, Kim, Lee, Hwang, Kim and Yeom, 2002). This is because such nanowire is expected to be treated as the s–band system having the simplest electronic structure characteristic for a monovalent atom. Elaborate investigations on electron–transport properties of s–band nanowires are, however, not common as yet: only a few experiment have been reported (Krans, van Ruitenbeek, Fisun, Yanson and de Jongh, 1995; Yanson, Yanson and van Ruitenbeek, 1999).

Second, it is important to determine the electronic structure of such small systems to see the evolution from the collection of atoms to a piece of a solid with the delocalized (*Bloch–type* or *Fermi–liquid–like*) states. The latter aspect opens up few separate problems for further investigations such as the presence of specific one–dimensional excitations (*holons* and *spinons*), the appearance of the *Peierls distortion*, and of the *Tomonaga–Luttinger liquid* behavior (Fisher and Glazman, 1997).

In this thesis we apply a novel method of approach (EDABI) developed in our group recently (Spałek, Podsiadły, Wójcik and Rycerz, 2000; Rycerz and Spałek, 2001; Spałek, Görlich, Rycerz, Zahorbeński, Podsiadły and Wójcik, 2003), in which we combine the *exact diagonalization* providing us with a rigorous treatment of interparticle interaction, with an *ab–initio* optimization of a single–particle wave function in the interacting–system ground state. In this manner, the interaction and the single–particle terms in the Hamiltonian are treated on the same footing. Hence, the method is particularly useful for strongly correlated systems, when the kinetic (band) energy of electrons propagating throughout the system is at best comparable to the interaction among those particles. Two other examples of systems when the interaction among particles dominates are the *high–temperature superconductors* and two–dimensional electron liquid with the *fractional quantum Hall effect*.

The major part of the thesis contains a numerical study of correlated atomic chains and ladders containing up to $N = 16$ atoms, with periodic (or antiperiodic) boundary conditions, and includes also the *long–range* part of the Coulomb interaction. Such nanoscopic systems are interesting objects of study for few reasons. First of all, the role of long–range Coulomb interaction in 1D is crucial, as the charge screening becomes less effective (Hubbard, 1978; Kondo and Yamai, 1977; Ovchinnikov, 1993). The exact solutions of the parametrized models with inclusion of intersite interactions (Strack and Vollhardt, 1993; Arachea and Aligia, 1994; Michielsen, De Raedt and Schneider, 1992) prove the existence of the metal–insulator transition (MIT) for the half–filled band case, in contradistinction to the Hubbard model solution (Lieb and Wu, 1968). The existence of such MIT has also been discussed by Daul and Noack (2000) within the density–matrix renormalization group (DMRG) method when the second–neighbor hopping is included. A separate question concerns the appearance of the Tomonaga–Luttinger behavior (Schulz, 1993; Voit, 1995) in the metallic state, for which some evidence has been gathered (Dardel, Malterre, Grioni, Weibel, Baer, Voit and Jérôme, 1992; Sekiyama, Fujimori, Aonuma, Sawa and Kato, 1995). *Last but not least*, the questions of the metallicity appearance in a correlated nanoscopic atomic chain or ring and that concerning the applicability of the concept of *Mott insulator* in the situation when the separation between the quasiparticle states (in a finite system) is of the same order of magnitude as the Hubbard gap, must be addressed separately. Similar problems are encountered in the weak–coupling renormalization group (RG) analysis (Fabrizio, 1996), which predicts that *umklapp* processes lead any half–filled 1D system with two Fermi points to an insulating state.

This is the reason for discussing in detail here a rigorous numerical evidence for the transition from a nanometal to the localized spin system. The analysis is performed separately for correlated atomic ladders, for which 4 Fermi points in principle allow the system metallicity even for short–range interactions (Voit, 1995), and the transformation from band to Mott insulator introduce a new phenomena known as *dielectric catastrophe* (Resta and Sorella, 1999; Aebisher, 2001).

1.1 Aim and scope of the thesis

The structure of the thesis is as follows. In the next Chapter we summarize briefly the method of approach as developed by (Spałek et al., 2000) and discuss its relation to multiconfiguration–interaction (MCI) approach from quantum chemistry. The Lanczos method for the Hamiltonian diagonalization in the Fock space is also presented. The particular emphasis is put on calculation of the dynamical properties such as the spectral function or the optical conductivity. In Chapter 3 we provide the numerical study of 1D chains with long–range Coulomb interactions, close to the metal–insulator transition. The role of boundary conditions for a finite system is also discussed. In Chapter 4 the stability of hydrogen molecules in 3D cluster is analyzed, the implications for hydrogen metallicity are briefly discussed. Finally, in Chapter 5, we present the results for the correlated ladders and the evidence for the dielectric catastrophe in that system.

The main feature of the above analysis is to provide the properties as a function of the lattice spacing. In this respect, our approach differs from numerous solutions of the parametrized models such as the (extended) Hubbard model, where the physical properties are discussed as a function of the model parameters. In this manner we can trace the evolution of the system properties systematically, since we change the interatomic distance continuously. We also complement our previous study of a correlated atomic chain (Spałek and Rycerz, 2001; Rycerz and Spałek, 2002) with an analysis performed systematically in the Gaussian $1s$–like basis (defined in Appendix A). The results concerning transport properties of 1D chain (Chapter 3), as well as all the data for H_4 cluster and those for the correlated fermionic ladders (Chapters 4 and 5, respectively) have not been published as yet.

Chapter 2

Numerical methods

In the first part of this Chapter we summarize our method of approach to the strongly correlated electron systems that combines the first– and the second–quantization scheme (Spałek et al., 2000). In the second part (Section 2.2) we recapitulate briefly the Lanczos algorithm for finding the ground state in the Fock space and its version for calculating dynamical properties, following mainly Jaklič and Prelovšek (2000) and Dagotto (1994). We also provide (in Section 2.2.3) brief overview of other numerical methods for correlated electrons and their relation to the Lanczos method.

2.1 The exact diagonalization – *ab initio* (EDABI) method

It is generally perceived that the wave mechanics (Schrödinger, 1926) (hereinafter called the first–quantization scheme) describes the matter–wave aspect of the system behavior, whereas the second–quantization scheme (Fock, 1957; Mahan, 1990) restores the particle language as it operates with the particle transitions (creations and annihilations) between the states with well defined quantum numbers appropriate for a complete set of single particle states. Obviously, a complete description of the physical system relies on *complementarity* of both descriptions of the quantum states. The question we have addressed (Spałek et al., 2000; Rycerz and Spałek, 2001; Spałek, Görlich, Rycerz and Zahorbeński, 2003) in this respect is whether one can combine both first– and the second–quantization schemes in approaching the many–particle systems, possibly in a systematic manner, which would represent a nonperturbational description of many–body as well as the complementary aspects of N–particle states.

The idea of exact diagonalization — *ab initio* (EDABI) approach is illustrated on the block–diagram exhibited in Figure 2.1. We start from choosing the initial

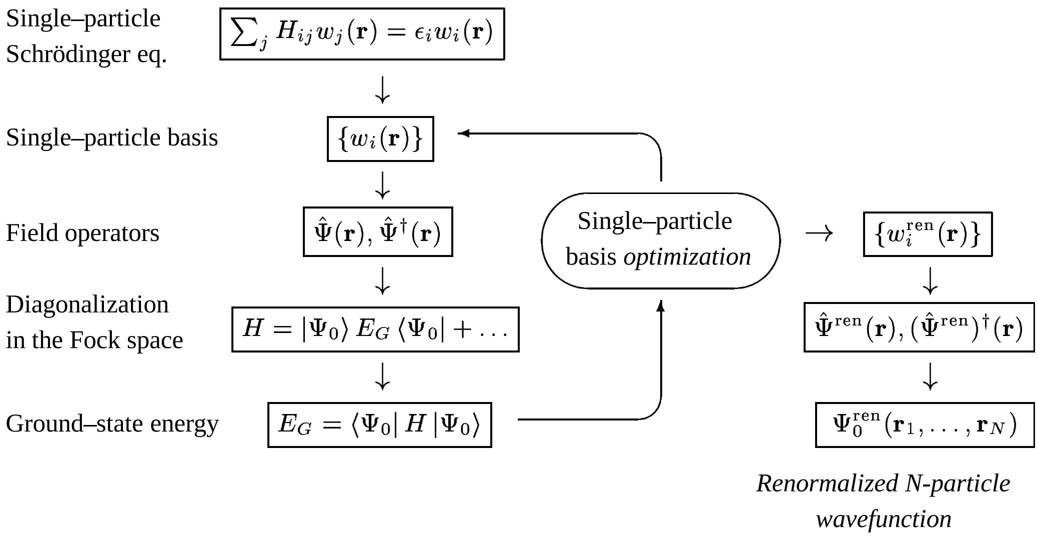

FIGURE 2.1: Flowchart diagram of the exact diagonalization *ab–initio* (EDABI) method. The part on the far right provides *renormalized* Wannier functions $\{w_i(\mathbf{r})\}$, field operators, as well as the N–particle wavefunction.

Wannier basis set $\{w_i(\mathbf{r})\}$, composed of orthogonalized atomic–like wavefunctions. Next, we write down the system Hamiltonian in the second–quantization form and determine the ground–state energy E_G and the corresponding state $|\Psi_0\rangle$ by e.g. Lanczos procedure (*cf.* Section 2.2) for the fixed basis $\{w_i(\mathbf{r})\}$. Then, the Wannier basis set $\{w_i(\mathbf{r})\}$ is optimized with respect to the inverse orbital size α, characterizing the atomic wave functions composing $w_i(\mathbf{r})$, until the minimal ground–state energy E_G is reached (see *below*) for given lattice parameter a. Operationally, the basis functions $\{w_i(\mathbf{r})\}$ are coded in the microscopic parameters of the Hamiltonian in the second–quantized form. Those parameters are determined, in turn, for a given interatomic distance a and the inverse orbital size α. We repeat the diagonalization for given a by varying α until the global minimum of E_G is achieved. The whole procedure is repeated for all the values of a under consideration, thus providing the system evolution as a function of the interatomic distance a.

2.1.1 The renormalized wave equation

In approaching a nonrelativistic system of interacting electrons in a single band we start from Hamiltonian in the Fock space, expressed in the form

$$H = \sum_\sigma \int d^3\mathbf{r} \widehat{\Psi}_\sigma^\dagger(\mathbf{r}) T(\mathbf{r}) \widehat{\Psi}_\sigma(\mathbf{r})$$

$$+\frac{1}{2}\sum_{\sigma_1\sigma_2}\int\int d^3\mathbf{r}_1 d^3\mathbf{r}_2 \widehat{\Psi}^\dagger_{\sigma_1}(\mathbf{r}_1)\widehat{\Psi}^\dagger_{\sigma_2}(\mathbf{r}_2)V(\mathbf{r}_1-\mathbf{r}_2)\widehat{\Psi}_{\sigma_2}(\mathbf{r}_2)\widehat{\Psi}_{\sigma_1}(\mathbf{r}_1), \tag{2.1}$$

where $T(\mathbf{r})$ and $V(\mathbf{r}_1-\mathbf{r}_2)$ are, respectively, the Hamiltonians for a single particle and a single pair of particles in the coordinate (Schrödinger) representation, and $\widehat{\Psi}_\sigma(\mathbf{r})$ is the field operator defined through

$$\widehat{\Psi}_\sigma(\mathbf{r}) = \sum_i w_i(\mathbf{r})\chi_\sigma a_{i\sigma}, \tag{2.2}$$

where $a_{i\sigma}$ is the annihilation operator of particle in a single–particle state $w_i(\mathbf{r})\chi_\sigma$. One should note that the basis $\{w_i(\mathbf{r})\chi_\sigma\}$ is completely arbitrary at this point. By substituting (2.2) into (2.1) we obtain the usual form of the Hamiltonian

$$H = \sum_{ij\sigma} t_{ij} a^\dagger_{i\sigma}a_{j\sigma} + \frac{1}{2}\sum_{ijkl\sigma\sigma'} V_{ijkl}a^\dagger_{i\sigma}a^\dagger_{j\sigma'}a_{l\sigma'}a_{k\sigma}, \tag{2.3}$$

with the microscopic parameters defined by

$$t_{ij} \equiv \langle w_i|\, T\, |w_j\rangle = \int d^3\mathbf{r}\, w_i^*(\mathbf{r})T(\mathbf{r})w_j(\mathbf{r}), \tag{2.4}$$

and

$$V_{ijkl} \equiv \langle w_i w_j|\, V\, |w_k w_l\rangle = \int d^3\mathbf{r}_1 d^3\mathbf{r}_2 w_i^*(\mathbf{r}_1)w_j^*(\mathbf{r}_2)V(\mathbf{r}_1-\mathbf{r}_2)w_k(\mathbf{r}_1)w_l(\mathbf{r}_2). \tag{2.5}$$

Thus, in the form (2.3) of the many–particle Hamiltonian, the single– and many–particle aspects of the problem are separated in the sense that calculation of the parameters t_{ij} and V_{ijkl}, both containing the single–particle basis $\{w_i(\mathbf{r})\}$, is separated from the diagonalization procedure of the Hamiltonian in the Fock space. The origin of this two–level procedure can be seen explicitly when we calculate the system ground state energy

$$E_G \equiv \langle H\rangle = \sum_{ij\sigma} t_{ij}\langle a^\dagger_{i\sigma}a_{j\sigma}\rangle + \frac{1}{2}\sum_{ijkl\sigma\sigma'} V_{ijkl}\langle a^\dagger_{i\sigma}a^\dagger_{j\sigma'}a_{l\sigma'}a_{k\sigma}\rangle, \tag{2.6}$$

where the averaging $\langle\ldots\rangle$ for the ground state $|\Phi_G\rangle$ takes place over *all* possible occupancies of single–particle states $|i\sigma\rangle$, $|j\sigma'\rangle$, $|k\sigma\rangle$, and $|l\sigma'\rangle$, for *fixed* values of t_{ij} and V_{ijkl} regarded usually as parameters. When considering the grand canonical ensemble, one have to diagonalize $H-\mu N$, with

$$N = \int d^3\mathbf{r}\,\widehat{\Psi}^\dagger(\mathbf{r})\widehat{\Psi}(\mathbf{r}) = \sum_{ij\sigma}\int d^3\mathbf{r}\, w_i^*(\mathbf{r})w_j(\mathbf{r})\langle a^\dagger_{i\sigma}a_{j\sigma}\rangle. \tag{2.7}$$

To close the solution we treat the expression (2.6) as a functional $\{w_i(\mathbf{r})\}$. In the most general case of the grand canonical ensemble and with a nonorthogonal basis $\{w_i(\mathbf{r})\}$ this functional can be written as

$$\mathcal{F}\left[w_i(\mathbf{r})\right] = E_G\left[w_i(\mathbf{r})\right] - \sum_{ij\sigma}(\mu + \lambda_{ij}) \int d^3\mathbf{r} w_i^*(\mathbf{r}) w_j(\mathbf{r}) \langle a_{i\sigma}^\dagger a_{j\sigma} \rangle. \tag{2.8}$$

In effect, the Lagrange–Euler equation, which plays the role of the stationary *renormalized wave equation* for $w_i(\mathbf{r})$, takes the form

$$\frac{\delta E_G}{\delta w_i^*(\mathbf{r})} - \nabla \cdot \frac{\delta E_G}{\delta \nabla w_i^*(\mathbf{r})} - \sum_{i \leqslant j, \sigma} (\lambda_{ij} - \mu) w_j(\mathbf{r}) \langle a_{i\sigma}^\dagger a_{j\sigma} \rangle = 0, \tag{2.9}$$

where λ_{ij} and μ play the role of Lagrange multipliers (if we use explicitly orthogonal basis and particle–conserving diagonalization procedure in the Fock space, then $\lambda_{ij} = \mu \equiv 0$ and Eq. (2.9) reduces to the usual Euler equation). Also, when the class of $\{w_i(\mathbf{r})\}$ is selected variationally (as in the following), Eq. (2.8) is then minimized with respect to trial function parameters (e.g. inverse orbital size α in the case when the orthogonal basis $w_i(\mathbf{r})$ is composed of superposed atomic–like wave functions).

2.1.2 Relation to MCI method

With the help of the field operator $\widehat{\Psi}(\mathbf{r}) = \sum_{i\sigma} w_i(\mathbf{r}\chi_\sigma)$ we can define ground–state N–particle wave function as $\Psi_0(\mathbf{r}_1, \ldots, \mathbf{r}_N) = \langle 0 | \widehat{\Psi}(\mathbf{r}_1) \ldots \widehat{\Psi}(\mathbf{r}_N) | \Psi_0 \rangle$ where $|\Psi_0\rangle$ is the N–particle ground state state in the Fock space

$$|\Psi_0\rangle = \frac{1}{\sqrt{N!}} \sum_{k_1 \ldots k_N} C_{k_1 \ldots k_N} a_{k_1}^\dagger \ldots a_{k_N}^\dagger |0\rangle \tag{2.10}$$

and $C_{k_1 \ldots k_N}$ are the expansion coefficients (note that: $k \equiv j\sigma$). Within our method we determine $C_{k_1 \ldots k_N}$ with the help of Lanczos algorithm (see next Section), whereas in the framework of *multiconfigurational–interaction* (MCI) method the $C_{k_1 \ldots k_N}$ coefficients are optimized variationally (Shavitt, 1977). Using the decomposition of $\widehat{\Psi}(\mathbf{r})$ in terms of $\{w_i(\mathbf{r})\}$ we obtain that

$$\Psi_0(\mathbf{r}_1, \ldots, \mathbf{r}_N) = \frac{1}{\sqrt{N!}} \sum_{k_1 \ldots k_N} C_{k_1 \cdots k_N} \mathcal{A}\left[w_{k_1}(\mathbf{r}_1) \ldots w_{k_N}(\mathbf{r}_N)\right], \tag{2.11}$$

where $\mathcal{A}$ is the antisymmetrizer. Therefore, if we are able to perform the diagonalization in the Fock space, we have an exact many–particle wave function within the subspace selected by the single–particle basis $\{w_i(\mathbf{r})\}$. This aspect of the whole problem will be explored in detail elsewhere (Spałek, Görlich, Rycerz and Zahorbeński, 2003).

2.1.3 Methodological remark: A meaning of EDABI method

A principal methodological remark is in place here (J. Spałek, private communication). The definition (2.2) of the field operator is *independent* of the basis $\{w_i(\mathbf{r})\}$ selected to represent it in the occupation–number representation provided it is *complete* in the quantum–mechanical sense. This independence on the choice of $\{w_i(\mathbf{r})\}$ is seen clearly from the circumstance that the fundamental anticummutation relations for the field operators $\widehat{\Psi}_\sigma(\mathbf{r})$ and $\widehat{\Psi}^\dagger_\sigma(\mathbf{r})$, which are

$$\begin{gathered}
\widehat{\Psi}_\sigma(\mathbf{r})\widehat{\Psi}^\dagger_{\sigma'}(\mathbf{r}') + \widehat{\Psi}^\dagger_{\sigma'}(\mathbf{r}')\widehat{\Psi}_\sigma(\mathbf{r}) = \delta^{(d)}(\mathbf{r}-\mathbf{r}')\delta_{\sigma\sigma'}, \\
\widehat{\Psi}_\sigma(\mathbf{r})\widehat{\Psi}_{\sigma'}(\mathbf{r}') + \widehat{\Psi}_{\sigma'}(\mathbf{r}')\widehat{\Psi}_\sigma(\mathbf{r}) = 0, \\
\widehat{\Psi}^\dagger_\sigma(\mathbf{r})\widehat{\Psi}^\dagger_{\sigma'}(\mathbf{r}') + \widehat{\Psi}^\dagger_{\sigma'}(\mathbf{r}')\widehat{\Psi}^\dagger_\sigma(\mathbf{r}) = 0,
\end{gathered} \tag{2.12}$$

are indeed independent of the basis and determine, together with the Heisenberg equation of motion

$$i\hbar\frac{\partial}{\partial t}\widehat{\Psi}_\sigma(\mathbf{r}) = \left[\widehat{\Psi}_\sigma(\mathbf{r}), H\right], \tag{2.13}$$

whole dynamics of the system. Obviously, Eq. (2.13) is *insoluble* in a general in a general case, as it represents a nonlocal operator equation for $\widehat{\Psi}_\sigma(\mathbf{r})$ (in actual calculations for an infinite basis, Eq. (2.13) should be supplemented with that for $\widehat{\Psi}^\dagger_\sigma(\mathbf{r})$, which makes the matter even worse). This is the reason why we have selected the two–step approach: A diagonalization of the Hamiltonian in the occupation–number representation followed by readjustment of $\{w_i(\mathbf{r})\}$ in the correlated state.

As said above, the definition of $\widehat{\Psi}_\sigma(\mathbf{r})$ requires the basis completness. In most parametrized models of interacting fermions the summation in Eq. (2.2) is limited to *incomplete* sets (one–, two–, three–band models, etc.). In practice, we select subset of L states to define $\widehat{\Psi}_\sigma(\mathbf{r})$. Under these circumstances, one can ask if there is a way to define the truncated basis $\{w_i(\mathbf{r}), i = 1 \ldots L\}$ in the *optimal* manner. The second step in our approach is the basis optimization and represents an original contribution of our group to the many–body approach in the general sense. Obviously, such set of formal ideas requires either analytical or numerical tools to be implemented when analyzing concrete physical problems and models; these are discussed next.

2.2 Lanczos technique for correlated electrons

The development of computational methods for strongly correlated electron systems was stimulated by the scarity of well–controlled analytical approaches. In 1D variety of models were solved by Bethe Ansatz (Ha, 1996). However, even the calculation basic ground–state properties for the Hubbard model (Hubbard, 1963), such as electron momentum distribution, involves intensive numerical computations and have been done only recently (Ogata and Shiba, 1990; Sorella, Parola, Parrinello and Tosatti, 1990). A few exactly solvable systems were discussed in the framework of EDABI method by Spałek et al. (2000). Conceptually the simplest way to find the ground state in the Fock space is the *exact diagonalization* (ED) method for small systems: having determined all the matrix element of the Hamiltonian $H_{kl} \equiv \langle\phi_k| H |\phi_l\rangle$ for same arbitrary basis $\{|\phi_k\rangle, k = 1 \ldots N_{\rm st}\}$ one can utilize standard numerical procedures for diagonalizing real–symmetric or hermitian matrices (Press, Teukolsky, Vetterling and Flannery, 1992). In the models of correlated electrons, however, one is dealing with the number of basis states $N_{\rm st}$ which grows exponentially with the system size. In the (extended) Hubbard model there are 4 basis states for each lattice sites and therefore, the number of basis states in the N–site system is $N_{\rm st} \propto 4^N$. In the ED of such systems one is representing operator with matrices $N_{\rm st} \times N_{\rm st}$, which are already large for very modest value of N. The present status of high–performance computing is restricted to diagonalization of the matrices with $N_{\rm st} < 10^4$ (Dongarra, Duff and van der Vorst, 1998), so that reachable system sizes are $N \leqslant 10$ for the Hubbard model.

The helpful circumstance is that for the most interesting operators and lattice models only a small portion of matrix elements is nonzero within the local basis. Then, the operators can be represent by sparse matrices with $N_{\rm st}$ rows and at most $f(N)$ nonzero elements in each row, where $f(N)$ is the total number of operator components in the second–quantization representation. For instance, $f(N) \propto N$ in the case of Hubbard model, whereas $f(N) \propto N^4$ for general Hamiltonian of the form (2.3). In this way memory requirements are relaxed, the matrices up to $N_{\rm st} \sim 10^7$ are considered in recent applications (Jaklič and Prelovšek, 2000). Finding eigenvalues and eigenvectors of such large matrices is not possible with the standard algorithms performing full diagonalization (Press et al., 1992). One must instead resort to power algorithms, among which the Lanczos algorithm (Lanczos, 1950; Pettifor and Weaire, 1985) is one of the most widely known. In the next Section we report the procedure of finding the ground–state eigenvector and, in Section 2.2.2, the methods for calculating dynamical properties within the Lanczos algorithm.

2.2.1 The ground–state algorithm

The basic idea of the Lanczos method is that a special basis can be constructed where the Hamiltonian has a tridiagonal representation. This is carried out iteratively, as shown below. First, it is necessary to select an arbitrary vector $|\phi_0\rangle$ in the Fock space of the model being studied. If the Lanczos method is used to obtain the ground state of the model $|\psi_0\rangle$, then it is necessary that the overlap between $|\psi_0\rangle$ and the initial state $|\phi_0\rangle$ be nonzero. If no *a priori* information about the ground state is available, this requirement is usually easily satisfied by selecting an initial state with *randomly* chosen coefficients in the working basis that is being used. If some other information about the ground state is known, like its total momentum and spin, then it is convenient to initiate the iterations with a state already belonging to the subspace having this quantum numbers (and still with random coefficients within this subspace). The randomly–chosen coefficients of the initial vector $|\phi_0\rangle$ are strongly recommended to avoid systematical errors in the resulting ground–state correlation functions.

After $|\phi_0\rangle$ is selected, we define a new vector by applying the Hamiltonian H to the initial state. The resulting vector is split in components parallel to $|\phi_0\rangle$, and $|\phi_1\rangle$ orthogonal to it, respectively,

$$H\,|\phi_0\rangle = a_0\,|\phi_0\rangle + b_1\,|\phi_1\rangle\,. \tag{2.14}$$

Since H is Hermitian, $a_0 = \langle\phi_0|\,H\,|\phi_0\rangle$ is real, while the phase of $|\phi_1\rangle$ can be chosen so that b_1 is also real. In the next step H is applied to ϕ_1,

$$H\,|\phi_1\rangle = b_1'\,|\phi_0\rangle + a_1\,|\phi_1\rangle + b_2\,|\phi_2\rangle\,, \tag{2.15}$$

where $|\phi_2\rangle$ is orthogonal to $|\phi_0\rangle$ and $|\phi_1\rangle$. It follows also $b_1' = \langle\phi_0|\,H\,|\phi_1\rangle = b_1$. Proceeding with the iteration one gets in i–th step

$$H\,|\phi_i\rangle = b_i\,|\phi_{i-1}\rangle + a_i\,|\phi_i\rangle + b_{i+1}\,|\phi_{i+1}\rangle\,, \qquad 1 \leqslant i \leqslant M. \tag{2.16}$$

By stopping the iteration at $i = M$ and putting the last coefficient $b_{M+1} = 0$, the Hamiltonian can be represent in the basis of orthogonal Lanczos functions $\{|\phi_i\rangle\,, i = 0\ldots M\}$ as the tridiagonal matrix

$$H_M = \begin{pmatrix} a_0 & b_1 & 0 & \cdots & 0 \\ b_1 & a_1 & b_2 & & \vdots \\ 0 & b_2 & a_2 & \ddots & 0 \\ \vdots & & \ddots & \ddots & b_M \\ 0 & \cdots & 0 & b_M & a_M \end{pmatrix} \tag{2.17}$$

Such matrix is easily diagonalized using standard numerical routines (Press et al., 1992) to obtain approximate eigenvalues ϵ_j and the corresponding orthonormal eigenvectors $|\psi_j\rangle$,

$$|\psi_j\rangle = \sum_{i=0}^{M} c_i^j \, |\phi_i\rangle \,, \qquad j = 0 \ldots M. \tag{2.18}$$

It is important to realize that $|\psi_j\rangle$ are (in general) not exact eigenfunctions of H, but show a remainder

$$H \, |\psi_i\rangle - \epsilon_j \, |\psi_i\rangle = b_{M+1} c_M^j \, |\phi_{M+1}\rangle \,. \tag{2.19}$$

Therefore, the procedure could be regarded as well–controlled, since the norm of the vector on the right–hand side of Eq. (2.19) can be easily calculated. On the other hand, it is evident from the diagonalization of H_M, that matrix elements

$$\langle\psi_i| \, H \, |\psi_j\rangle = \epsilon_j \delta_{ij}, \qquad i, j = 0 \ldots M \tag{2.20}$$

are exact, with no restriction to the subspace $L_M = \text{span}\{|\phi_i\rangle \,, i = 0 \ldots M\}$. The above identity shows the usefulness of the Lanczos method for calculation of particular matrix elements (see *next* Section).

If in the equation (2.16) $b_{M+1} = 0$, we find a $(M+1)$–dimensional eigenspace where H_M is already an exact representation of H. This inevitably happens when $M = N_{\text{st}} - 1$, but for $M < N_{\text{st}} - 1$ it can only occur if the starting vector is orthogonal to some invariant subspace of H. This usually represent a systematical error in selection of $|\phi_0\rangle$, and should not be the case if the input vector $|\phi_0\rangle$ is random, without any hidden symmetries.

Within the Lanczos algorithm the extreme (the smallest and the largest) eigenvalues ϵ_i, along with their corresponding $|\psi_i\rangle$, are rapidly converging to exact eigenvalues E_i and eigenvectors $|\Psi_i\rangle$. It is quite characteristic that usually (for nondegenerate states) $M = 30 \div 60 \ll N_{\text{st}}$ is sufficient to achieve the convergence to the machine precision of the ground–state energy E_0 and the wavefunction $|\Psi_0\rangle$, from which various static and dynamical properties can be evaluated.

The number of operations needed to perform M Lanczos iterations scales as MN_{st}. Numerically, the Lanczos procedure is subject to roundoff errors, introduced by the finite–precision arithmetics. This problem usually only becomes severve at $M > 100$ (more than needed to get accurate g.s. $|\Phi_0\rangle$) and is seen in the loss of the orthogonality of vectors $|\phi_i\rangle$. It can be remedied by successive reorthogonalization (and normalization) of new states $|\phi_i\rangle$, plagued with errors, with respect to previous ones. However, this procedure requires $\sim M^2 N_{\text{st}}$ operations, and can become computationally more demanding than Lanczos iterations alone. This effect prevent one using the Lanczos method, e.g. to tridiagonalize fully large matrices.

2.2.2 Dynamical response in the ground state

One of the most appealing features of the Lanczos method is that it allows the calculation of *dynamical* properties of a given Hamiltonian (Haydock, Heine and Kelly, 1972; Gagliano and Balseiro, 1987). Before the Maximum Entrophy method (van der Linden, 1995; Jarrel and Gubernatis, 1996) for quantum Monte Carlo technique have been developed, the Lanczos approach was the only reliable technique for evaluating dynamical responses in a controlled way (and for the *frustrated* systems still is). For small systems of $N \lesssim 16$ sites (for Hubbard model) the Lanczos method still remains optimal from the computational point of view.

After $|\Psi_0\rangle$ is obtained, the g.s. dynamic correlation functions can be calculated within the same framework. Let us consider the autocorrelation function

$$C_A(t-t') = -i\,\langle\Psi_0|\,A^\dagger(t)A(t')\,|\Psi_0\rangle = -i\,\langle\Psi_0|\,A^\dagger e^{i(E_0-H)(t-t')}A\,|\Psi_0\rangle\,, \quad (2.21)$$

where A is the operator that we are analyzing (which depends on the actual experimental setup under consideration), $A(t)$ is the Heisenberg representation of A, $|\Psi_0\rangle$ is the ground state of the Hamiltonian H, whose ground–state energy is E_0. Many experiments, like (inverse) photoemission, inelastic neutron scattering, and nuclear magnetic resonance, measure directly the Fourier transform $C_A(\omega)$ of $C_A(t-t')$, which is given by

$$C_A(\omega) = -i\int_0^\infty dt e^{i(\omega+i\eta)t}C_A(t) = \langle\Psi_0|\,A^\dagger\frac{1}{\omega+i\eta+E_0-H}A\,|\Psi_0\rangle\,, \quad (2.22)$$

where ω is the frequency and $\eta > 0$ is the small (real) number introduced in the calculation to shift the poles of the Green's function into the complex plane. Usually, we are interested in calculating the *spectral intensity*, which is defined by

$$I_A(\omega) = -\frac{1}{\pi}\mathrm{Im}C_A(\omega) = -\frac{1}{\pi}\mathrm{Im}\,\langle\Psi_0|\,A^\dagger\frac{1}{\omega+i\eta+E_0-H}A\,|\Psi_0\rangle\,. \quad (2.23)$$

Introducing a complete basis, $\sum_n|\Psi_n\rangle\langle\Psi_n| = 1$ and using the identity

$$\frac{1}{x+i\eta} = P\left(\frac{1}{x}\right) - i\pi\delta(x),$$

valid for $\eta\to 0$ (where x is real, amd P denotes the principal part), we arrive at

$$I_A(\omega) = \sum_n |\langle\Psi_n|\,A\,|\Psi_0\rangle|^2\,\delta(\omega-(E_n-E_0)), \quad (2.24)$$

which is another way of expressing the spectral decomposition of a given operator. $|\Psi_n\rangle$ are selected as eigenvectors of the Hamiltonian with eigenvalues E_n.

In practice, the δ functions are smeared by a finite ϵ, i.e. they are replaced by Lorentzians according to

$$\delta(x) \to \frac{1}{\pi}\frac{\epsilon}{x^2+\epsilon^2}. \tag{2.25}$$

In order to evaluate numerically Eq. (2.24), it is convenient to write down the Hamiltonian in the Lanczos basis $|\phi_i\rangle$ (see *previous* Section), but, instead of starting iterations with a random state, we chose now

$$|\phi_0\rangle = A\,|\Psi_0\rangle \,/\sqrt{\langle\Psi_0|\,A^\dagger A\,|\Psi_0\rangle} \tag{2.26}$$

as an initial configuration. Let us consider, following Fulde (1991), the matrix $(z-H_M)$ and the identity $(z-H_M)(z-H_M)^{-1}=I$, where $z=\omega+i\epsilon+E_0$. The the first–row, first–column element of the matrix $(z-H_M)^{-1}$ corresponds to

$$\langle\phi_0|\,\frac{1}{z-H}\,|\phi_0\rangle\,,$$

which is the quantity we want to study in Eq. (2.23). Using the Cramers rule to invert the matrix $(z-H_M)$, one can easily represent the spectral intensity (2.23) in the continued–fraction form (Haydock et al., 1972)

$$I_A(\omega) = -\frac{1}{\pi}\mathrm{Im}\left(\cfrac{\langle\Psi_0|\,A^\dagger A\,|\Psi_0\rangle}{z-a_0-\cfrac{b_1^2}{z-a_1-\cfrac{b_2^2}{z-a_2-\ldots}}}\right), \tag{2.27}$$

where a_i and b_i are the elements of the tridiagonal matrix H_M, evaluated within the Lanczos algorithm starting from the initial state Eq. (2.26), and the form terminates with $b_{M+1}=0$. Recalling that $z=\omega+i\epsilon+E_0$ and knowing the ground–state energy of the system, we can, for any value of frequency ω and of the width ϵ, obtain the spectral function. From the eigenvalues of the Hamiltonian H_M we can get very accurately the positions of the poles in the spectral function.

In practice, in order to get the dynamical response of a finite cluster it is the best to proceed in two steps. *First*, to run the Lanczos subroutine using Eq. (2.26) as the initial state. It is clear that, with this procedure, we are testing the subspace of the Hilbert space in which we are interested (and which is, in general different from the subspace explored by the ground–state Lanczos procedure, *cf.* Section 2.2.1). Thus, all the states found in the Lanczos step will contribute to the spectral function (there will be $M+1$ poles as M iterations are carried out, assuming that $M+1$ is smaller than the dimension of the subspace being explored). *Secondly,* in order to find the intensity of each pole, it is useful to recall that that any energy *eigenvector* $|\psi_j\rangle$ of the tridiagonal representation of the Hamiltonian H_M can be written as in Eq. (2.18), where now $|\phi_i\rangle$ are the orthonormalized vectors defined in the Lanczos procedure, with $|\phi_0\rangle$ given by Eq. (2.26). Then, it can be easily shown that

$$|\langle\psi_j|\, A\, |\Psi_0\rangle|^2 = \left|c_0^j\right|^2 \langle\Psi_0|\, A^\dagger A\, |\Psi_0\rangle\,, \tag{2.28}$$

and thus the intensity can be can be written in terms of the first component of each eigenvector obtained when the tridiagonal Hamiltonian matrix H_M is diagonalized, i.e.

$$I_A(\omega) \approx \sum_{j=0}^{M} \left|c_0^j\right|^2 \langle\Psi_0|\, A^\dagger A\, |\Psi_0\rangle\, \delta(\omega - (\epsilon_j - E_0)), \tag{2.29}$$

where eigenvalues ϵ_j corresponds to eigenvectors $|\psi_j\rangle$ and different notation is used for the ground–state wavefunction $|\Psi_0\rangle$ and energy E_0 to underline they *may*, in general, belong different subspace of the full Hilbert space.

In summary, the whole procedure simply amounts to a Lanczos run with a very particular initial state. To test the convergence of the procedure, it is generally enough to plot the spectral function with a particular ϵ in Eq. (2.25), and to test by eye how the results evolve with the number of iterations. Other more formal methods to terminate the iterations can also be implemented (Pettifor and Weaire, 1985; Viswanath and Müller, 1990; Viswanath and Müller, 1991).

2.2.3 Relation to other numerical methods

Numerical approaches to strongly correlated electrons predominantly can be divided into two categories: the *Quantum Monte Carlo* (QMC) methods and *exact diagonalization* (ED) methods. As we have already mentioned, in ED methods (e.g. the Lanczos method), the computational effort scales exponentially with the system size N, that limits their applicability to small clusters only. On the other hand, when choosing Lanczos technique, one has to make a very mild assumption about the considered model, since the computational time depends smoothly on the number of terms in the Hamiltonian in local basis, and does not depend at all on the parameter values. This is not the case in QMC, when one can easily cross the border between the sign–free and sign–plagued problems. For this reason, the Lanczos method remains still the only method of well–controlled numerical study of various systems, e.g. with magnetic frustration, or with long–range interactions, as considered in this thesis. Major advantages of Lanczos method for the latter application are listed at the end of this Section. Here we mention only that the recently developed finite–temperature Lanczos method (FTML) by Jaklič and Prelovšek (1994), combining the Lanczos algorithm with a random sampling, allows for analogous treatment of many–body quantum models at $T > 0$ (Jaklič and Prelovšek, 2000) as a standard Lanczos method for $T = 0$.

A complete study of the system thermodynamical, dynamical, transport and ground–state properties without restriction on the type of model is a challenging goal. There are, however, problems for which other specific numerical techniques provide valuable insight, as they are capable of reaching large N (the computational effort scales as a power of N). These are:

(i) density–matrix renormalization group (DMGR), applied to general 1D systems (White, 1998),

(ii) world–line loop QMC applied to non–frustrated spin systems in arbitrary dimensions (Evertz, Lana and Marcu, 1993), and

(iii) auxiliary–fields QMC methods (Blankenbecler, Scalapino and Sugar, 1981).

Apart form restriction to 1D systems, DMGR method (i) strongly prefers open boundary conditions (computation time scales as m^2 for PBC and as m for open–BC, where m is the number of leading eigenvalues of the density matrix included in the calculation). Convergence of the method become also rapidly slower with the range of interactions, which makes DMGR method not suitable for the systems with unscreened long–range Coulomb interactions. In spite of the above limitations, DMGR remains the powerful extension of ED methods in 1D, as it provides physical properties of various systems containing $N = 100 \div 200$ sites with precision unreachable for the finite–time QMC averaging.

In the method (ii) computational efforts scales linearly with N, that allows one to reach huge system size $N \sim 10^6$. This is because in this class of methods the path–integral formulation of the imaginary time propagation maps d–dimensional quantum system onto $(d+1)$–dimensional simple classical system. Within the World–Line QMC algorithm (Hirsch, Scalapino, Sugar and Blankenbecler, 1981) this mapping relates 1D XYZ quantum spin chain to an eight–vertex model (Barma and Shastry, 1978) or 1D t–J model to the 15–vertex model (Assaad and Würtz, 1991). Although world–line methods are simple and powerful, they are also limited to very specific systems, so that no significant progress have been observed in this field since the early 90's.

The last method (iii) is the only QMC algorithm capable of handling a class of models with spin and charge degrees of freedom in dimension larger than unity, such as 2D Hubbard model, which plays a special role in theoretical description of high–T_c superconductivity (Assaad, Hanke and Scalapino, 1994). In the determinantal approach to lattice models (Assaad, 2002), which exists in both ground–state and finite–temperature versions, CPU time scales as N^3, so relatively large systems of $N \sim 100$ sites can be studied. The situation is even better in a very much related Hirsch–Fye impurity algorithm (Hirsch and Fye, 1986), where one can consider infinite system with a single impurity. The latter method has been used extensively in the context of dynamical mean field theories (Jarrell, 1992; Georges, Kotliar, Krauth and Rozenberg, 1996). However, electron correlations in many cases leads to the sign–problem, which remains the central challenge in QMC simulations. Insight into the origin of the sign–problem was provided by Fahy and Hammann (1990), and is beyond the scope of this brief review. We mention only, that for sing–plagued models the computational effort scales exponentially with N (and with the inverse temperature β), that makes the system intractable except for very high temperatures. Defining auxiliary fields in the way which explore the special symmetries of a given model, we avoid the sign–problem in many cases; a remarkable progress has been made for the case of Kondo–lattice models (Capponi and Assaad, 2001).

An interesting generalization of the Lanczos method for QMC simulations have been recently proposed by Sorella (2001). In the *effective Hamiltonian approach* the Lanczos algorithm is used to perform systematic corrections to a variational wavefunction (of Jastrow type), obtained from fixed–node variational QMC. The method combines the efficiency of Lanczos with possibility to study large systems of $N \sim 100$ sites. However, at the present stage, it is not capable of providing an estimate of the dynamical and transport properties.

To summarize this overview, we recall the main features of the Lanczos method, which brought us to apply it for diagonalization of the Hamiltonian in our method combining the first– and the second–quantization scheme (EDABI). In brief, there are three most remarkable advantages of the Lanczos algorithm in comparison to other methods, when applied to small clusters:

- **Accuracy.** The Lanczos method is free of systematic errors. When starting from a random initial state, the system properties converge to their exact values usually up to the machine round–off errors.

- **Efficiency.** The method is actually the fastest for small clusters, when necessary information fits into the machine RAM memory.

- **Universality.** A very mild assumptions are made about the system Hamiltonian. CPU time scales predictably when new term are added.

For future applications to larger systems, particularly for the ladders, the auxiliary–fields QMC and the Maximal Entrophy method (van der Linden, 1995; Jarrel and Gubernatis, 1996) look very promising as the sign–problem is absent in 1D. However, some additional model assumptions must be done.

Chapter 3

Correlated electrons in nanochains

The discussion of 1D systems in a half–filled band sector is interesting for few reasons. From one hand, we have an analytical solution of Hubbard model obtained by Lieb and Wu (1968), in which ground state is insulating for arbitrary small *Coulomb repulsion* U. This result was complemented with weak–coupling renormalization group analysis by Fabrizio (1996), who showed that *umklapp* processes drives any half–filled system with two Fermi points to an insulating state. On the other hand, we have experimental results for quantum rings and wires (Jacak, Hawrylak and Wójs, 1998; Ge, Prasad, Andresen, Bird, Ferry, Lin et al., 2000) and nanotubes (Mintmire, Dunplap and White, 1992; Frank et al., 1998), which demonstrate the metallic behavior even for s–band systems, such as Na nanowires (Krans et al., 1995; Yanson et al., 1999).

This apparent contradiction has been partially lifted by an analysis of parametrized models with additional interactions. Strack and Vollhardt (1993) reported the presence of a metal–insulator transition (MIT) in the extended Hubbard model with *correlated hopping* $V = -t$ (where t is the *hopping* magnitude). Daul and Noack (2000) studied the model with *second–neighbor hopping* t' and found MIT for $t' = 0.5t$. In these models the 2–point structure of the Fermi surface is destroyed by the artificially large additional terms, which do not seem to be relevant in real atomic or molecular systems. Similar restriction concerns the condensation–like MIT described by Lin and Hirsch (1986) in the model with *nearest–neighbor Coulomb interaction* $K = U$. Extensive numerical study of 1D systems with *long–range* Coulomb interactions are, however, not common as yet. The only complete analysis of MIT in such a system was done for spinless fermions (Capponi, Poilblanc and Giamarchi, 2000).

A separate problem concerns the transport properties of a finite–size system, where the separation between quasiparticle levels result always in a finite charge–gap and, additionally, the electron tunneling through a finite barrier leads always to a finite conductivity. In this context, we address the question of metallicity appearance in correlated quantum dots and correlated atomic chains and rings.

In this Chapter we complement our previous study of the correlated 1D chain (Spałek and Rycerz, 2001; Rycerz and Spałek, 2002). The analysis here is performed systematically in the Gaussian $1s$–like basis (for the basis definition and properties *cf.* Appendix A), and using the boundary conditions that minimize ground–state energy for a given system size N (*cf.* Section 3.3.2). Brief comparison with the results for the Slater–type orbitals, used previously, is also provided in Section 3.2.3.

3.1 The Hamiltonian

We consider the system of N_e electrons on N lattice sites, each containing a single valence orbital and an infinite–mass ion (i.e. we start from hydrogenic–like atoms). Including *all* long–range Coulomb interaction and neglecting other terms, one can reduce the generic lattice Hamiltonian (2.3) to the form

$$\begin{aligned} H = \epsilon_a \sum_i n_i + t \sum_{i\sigma} \left(a^\dagger_{i\sigma} a_{i+1\sigma} + \mathrm{HC} \right) \\ + U \sum_i n_{i\uparrow} n_{i\downarrow} + \sum_{i<j} K_{ij} n_i n_j + \sum_{i<j} V_{\mathrm{ion}} \left(\mathbf{R}_j - \mathbf{R}_i \right) . \end{aligned} \tag{3.1}$$

The first term represents the atomic energy (we include it explicitly, since ϵ_a changes with the varying lattice constant). The second describes the kinetic energy of the system with nearest–neighbor hopping t. Next two terms express the intra– and interatomic Coulomb interaction. The last term is the Coulomb repulsion between the ions located at positions $\{\mathbf{R}_i\}$, included for the same reasons as the atomic energy ϵ_a.

Derivation of the microscopic parameters for a given Wannier basis $\{w_i(\mathbf{r})\}$ and their numerical values are provided in the next two sections. Here we recall only the definitions of single– and two–particle parameters t_{ij} (2.4) and V_{ijkl} (2.5), which lead to

$$\epsilon_a = t_{ii} = \langle w_i | \, T \, | w_i \rangle , \qquad t = t_{i,i+1} = \langle w_i | \, T \, | w_{i+1} \rangle , \tag{3.2}$$

and

$$U = V_{iiii} = \langle w_i w_i | \, V \, | w_i w_i \rangle , \qquad K_{ij} = V_{ijij} = \langle w_i w_j | \, V \, | w_i w_j \rangle . \tag{3.3}$$

The operator T represents the full single–particle lattice potential, i.e.

$$T(\mathbf{r}) = -\frac{\hbar^2}{2m} \nabla^2 - \sum_j \frac{e^2}{|\mathbf{r} - \mathbf{R}_j|} \overset{\text{a.u.}}{=} -\nabla^2 - \sum_j \frac{2}{|\mathbf{r} - \mathbf{R}_j|}, \tag{3.4}$$

where a.u. means the expression in atomic units. $V = e^2/|\mathbf{r}_1 - \mathbf{r}_2|$ is the usual Coulomb potential (we do not include any screening by e.g. core electrons as we want to discuss the model situation, but in a rigorous manner). Analogously, the Coulomb repulsion between ions $V_{\text{ion}} = V$.

The interatomic Coulomb term in the Hamiltonian (3.1) can be represented as a following

$$\begin{aligned}\sum_{i<j} K_{ij} n_i n_j &= \sum_{i<j} K_{ij}(n_i - 1)(n_j - 1) - \sum_{i<j} K_{ij} + 2N_e \frac{1}{N} \sum_{i<j} K_{ij} \\ &= H_K + N_e \frac{1}{N} \sum_{i<j} K_{ij} + (N_e - N) \frac{1}{N} \sum_{i<j} K_{ij}, \qquad (3.5)\end{aligned}$$

where we use the relation $N_e = \sum_i n_i$ and introduce the symbol H_K for the long–range Coulomb interaction. Substituting (3.5) to the Hamiltonian (3.1) and representing the ionic repulsion in the form

$$\sum_{i<j} \frac{2}{R_{ij}} = N_e \frac{1}{N} \sum_{i<j} \frac{2}{R_{ij}} - (N_e - N) \frac{1}{N} \sum_{i<j} \frac{2}{R_{ij}}$$

(in Rydbergs), where $R_{ij} = |\mathbf{R}_j - \mathbf{R}_i|$, we obtain that

$$H = N_e \epsilon_a^{\text{eff}} + H_t + H_U + H_K + (N_e - N) \frac{1}{N} \sum_{i<j} \left(K_{ij} - \frac{2}{R_{ij}} \right). \qquad (3.6)$$

We denote kinetic energy and intraatomic Coulomb interaction terms by H_t and H_U (respectively), the *effective atomic energy* is defined (in Ry) as

$$\epsilon_a^{\text{eff}} \equiv \epsilon_a + \frac{1}{N} \sum_{i<j} \left(K_{ij} + \frac{2}{R_{ij}} \right). \qquad (3.7)$$

The effective atomic energy contains the electron attraction to the ions, as well as the mean–field part of their repulsion (K_{ij}), and the ion–ion interaction. Such definition preserves correctly the atomic limit, when the distant atoms should be regarded as neutral objects. In practice, the above form is calculated numerically with the help of Richardson extrapolation for $N \to \infty$ (Burden and Faires, 1985). One can find it converges exponentially with N, whereas *bare* ϵ_a is divergent harmonically, due to $\sim 1/r$ Coulomb wells in the single–particle potential (3.4). The situation is more subtle in the case of hopping integral t, and will be discussed in Section 3.1.1.

Last term in the Hamiltonian (3.6) vanish for the half–filled band case $N_e = N$, as it is $\propto (N_e - N)$. It also does not affect the system charge gap (as it depends linearly on N_e), and the correlation functions away from half filling (as a constant term). For these reasons, we skip the last term in (3.6) in all the further analysis. Therefore, recalling the definitions of the terms H_t, H_U, and H_K, we can write down the system Hamiltonian in the form

$$H = \epsilon_a^{\mathrm{eff}} \sum_i n_i + t \sum_{i\sigma} \left(a_{i\sigma}^{\dagger} a_{i+1\sigma} + \mathrm{HC} \right) + U \sum_i n_{i\uparrow} n_{i\downarrow} + \sum_{i<j} K_{ij} \delta n_i \delta n_j, \quad (3.8)$$

where $\delta n \equiv n_i - 1$. Thus all the *mean–field* Coulomb terms are collected in $\epsilon_a^{\mathrm{eff}}$, whereas the last term in the above Hamiltonian represent the *correlated* part of the long–range interactions.

3.1.1 Wannier basis and tight–binding approximation

The parameters of our model Hamiltonian (3.8) are define by Eq. (3.2) and (3.3) in terms of Wannier basis $\{w_i(\mathbf{r})\}$. In the framework of *tight–binding approximation* (TBA) one can postulate Wannier functions in the form

$$w_i = \beta \left[\Psi_i - \gamma (\Psi_{i-1} + \Psi_{i+1}) \right], \quad (3.9)$$

where Ψ_j represents the atomic function (i.e. of $1s$ type) centered on site j (see Appendix A and B for details). The above finite expansion is validated by an exponential drop of Wannier functions (Kohn, 1959; Zeiner, Dirl and Davies, 1998). The orthogonality relation $\langle w_i | w_{i\pm1} \rangle = 0$ and the normalization condition $\langle w_i | w_i \rangle = 1$ leads to coefficients of the expansion (3.9)

$$\gamma = \frac{S_1}{(1+S_2) + \sqrt{(1+S_2)^2 - S_1(3S_1 + S_3)}}, \quad (3.10)$$

and

$$\beta = \left[1 - 4\gamma S_1 + 2\gamma^2 (1 + S_2) \right]^{-1/2}, \quad (3.11)$$

where we define the overlap integral of atomic functions $S_m = \langle \Psi_i | \Psi_{i+m} \rangle$ (the normalization $S_0 = \langle \Psi_i | \Psi_i \rangle = 1$ is supposed).

The above expressions are well–defined if the quantity under the square root in Eq. (3.10)

$$\Delta = (1+S_2)^2 - S_1(3S_1 + S_3) > 0,$$

which is the case for all the lattice constants studied here (see Table 3.1 for numerical values). The actual limits of TBA comes with nonzero overlap integral of Wannier functions defined by Eq. 3.9, when considering the second–neighbor sites

$$\langle w_i | w_{i+2} \rangle = \beta^2 \gamma^2.$$

TABLE 3.1: Wannier–basis parameters for 1D chain calculated in the Gaussian STO–3G basis (see Appendix A) as a function of lattice parameter a (a_0 is the Bohr radius). The values of the optimal inverse orbital size $\alpha_{\min}$ are also provided.

a/a_0	$\alpha_{\min}a_0$	β	γ	$\langle w_i \vert w_{i+2}\rangle$	Δ
1.5	1.363	1.41984	0.32800	0.21689	0.34735
2.0	1.220	1.23731	0.26301	0.10590	0.50525
2.5	1.122	1.14133	0.20965	0.05725	0.63980
3.0	1.062	1.08190	0.16246	0.03089	0.75691
3.5	1.031	1.04394	0.12013	0.01573	0.85349
4.0	1.013	1.02216	0.08568	0.00768	0.92009
4.5	1.007	1.01010	0.05795	0.00343	0.96170
5.0	1.004	1.00429	0.03779	0.00144	0.98327
6.0	1.001	1.00063	0.01451	0.00021	0.99749
7.0	1.000	1.00007	0.00483	$2.3{\cdot}10^{-5}$	0.99972
8.0	1.000	1.00001	0.00139	$1.9{\cdot}10^{-6}$	0.99998
10.0	1.000	1	$7.3{\cdot}10^{-5}$	$5.3{\cdot}10^{-9}$	1

Numerical values of the overlap remainder $\langle w_i|w_{i+2}\rangle$ are also gathered in Table 3.1. The above nonorthogonality may strongly affect the second neighbor hopping, as a zero–overlap is crucial for the convergence of hopping integral on an lattice providing the single–particle potential of the form (3.4). However, as the only term involving second–neighbors in our Hamiltonian (3.8) is the interatomic Coulomb repulsion K_2, the presented TBA approach seems sufficient for the purpose of this thesis.

Substituting Eq. (3.9) to (3.2) we obtain the expressions for single–particle parameters

$$\epsilon_a = \beta^2\left[\epsilon'_a - 4\gamma t'_1 + 2\gamma^2(\epsilon'_a + t'_2)\right], \tag{3.12}$$

and

$$t = \beta^2\left[t'_1 - 2\gamma(\epsilon'_a + t'_2) + \gamma^2(3t'_1 + t'_3)\right], \tag{3.13}$$

where primes denotes the parameters in the atomic basis, namely $\epsilon'_a = \langle\Psi_i|\,T\,|\Psi_i\rangle$ and $t'_m = \langle\Psi_i|\,T\,|\Psi_{i+m}\rangle$. The detailed formulas for ϵ'_a and t'_m are provided in Appendix A for the Gaussian–type orbitals and in Appendix B for the Slater–type. Here we only emphasize, that as the terms up to third–neighbors are included in Eq. (3.13) one should carefully apply TBA on the level of single–particle potential $T(\mathbf{r})$ defined by Eq. (3.4). This is the main goal of this section.

We already mentioned, that the atomic energy ϵ_a is divergent with the lattice size N and define the convergent effective quantity ϵ_a^{eff} (3.7). In case of hopping t

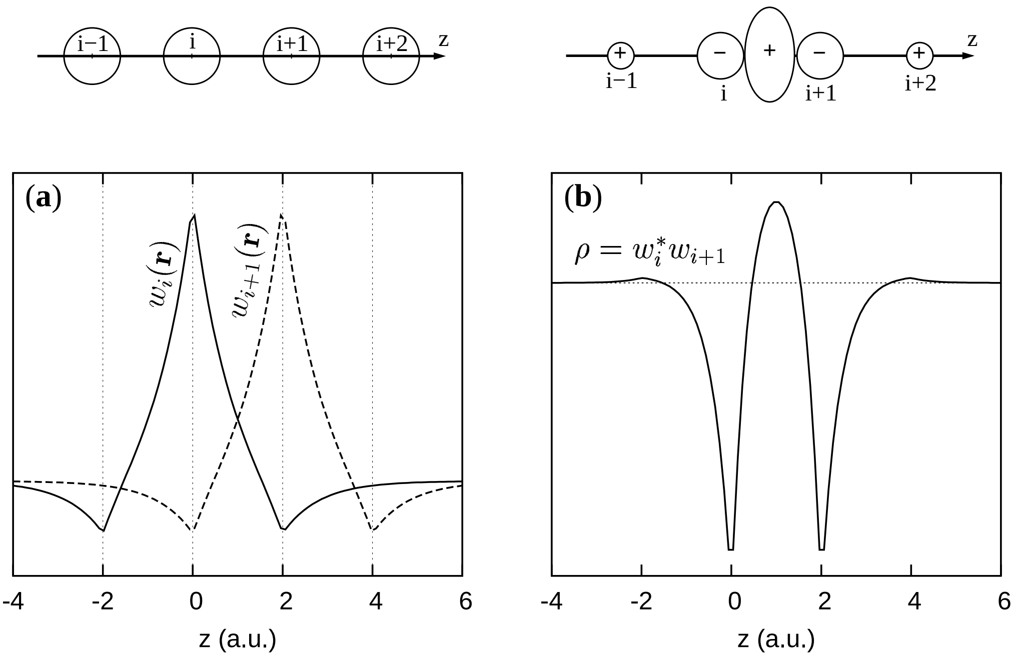

FIGURE 3.1: Schematic representation of the Wannier functions (a) centered on the neighboring sites $w_i(\mathbf{r})$ and $w_{i+1}(\mathbf{r})$, and (b) the resulting charge distribution $\rho(\mathbf{r}) = w_i^*(\mathbf{r})w_{i+1}(\mathbf{r})$. The values of the lattice parameter and the inverse orbital size are $a = 2a_0$ and $\alpha_{\min}a_0 = 1.22$, respectively.

the convergence is provided by an orthogonality of the Wannier functions w_i and w_{i+1}. This is because, when calculating the hopping integral

$$t = \langle w_i | T | w_{i+1} \rangle \overset{\text{a.u.}}{=} \langle w_i | -\nabla^2 | w_{i+1} \rangle + \sum_k \langle w_i | V_k | w_{i+1} \rangle, \tag{3.14}$$

one approaches to the series of electrostatic interactions between the continuous charge distribution $\rho(\mathbf{r}) = w_i^*(\mathbf{r})w_{i+1}(\mathbf{r})$ (depicted schematically in Figure 3.1) and the ions, each providing the Coulomb well $V_k(\mathbf{r}) = -2/|\mathbf{r} - \mathbf{R}_k|$ (in Ry) located on the k–th lattice site, namely

$$\langle w_i | V_k | w_{i+1} \rangle = -\int d^3\mathbf{r} w_i^*(\mathbf{r}) \frac{2}{|\mathbf{r} - \mathbf{R}_k|} w_{i+1}(\mathbf{r}).$$

In order to estimate the asymptotic behavior of t we take into account only the leading term in the multipole expansion of the charge distribution $\rho(\mathbf{r})$. Because of the symmetry, the total charge $q = \int d^3\mathbf{r}\rho(\mathbf{r}) = 0$, as well as the dipole moment $\mathbf{p} = \int d^3\mathbf{r}\ \mathbf{r}\rho(\mathbf{r}) = 0$. Thus the first non–vanishing term is the quadrupole moment, defined as a traceless tensor

$$Q_{pq} = \int d^3\mathbf{r}(3r_p r_q - r^2\delta_{pq})\rho(\mathbf{r})$$

(Jackson, 1975). The relevant contribution to the potential energy in (3.14) is equal to

$$-\frac{1}{6}\sum_{pq} Q_{pq} \left.\frac{\partial^2 U}{\partial r_p \partial r_q}\right|_{\mathbf{R}_C},$$

where $U(\mathbf{r}) = \sum_k V_k(\mathbf{r})$ is the total potential of the lattice and $\mathbf{R}_C = (\mathbf{R}_i + \mathbf{R}_{i+1})/2$ denotes the quadrupole position. The hopping integral t (3.14) become now convergent with $N \to \infty$ even in 3D, because of the symmetry (the distant Coulomb wells do not influence the gradient of an electric field, $\partial^2 U/\partial r_p \partial r_q$, inside an infinite system).

Since the formal convergence of ϵ_a^{eff} (3.7) and t (3.14) with N was shown, few technical remarks should be added. In practice, when using the expressions (3.12) and (3.13) one has to deal with the divergent quantities in the atomic basis (ϵ_a', t_1', etc.) This may, in principle, plague the resulting values of ϵ_a^{eff} and t with round–off errors. This is fortunately no the case in 1D, where the divergence is harmonic only, but should be considered carefully in 2D and 3D, where the divergence with N is, respectively, of order $\sim N^{1/2}$ and $\sim N^{2/3}$. The problem could be managed by making a particular transformation of the single–particle operator $T(\mathbf{r})$

$$T(\mathbf{r}, \Sigma_R) = T(\mathbf{r}) + \Sigma_R, \tag{3.15}$$

where Σ_R is a constant of the same asymptotic behavior as $T(\mathbf{r})$, but has an opposite sign, namely

$$\Sigma_R = \sum_k \frac{2}{|\mathbf{R}_c - \mathbf{R}_k|}.$$

The transformation (3.15) affects the matrix elements in a following manner

$$t_{ij}(\Sigma_R) = \langle w_i | \, T + \Sigma_R \, | w_j \rangle = t_{ij} + \Sigma_R \delta_{ij},$$

so only the atomic energy $\epsilon_a = t_{ii}$ changes. The simple redefinition of the effective atomic energy

$$\epsilon_a^{\text{eff}}(\Sigma_R) = \epsilon_a(\Sigma_R) + \left[\frac{1}{N}\sum_{i<j}\left(K_{ij} + \frac{2}{R_{ij}}\right) - \Sigma_R\right] = \epsilon_a^{\text{eff}},$$

(brackets denotes the order of operations, essential on a finite–precision machine) makes the model Hamiltonian (3.8) totally invariant under the transformation (3.15).

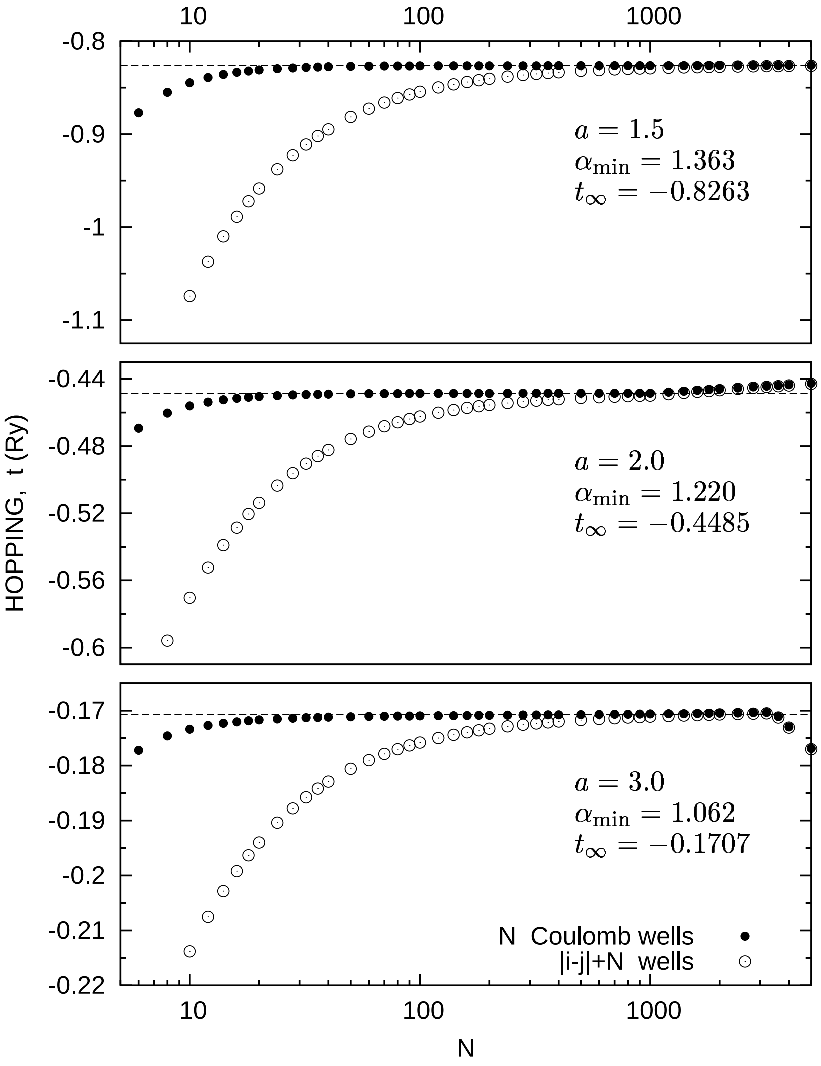

FIGURE 3.2: Convergence of the hopping integral t calculated including a constant number of N Coulomb wells on the atomic level (*dots*) versus the version including $|i-j|+N$ wells when calculating t'_{ij} (*circles*). The values of lattice parameter a and inverse orbital size α are specified in a.u. Limiting values of the hopping integral t_∞ (in Ry) are obtained via the Richardson extrapolation in the Slater–type basis.

Additionally, the convergence of the hoping integral t depends dramatically on the way, in which we cut-off distant Coulomb wells in a single–particle potential $T(\mathbf{r})$ when calculating the primed terms in Eq. (3.13). The most efficient method we have determined relies on taking the same number of wells N for all primed terms, namely

$$\begin{aligned}
\epsilon_a' &= \langle\Psi_i| T |\Psi_i\rangle \approx \langle\Psi_i| -\nabla^2 |\Psi_i\rangle + \sum\nolimits_{k=i-N/2}^{i+N/2} \langle\Psi_i| V_k |\Psi_i\rangle \,, \\
t_1' &= \langle\Psi_i| T |\Psi_{i+1}\rangle \approx \langle\Psi_i| -\nabla^2 |\Psi_{i+1}\rangle + \sum\nolimits_{k=i-N/2}^{i+N/2} \langle\Psi_i| V_k |\Psi_{i+1}\rangle \,, \qquad (3.16) \\
t_2' &= \langle\Psi_{i-1}| T |\Psi_{i+1}\rangle \approx \langle\Psi_{i-1}| -\nabla^2 |\Psi_{i+1}\rangle + \sum\nolimits_{k=i-N/2}^{i+N/2} \langle\Psi_{i-1}| V_k |\Psi_{i+1}\rangle \,, \\
t_3' &= \langle\Psi_{i-1}| T |\Psi_{i+2}\rangle \approx \langle\Psi_{i-1}| -\nabla^2 |\Psi_{i+2}\rangle + \sum\nolimits_{k=i-N/2}^{i+N/2} \langle\Psi_{i-1}| V_k |\Psi_{i+2}\rangle \,.
\end{aligned}$$

The comparison of t obtained by using formulas (3.16) with the simplest choice

$$t_{ij}' = \langle\Psi_i| T |\Psi_j\rangle \approx \langle\Psi_i| - \nabla^2 |\Psi_j\rangle + \sum_{k=i-1}^{j+1} \langle\Psi_i| V_k |\Psi_j\rangle \qquad (3.17)$$

is presented in Figure 3.2. We find, that the choice of $N = 6$ wells in Eqs. (3.16) provides the same accuracy as $N = 60 \div 70$ in Eq. (3.17). This is because the cut–off in $T(\mathbf{r})$ via formulas (3.16) could be, approximately, regarded as a transformation of the form (3.15), whereas Eq. (3.17) corresponds to different constants Σ_R in ϵ_a', t_1', etc. that lead to the invariance of the Hamiltonian only for $N \gg 1$. The results for $N \gtrsim 2000$ in Figure 3.2 suffers from the finite–precision numerical integration of the potential energy part in Eqs. (3.16) and (3.17), which was of the order $\sim N \cdot 10^{-7}$ Ry for the Slater type orbitals (see Appendix B). However, the wide plateau, typically for $N = 50 \div 2000$ is sufficient to perform the extrapolation to $N \to \infty$. In practice, 2–nd order Richardson extrapolation (Burden and Faires, 1985) for $N = 20$, 40 and 80 provides an excellent accuracy.

3.1.2 Interaction parameters

The only parameters of the Hamiltonian (3.8) not determined as yet are the intra– and interatomic Coulomb repulsion U and $K_{ij} = K_{|i-j|}$. Since $U = K_{ii}$, one can express all of them in a compact formula obtained by substituting the expansion (3.9) to the definition (3.3)

$$K_{ij} = \langle w_i w_j| V |w_i w_j\rangle = \sum_{\delta_1\delta_2\delta_3\delta_4} \mathrm{B}_{\delta_1}\mathrm{B}_{\delta_2}\mathrm{B}_{\delta_3}\mathrm{B}_{\delta_4} \langle\Psi_{i+\delta_1}\Psi_{j+\delta_2}| V |\Psi_{i+\delta_3}\Psi_{j+\delta_4}\rangle \,, \qquad (3.18)$$

where $\delta_1 \ldots \delta_4 = -1, 0, 1$ and

$$\mathrm{B}_\delta = \left\{ \begin{array}{cc} \beta, & \delta = 0 \\ -\beta\gamma, & \delta = \pm 1 \end{array} \right. .$$

The sum in Eq. (3.18) contains $3^4 = 81$ terms, as each index δ assumes 3 values. In practice, this number can be reduced to 36 by using the symmetry of $V'_{ijkl} = \langle \Psi_i \Psi_j | \, V \, | \Psi_k \Psi_l \rangle$ terms with $i \leftrightarrow k$ and $j \leftrightarrow l$, that clearly comes out in the same integral form as (2.5).

In the case of Gaussian–type orbitals, all the V'_{ijkl} terms in Eq. (3.18) are calculated explicitly, since the product of two Gaussians has still a Gaussian form (see Appendix A). For the Slater basis, however, the compact formulas are available only for two–site terms, namely the Coulomb repulsion $K'_{ij} = V'_{ijij}$, correlated hoping $V'_{ij} = V'_{iiij}$, and the Heisenberg exchange integral $J'_{ij} = V'_{ijji} = V'_{iijj}$ (see Appendix B). Numerical calculations for the Slater–type basis, if the three– and four–site terms are included, requires an extansive computational effort. So, the systematic analysis in the Gaussian–type orbitals becomes much more efficient.

The values of the model parameters, corresponding to the lattice spacing $a/a_0 = 1.5 \div 10$, are presented in Table 3.2. The data correspond to the optimal values of the inverse orbital size α_{min}, as displayed in Table 3.1. We also provide there the values of the *correlated hopping* V and the *Heisenberg–exchange integral* J to show that one could disregard the corresponding terms in the Hamiltonian (3.8).

TABLE 3.2: Microscopic parameters (in Ry) of 1D chain, calculated in the Gaussian STO–3G basis. Corresponding values of the optimal inverse orbital size α_{min} are provided in Table 3.1. The Richardson extrapolation with $N \to \infty$ were used.

R/a_0	ϵ_a^{eff}	t	U	$V^\dagger$	$J^\dagger$	K_1	K_2	K_3
1.5	0.0997	-0.8309	2.054	-43.93	30.92	1.165	0.667	0.447
2.0	-0.5495	-0.4423	1.733	-23.81	21.06	0.911	0.501	0.334
2.5	-0.7973	-0.2644	1.531	-14.95	15.13	0.750	0.401	0.267
3.0	-0.9015	-0.1708	1.407	-10.99	10.91	0.639	0.334	0.222
3.5	-0.9483	-0.1156	1.335	-9.41	75.6	0.557	0.286	0.191
4.0	-0.9705	-0.0796	1.291	-8.74	4.93	0.493	0.250	0.167
4.5	-0.9815	-0.0549	1.270	-8.10	2.92	0.442	0.222	0.148
5.0	-0.9869	-0.0374	1.258	-7.07	1.57	0.399	0.200	0.133
6.0	-0.9908	-0.01676	1.249	-4.29	0.34	0.333	0.167	0.111
7.0	-0.9915	-0.00710	1.247	-1.96	0.05	0.286	0.146	0.095
8.0	-0.9917	-0.0027	1.247	-0.70	$5{\cdot}10^{-3}$	0.250	0.125	0.083
10.0	-0.9917	$-2.5{\cdot}10^{-3}$	1.247	-0.05	$2{\cdot}10^{-5}$	0.200	0.100	0.067

† The values of V and J are specified in mRy.

The values of the effective atomic energy ϵ_a^{eff} and the hopping integral t were obtained by using Richardson extrapolation for the lattice size $N \to \infty$ and Eqs. (3.16) for calculating the corresponding parameters in the atomic basis. One can note the values of t calculated in the Gaussian STO–3G basis (listed in Table 3.2) differs from those obtained in Slater basis (presented in Figure 3.2) by less then 0.5% when using the same values of the inverse orbital size α. However, the differences grow significantly, if α is optimized independently for the Slater basis and the three– and four–site terms are not included in the atomic basis. More detailed discussion of this problem is provided in the next section.

3.2 The optimized ground–state energy

We now consider a nanoscopic linear chain of $N = 6 \div 10$ atoms, each containing a single valence electron (hydrogenic–like atoms), including *all* long-range Coulomb interactions (3– and 4–site terms are treated exactly in the Gaussian STO–3G basis). We focus here on the so–called *Extended Hubbard Model* with Hamiltonian (3.8).

3.2.1 Results from EDABI method

The Hamiltonian (3.8) is diagonalized in the Fock space with the help of Lanczos technique. As the microscopic parameters ϵ_a^{eff}, t, U, and K_{ij} are calculated numerically in the Gaussian STO–3G basis, the inverse orbital size α of the $1s$–like state is subsequently optimized to obtain the ground state energy E_G as a function of the interatomic distance a. We have already shown (Rycerz and Spałek, 2001) that such a combined exact diagonalization – *ab initio* study of the one dimensional system provides precise values of the localization threshold, the electron–lattice couplings, and the dimerization magnitude. However, the convergence of the results obtained with the Slater-type orbitals is not sufficient to be able to perform a finite–size scaling with the lattice size $N \to \infty$. This is because, when calculating the microscopic parameters in the single–particle (Wannier) basis, one ignores the three– and the four–site interaction terms, that represents an uncontrolled approximation. Numerical illustration of this problem is provided in Section 3.2.3.

In contrast, for the Gaussian-type orbitals we can treat the three– and four–site terms exactly. Their effects on the convergence of the results for the ground-state energy E_G and the optimal inverse orbital size $\alpha_{\min}$ are shown in Figure 3.3 for $N = 6 \div 10$ atoms. These results were used to extrapolate the value of the variational parameter $\alpha_{\min}$ to larger N to speed up the computations. Figure 3.3 illustrates also the *Hubbard localization criterion.* Namely, for the interatomic

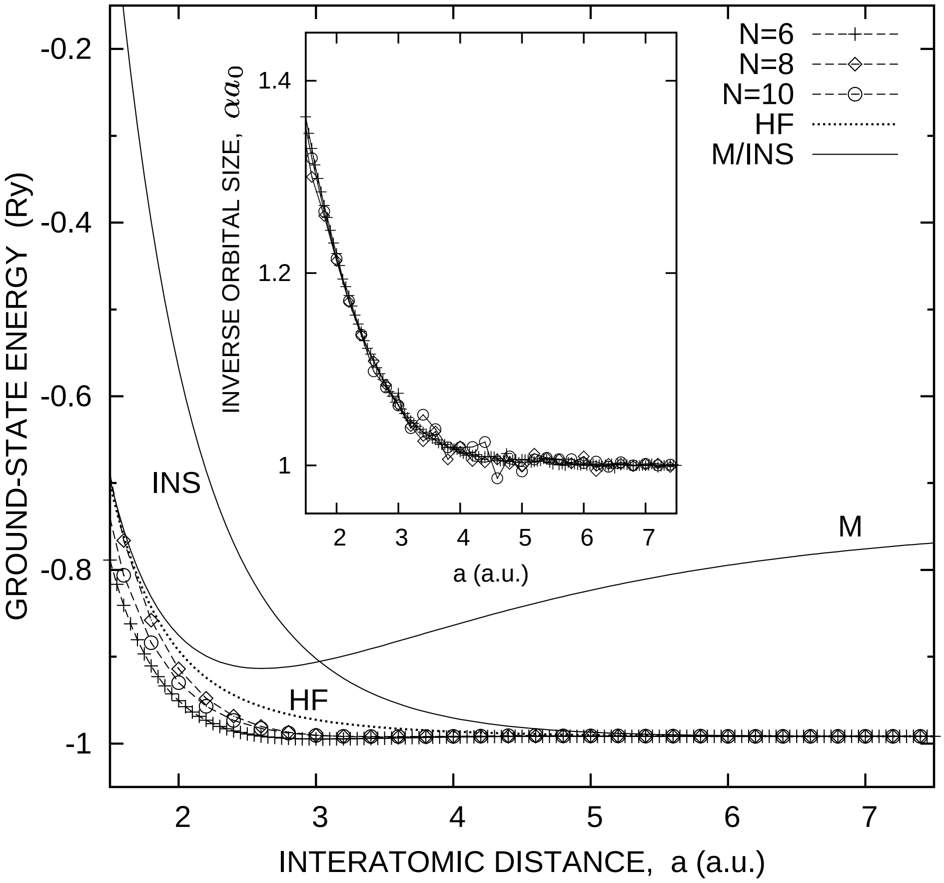

FIGURE 3.3: The ground state energy per atom for the linear chain of $N = 6 \div 10$ atoms with periodic boundary conditions. The Gaussian-type orbitals (STO–3G basis) have been used. The energies of the *ideal* metallic (M), *ideal* insulating (INS), and Hartree–Fock (HF) solutions for an *infinite* system are shown for comparison. The *inset* provides the optimal inverse orbital size $\alpha_{\min}$.

distance $a \approx 3a_0$ the energy of the *ideal metallic* state (M), determined as

$$E_G^{\mathrm{M}} = \epsilon_a^{\mathrm{eff}} - \frac{4}{\pi}\,|t| + \frac{1}{N}\sum_{i<j} K_{ij}\,\langle \delta n_i \delta n_j \rangle\,, \tag{3.19}$$

where the charge–density correlation function $\langle \delta n_i \delta n_j \rangle$ is calculated for the electron gas on the lattice

$$\langle \delta n_i \delta n_j \rangle = -2\frac{\sin^2(\pi\,|i-j|\,/2)}{(\pi\,|i-j|)^2}$$

(for the *half–filled* band case), crosses over to that representing the *Mott insulating* state (INS), with

$$E_G^{\mathrm{INS}} = \epsilon_a^{\mathrm{eff}}. \tag{3.20}$$

One usually adds the second–order perturbation correction to the energy of insulating state (3.20) in the well–known form (Emery, 1979)

$$\frac{4t^2}{U-K_1}\left(\langle \mathbf{S}_i \cdot \mathbf{S}_{i+1} \rangle - \frac{1}{4}\right),$$

where $\mathbf{S}$ is a spin operator and the Bethe–Ansatz result is $\langle \mathbf{S}_i \cdot \mathbf{S}_{i+1} \rangle - 1/4 = -\ln 2$ for the Heisenberg antiferromagnet. Here we only compare the two simplest variational approaches, leading to the energies (3.19) and (3.20).

The critical value of a is very close to obtained for the $1s$ Slater–type orbitals (Spałek and Rycerz, 2001). The validity of the Hubbard criterion for this one–dimensional system is controversial, as the energy of the antiferromagnetic (so *Slater-type*) Hartree–Fock solution (HF) is lower than those of M and INS. Therefore, the detailed verification of this criterion by estimating the charge–energy gap and transport properties of the correlated system is the main goal of this Chapter.

3.2.2 Hartree–Fock approximation

In this Section we describe briefly the Hartree–Fock (HF) solution included in Figure 3.3. Since analytical HF equations for an infinite system described by the Hamiltonian (3.8) are not easy to obtain, we apply here a fully numerical procedure, capable of treating the system size $N \sim 10^3$. The main advantage of this approach is that we utilize an unrestricted Hartree–Fock (UHF) method, in which no particular charge or spin order is supposed in the resulting Slater determinant. It can be also easily generalized for the systems of a higher dimensionality, which are, however, beyond the scope of this thesis.

An effective Hartree–Fock version of the Hamiltonian (3.8), including the long–range part of the Coulomb interaction, reads

$$\begin{aligned} H^{\mathrm{HF}} = \epsilon_a^{\mathrm{eff}} \sum_i n_i + t \sum_{i\sigma} \left(a_{i\sigma}^\dagger a_{i+1\sigma} + \mathrm{HC} \right) + U \sum_i \left(\langle n_{i\uparrow} \rangle n_{i\downarrow} + \langle n_{i\downarrow} \rangle n_{i\uparrow} \right. \\ \left. - \langle n_{i\uparrow} \rangle \langle n_{i\downarrow} \rangle \right) + \sum_{i<j} K_{ij} \left(\langle \delta n_i \rangle \delta n_j + \langle \delta n_j \rangle \delta n_i - \langle \delta n_i \rangle \langle \delta n_j \rangle \right) \\ - \sum_{i<j,\sigma} K_{ij} \left(\langle a_{i\sigma}^\dagger a_{j\sigma} \rangle a_{j\sigma}^\dagger a_{i\sigma} + \langle a_{j\sigma}^\dagger a_{i\sigma} \rangle a_{i\sigma}^\dagger a_{j\sigma} - |\langle a_{i\sigma}^\dagger a_{j\sigma} \rangle|^2 \right) . \end{aligned} \tag{3.21}$$

The above effective Hamiltonian has the form $H^{\mathrm{HF}} = H_\uparrow^{\mathrm{HF}} + H_\downarrow^{\mathrm{HF}}$ (up to constant terms), where the commutator $[H_\uparrow^{\mathrm{HF}}, H_\downarrow^{\mathrm{HF}}] = 0$, as the particles with $\sigma =\uparrow$ are coupled to those with $\sigma =\downarrow$ by a diagonal (*Hartree*) term only. Because of that property, one can diagonalize separately the $N \times N$ Hamiltonian for $\sigma =\uparrow$ and that for $\sigma =\downarrow$.

We start the self–consistent procedure by choosing the set of $N/2$ random, orthogonal wavefunctions for $\sigma =\uparrow$ and separate for $\sigma =\downarrow$ (we suppose an absence of global magnetization). Then, the cumulants $\langle a_{i\sigma}^\dagger a_{j\sigma} \rangle$ are estimated, and the resulting HF Hamiltonians for $\sigma =\uparrow, \downarrow$ are diagonalized with standard numerical routines (Press et al., 1992). Having obtained new sets of $N/2$ eigenfunctions corresponding to the lowest–lying eigenvalues for $\sigma =\uparrow, \downarrow$, we calculate new cumulants $\langle a_{i\sigma}^\dagger a_{j\sigma} \rangle$. In the next step, we apply the relaxation scheme, namely, we substitute the diagonal cumulants

$$\langle n_{i\sigma} \rangle_{\mathrm{new}} \to (1-\eta) \langle n_{i\sigma} \rangle_{\mathrm{new}} + \eta \langle n_{i\sigma} \rangle_{\mathrm{old}} ,$$

to avoid the oscillating solutions. In practice, the choice of $\eta = 0.2 \div 0.5$ provides a convergent and efficient algorithm.

For the half–filled band case ($N_e = N$), we find for the above procedure a convergence to the antiferromagnetic (AF) solution, with an uniform charge distribution, and the alternating spin order, i.e.

$$\langle \delta n_i \rangle = 1 - \bar{n} = 0, \qquad \langle n_{i\uparrow} \rangle - \langle n_{i\downarrow} \rangle = (-1)^i m, \tag{3.22}$$

where $\bar{n} = N_e/N$ is the band filling and m is the magnetization. Typically, only few domain walls appear due to the randomness of the initial–state choice. This property suggest us to keep the diagonal cumulants satisfying AF order (3.22) at each step, and determine only the magnetization m self–consistently (starting random basis, as before). The values of ground–state energy, presented in Figure 3.3 and that of charge–energy gap, discussed in Section 3.3.4, are obyained within such a modified procedure.

3.2.3 Comparison with the results for the Slater–basis

We compare now the results obtained within EDABI method for the Gaussian– and the Slater–basis sets. However, as the Wannier functions in the form (3.9) lead to instabilities when using the Slater basis for the lattice parameter $a \lesssim 3a_0$ (Rycerz, 2000), a few modifications must be introduced to make such comparison possible. First of all, we reduce the interaction part of the Hamiltonian (3.8) to the Hubbard term only, so we put $\langle \delta n_i \delta_j \rangle \approx 0$ for $i \neq j$. Moreover, we take *six* Coulomb wells only in the single–particle potential $T(\mathbf{r})$, when calculating ϵ_a^{eff} and t via Eqs. (3.16) in the atomic representation. As the remaining part of the approach is standard, we use formulas (3.12), (3.13), and (3.18) to estimate the model parameters in the Wannier basis, whereas the quantities in the atomic representation (*primed*) are calculated as described in Appendix A and B for the Gaussian and the Slater base, respectively.

Numerical results for a chain containing $N = 10$ atoms are shown in Tables 3.3 and 3.4. The data for Gaussian–type STO–3G basis differ from those obtained for the model with long–range Coulomb interaction and the single–particle potential of an infinite lattice (see Table 3.2) by less than 5%, whereas the errors for the Slater–type orbitals approach of 30%. This is because, when using the Slater–

TABLE 3.3: Optimized inverse orbital size, microscopic parameters and the ground–state energy for 1D chain of $N = 10$ atoms calculated in Gaussian–type STO–3G basis and as a function of the interatomic distance. Intersite Coulomb repulsion K_1 is included on the mean–field level in ϵ_a^{eff}, Hubbard U term is treated exactly. Single–particle potential is approximated by *six* Coulomb wells.

a/a_0	$\alpha_{\min}a_0$	ϵ_a^{eff}	t	U	K	E_G/N
1.5	1.309	0.1311	-0.8643	2.002	1.154	-0.5684
2.0	1.205	-0.5342	-0.4595	1.718	0.908	-0.8154
2.5	1.120	-0.7893	-0.2750	1.530	0.750	-0.9139
3.0	1.067	-0.8975	-0.1776	1.412	0.639	-0.9567
3.5	1.038	-0.9465	-0.1197	1.342	0.558	-0.9756
4.0	1.020	-0.9698	-0.0820	1.299	0.494	-0.9841
4.5	1.013	-0.9812	-0.0562	1.276	0.442	-0.9881
5.0	1.005	-0.9868	-0.0382	1.260	0.399	-0.9901
6.0	1.003	-0.9908	-0.0170	1.251	0.333	-0.9914
7.0	1.000	-0.9915	-0.0072	1.247	0.286	-0.9917
8.0	1.000	-0.9917	-0.0027	1.246	0.250	-0.9917
10.0	1.000	-0.9917	-0.0003	1.246	0.200	-0.9917

TABLE 3.4: Optimized inverse orbital size, microscopic parameters and the ground–state energy for $N = 10$ atoms calculated in Slater–type basis. Inter-site Coulomb repulsion K_1 is included on the mean–field level in ϵ_a^{eff}, Hubbard U term is treated exactly. Single–particle potential contains *six* Coulomb wells.

a/a_0	$\alpha_{\min}a_0$	ϵ_a^{eff}	t	U	K	E_G/N
1.5	1.806	0.9103	-1.0405	2.399	1.695	0.0665
2.0	1.491	-0.1901	-0.5339	1.985	1.172	-0.5179
2.5	1.303	-0.6242	-0.3076	1.722	0.889	-0.7627
3.0	1.189	-0.8180	-0.1904	1.553	0.713	-0.8800
3.5	1.116	-0.9104	-0.1230	1.440	0.596	-0.9391
4.0	1.069	-0.9559	-0.0815	1.365	0.513	-0.9693
4.5	1.039	-0.9784	-0.0546	1.317	0.451	-0.9848
5.0	1.022	-0.9896	-0.0370	1.288	0.403	-0.9926
6.0	1.013	-0.9977	-0.0165	1.269	0.334	-0.9982
7.0	1.001	-0.9995	-0.0072	1.252	0.286	-0.9996
8.0	1.001	-0.9999	-0.0031	1.251	0.250	-0.9999
10.0	1.000	-1.0000	0.0003	1.250	0.200	-1.0000

TABLE 3.5: Optimized inverse orbital size, microscopic parameters and the ground–state energy for 1D chain of $N = 10$ atoms, calculated in Gaussian–type STO–3G basis. *Long–range* Coulomb interactions are included exactly, single–particle potential contains *six* Coulomb wells.

a/a_0	$\alpha_{\min}a_0$	ϵ_a^{eff}	t	U	K	E_G/N
1.5	1.322	0.1340	-0.8684	2.014	1.156	-0.7691
2.0	1.208	-0.5338	-0.4603	1.721	0.909	-0.9377
2.5	1.119	-0.7894	-0.2748	1.528	0.749	-0.9824
3.0	1.063	-0.8977	-0.1770	1.407	0.639	-0.9924
3.5	1.030	-0.9466	-0.1192	1.334	0.557	-0.9932
4.0	1.011	-0.9697	-0.0817	1.288	0.493	-0.9922
4.5	1.006	-0.9812	-0.0562	1.269	0.442	-0.9917
5.0	1.006	-0.9868	-0.0382	1.260	0.399	-0.9915
6.0	1.002	-0.9908	-0.0170	1.250	0.333	-0.9917
7.0	1.000	-0.9915	-0.0072	1.247	0.286	-0.9917
8.0	1.000	-0.9917	-0.0027	1.246	0.250	-0.9917
10.0	1.000	-0.9917	-0.0003	1.246	0.200	-0.9917

type orbitals, we ignore the three– and four–site terms in the atomic basis, that represents an uncontrolled approximation. Similar analysis of the existing Hubbard model solution for an infinite chain (Lieb and Wu, 1968) shows the absolute difference $\lesssim 10^{-2}$ Ry in the ground–state energy per site and the relative deviation of order $10^{-4} \div 10^{-3}$ in the values of the model parameters (Kurzyk, Spałek, Wójcik and Rycerz, 2003).

The corresponding results for $N = 10$ atoms in Gaussian basis, when the long–range interactions are included, are presented in Table 3.5. One can notice, that the long–range interaction leads to a relatively small difference between the presented data and those in the Table 3.2. The major contributions to such difference comes from the single–particle potential energy. This explains the necessity of using a quite sophisticated procedure, which is described in Section 3.1.1.

3.3 The ground–state properties

In this Section we analyze basic ground state correlation functions, the electron momentum distribution and the charge–energy gap of a correlated 1D chain of $N = 4 \div 16$ atoms. All the properties are calculated as a function of lattice parameter a in the Gaussian–type STO–3G basis (see Appendix A). We use the optimal values of the inverse orbital size α_{min} obtained from extrapolation of the data for $N = 6 \div 10$, presented in previous Section (*cf.* Table 3.2). The main points of the analysis presented here and in the next Section, are discussed in relation to the *Hubbard model*, for which one has Mott–insulating state in 1D (Lieb and Wu, 1968) and to the *quater–filled* (QF) system with long–range Coulomb interaction, which exhibits highly–conducting behavior (*cf.* Section 3.4).

3.3.1 Spin and charge correlation functions

In Figure 3.4 we present the set of basic correlation functions for the nanochain described by Hamiltonian (2.1), obtained with the EDABI method. The oscillating spin–spin correlation function $\langle \mathbf{S}_i \cdot \mathbf{S}_j \rangle$ illustrates the *antiferromagnetic* nature of the system ground state, particularly for $a/a_0 \gtrsim 3$ (*cf.* Figure 3.4a). The *long-range* character of this order is confirmed by the nearest neighbor spin-spin correlation function $|\langle \mathbf{S}_i \cdot \mathbf{S}_{i+1} \rangle|$, which is almost independent of R, whereas the single-particle correlation function $|\langle a_i^\dagger a_{i+1} \rangle|$ and the average double occupancy $\langle n_{i\uparrow} n_{i\downarrow} \rangle$, decrease exponentially with the increasing R (*cf.* Figure 3.4b, *note* the logarithmic scale of the y-axis). The analysis of the density-density correlation function $\langle \Delta n_i \Delta n_j \rangle$, (where $\Delta n_i \equiv n_i - \bar{n}$ and $\bar{n} = N_e/N$ is the band filling) provides the evidence that the system gradually transforms from a nanoscopic metal to an insulator with growing R. In the half-filed band case (*cf.* Figure 3.4c),

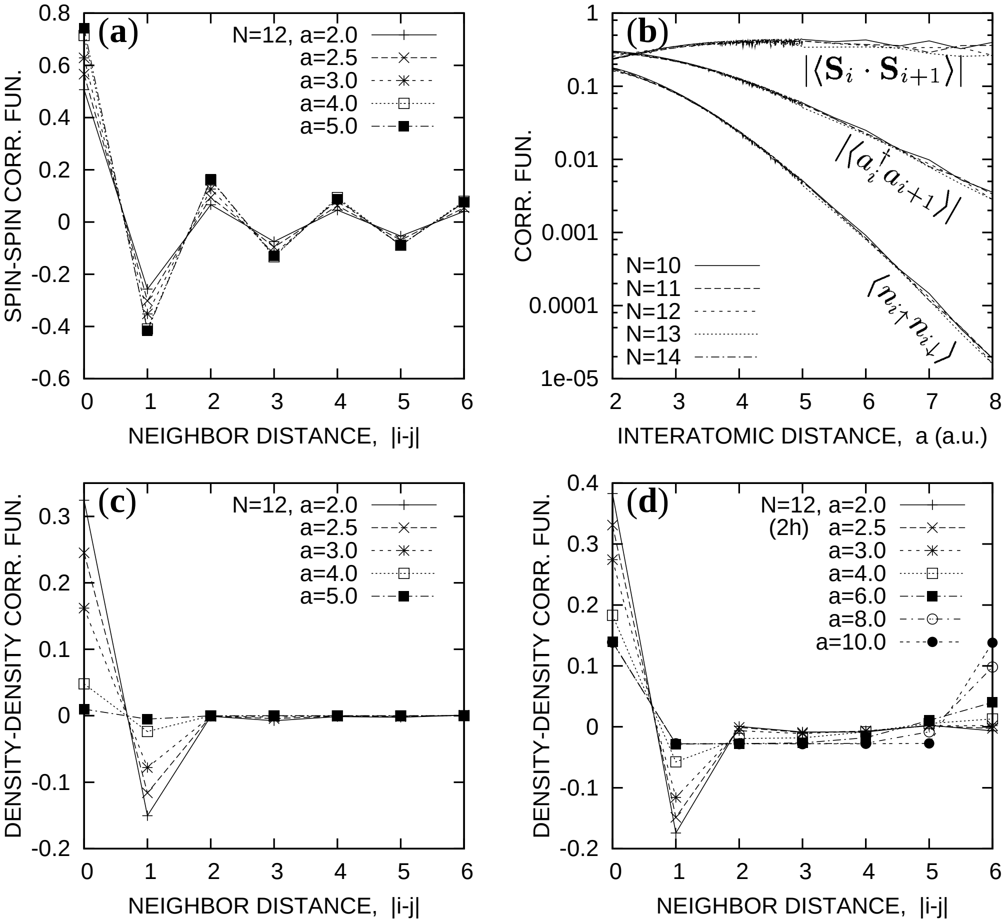

FIGURE 3.4: Basic correlation functions for nanochain: (a) spin–spin correlation function $\langle \mathbf{S}_i \cdot \mathbf{S}_j \rangle$ vs. distance $|i-j|$; (b) absolute values of the nearest neighbor spin–spin $|\langle \mathbf{S}_i \cdot \mathbf{S}_{i+1} \rangle|$, single–particle (hopping) correlation function $|\langle a_i^\dagger a_{i+1} \rangle|$, and average double occupancy per site $\langle n_{i\uparrow} n_{i\downarrow} \rangle$, all vs. interatomic distance a (specified in units of a_0); (c) density–density fluctuation correlation function $\langle \Delta n_i \Delta n_j \rangle$ vs. distance $|i-j|$ for the half–filled band case ($N_e = N$), and (d) for the system containing two holes ($N_e = N - 2$).

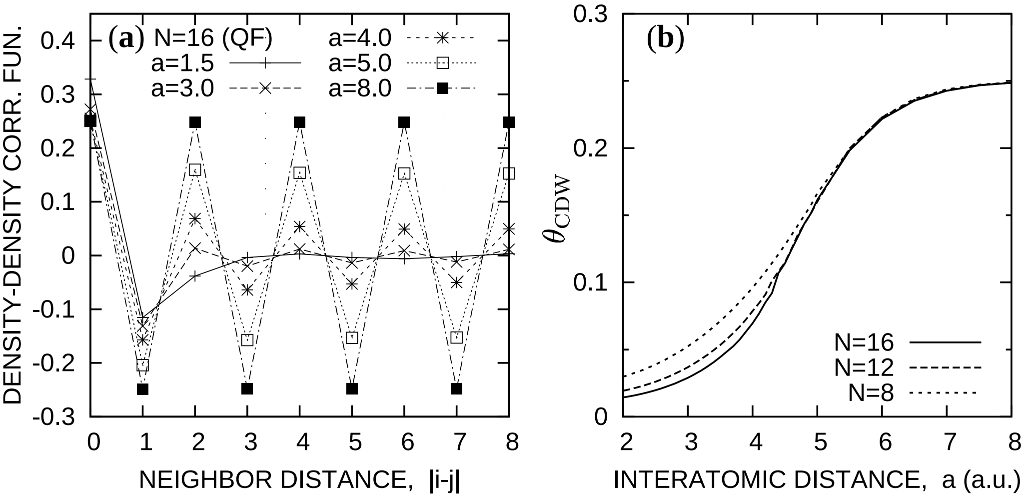

FIGURE 3.5: Charge–density distribution for the *quarter–filled* ($N_e = N/2$) nanochain: (a) density–density fluctuation correlation function $\langle \Delta n_i \Delta n_j \rangle$ vs. distance $|i-j|$, (b) *charge–density wave* order parameter for the alternating density–density fluctuation (*see* main text for the definition) vs. interatomic distance a.

$\langle \Delta n_i \Delta n_j \rangle$ diminishes significantly faster with the distance $|i-j|$ for larger R, whereas for the system containing 2 holes (*cf.* Figure 3.4d) an additional maximum appears at $|i-j| = N/2$ for $a/a_0 \gtrsim 3$; this can be interpret as follows: in the metallic–like regime the added holes are distributed almost uniformly throughout the system to minimize their band energy, whereas in the insulating limit (large R) the Coulomb repulsion dominates, so the minimal energy respects the holes located at the opposite sides of the system (i.e. at $|i-j| = N/2$ for the periodic boundary conditions).

Such crossover behavior is strongly manifested for the *quarter–filled* band case (*cf.* Figure 3.5). In QF chain of $N = 16$ atoms (*cf.* Figure 3.5a) the charge is almost uniformly distributed for $a \lesssim 3a_0$, but charge–density waves are formed rapidly in the range $a/a_0 = 4 \div 5$. The corresponding order parameter, defined as

$$\theta_{\mathrm{CDW}} = \frac{1}{N} \sum_m (-1)^m \langle \Delta n_i \Delta n_{i+m} \rangle , \qquad (3.23)$$

approaches its maximal value $\theta_{\mathrm{CDW}} = 1/4$ for $a \gtrsim 8a_0$ (*cf.* Figure 3.5b). The above transition–like behavior seems similar to MIT observed by Capponi et al. (2000) for spinless fermions, as we note that quarter–filling for $S = 1/2$ electrons corresponds to the half–filled band case for spinless fermions. The correspondence between charge–order transformation described here, and the resulting system conductivity is discussed in Section 3.4.2.

3.3.2 The boundary–condition problem

In the thermodynamic limit the system properties are the same, regardless which boundary conditions are used. Nevertheless, the role of the boundary conditions is of great importance when working with finite clusters. For 1D system at half–filling ($N_e = N$) the so–called modified boundary conditions (MBC) are one possibility (Jullien and Martin, 1982). For MBC, when $N = 4n + 2$ (where n is natural number) true periodic boundary conditions (PBC) are used, whereas for $N = 4n$ one uses instead antiperiodic boundary conditions (ABC). This choice follows from the different behavior of linear clusters with $N = 4n+2$ and $N = 4n$ sites, respectively (Rościszewski and Oleś, 1993; Fourcade and Sproken, 1984). In practice, both PBC and ABC are implemented in a cluster with torus topology (a ring in 1D); namely, the terminal annihilation operators in the Hamiltonian (3.8) are substituted by

$$\begin{cases} a_{N+1,\sigma} \rightarrow a_{1\sigma} & \text{for PBC,} \\ a_{N+1,\sigma} \rightarrow -a_{1\sigma} & \text{for ABC.} \end{cases} \tag{3.24}$$

Therefore, the terminal hopping term involving the end atoms changes sign for ABC, whereas the interaction terms $n_{i\uparrow}n_{i\downarrow}$ and $n_i n_j$ remain unaltered for both PBC and ABC.

The effect of MBC on the ground–state energy E_G of 1D nanochain with long–range Coulomb interactions is illustrated in Table 3.6, where we use the extrapo-

TABLE 3.6: The effect of boundary conditions on the ground–state energies of 1D nanochains when long–range Coulomb interactions are included.

	E_G/N, $N=8$		E_G/N, $N=10$		E_G/N, $N=12$	
a/a_0	PBC	ABC	PBC	ABC	PBC	ABC
1.5	-0.69911	-0.76236	-0.74908	-0.71131	-0.71732	-0.74225
2.0	-0.91386	-0.93660	-0.92973	-0.91767	-0.91927	-0.92633
2.5	-0.97524	-0.98164	-0.97857	-0.97593	-0.97602	-0.97721
3.0	-0.99049	-0.99168	-0.99062	-0.99030	-0.99008	-0.99013
3.5	-0.99256	-0.99270	-0.99234	-0.99232	-0.99216	-0.99217
4.0	-0.99200	-0.99201	-0.99186	-0.99184	-0.99169	-0.99171
4.5	-0.99156	-0.99156	-0.99149	-0.99148	-0.99134	-0.99142
5.0	-0.99143	-0.99148	-0.99144	-0.99143	-0.99130	-0.99135
6.0	-0.99163	-0.99164	-0.99163	-0.99163	-0.99157	-0.99157
7.0	-0.99170	-0.99170	-0.99169	-0.99169	-0.99169	-0.99169
8.0	-0.99169	-0.99169	-0.99169	-0.99169	-0.99169	-0.99169
10.0	-0.99169	-0.99169	-0.99169	-0.99169	-0.99169	-0.99169

lated values of optimal inverse orbital size $\alpha_{\min}$ listed in Table 3.1. The changes of the ground–state energy due to boundary conditions are minimal, particularly for larger system sizes N and lattice parameters a. This is because E_G (and the corresponding α_{min}) is rapidly convergent with N, as it was discussed in Section 3.2.1. However, the choice of boundary conditions may have a significant influence on other physical properties of the finite system. For example, the Drude weight D is negative, when PBC are applied to the half–filled system of $N = 4n$ sites (Fye, Martins and Scalapino, 1991), whereas one can easily keep $D \geqslant 0$ by choosing BC that minimize the ground–state energy (Góra, Rościszewski and Oleś, 1998). We discuss this problem in more detail in Section 3.4.2.

We explain briefly here, why the minimal E_G corresponds to particular boundary conditions by analyzing the situation for noninteracting fermions. But first, we provide the correspondence between MBC and the approach by Kohn (1964) introducing a (fictitious) flux $N\phi$ through a torus representing the lattice with PBC, depicted schematically in Figure 3.6a. Such a flux indicates a vector potential $\mathbf{A}(\mathbf{r})$, having a circulance

$$\oint_C \mathbf{A}(\mathbf{r}) \cdot d\mathbf{l} = N\phi, \tag{3.25}$$

when moving around the lattice sites $j = 1, \ldots, N, N{+}1 \equiv 1$. For discrete–lattice model the vector potential $\mathbf{A}(\mathbf{r})$ can be introduced via a gauge transformation (the *Peierls construction*)

$$a_{j\sigma} \to a_{j\sigma} \exp\left(i \int_{\mathbf{R}_0}^{\mathbf{R}_j} \mathbf{A}(\mathbf{r}) \cdot d\mathbf{r} \right), \tag{3.26}$$

(where $\mathbf{R}_0$ is an arbitrary starting point) which effectively modifies the hopping term in the Hamiltonian (3.8), namely

$$H_t\left[\mathbf{A}(\mathbf{r})\right] = t \sum_j \left[\exp\left(i \int_{\mathbf{R}_j}^{\mathbf{R}_{j+1}} \mathbf{A}(\mathbf{r}) \cdot d\mathbf{r} \right) a_{j\sigma}^{\dagger} a_{j+1\sigma} + \mathrm{HC} \right], \tag{3.27}$$

whereas diagonal and interactions terms do not change again. The only physical information, contained in the phase differences

$$\varphi_{j,j+1} = \int_{\mathbf{R}_j}^{\mathbf{R}_{j+1}} \mathbf{A}(\mathbf{r}) \cdot d\mathbf{r}$$

is the total flux $N\phi$, as the circulance (3.25) can be now written in a phases sum–rule form

$$\sum_j \varphi_{j,j+1} = N\phi. \tag{3.28}$$

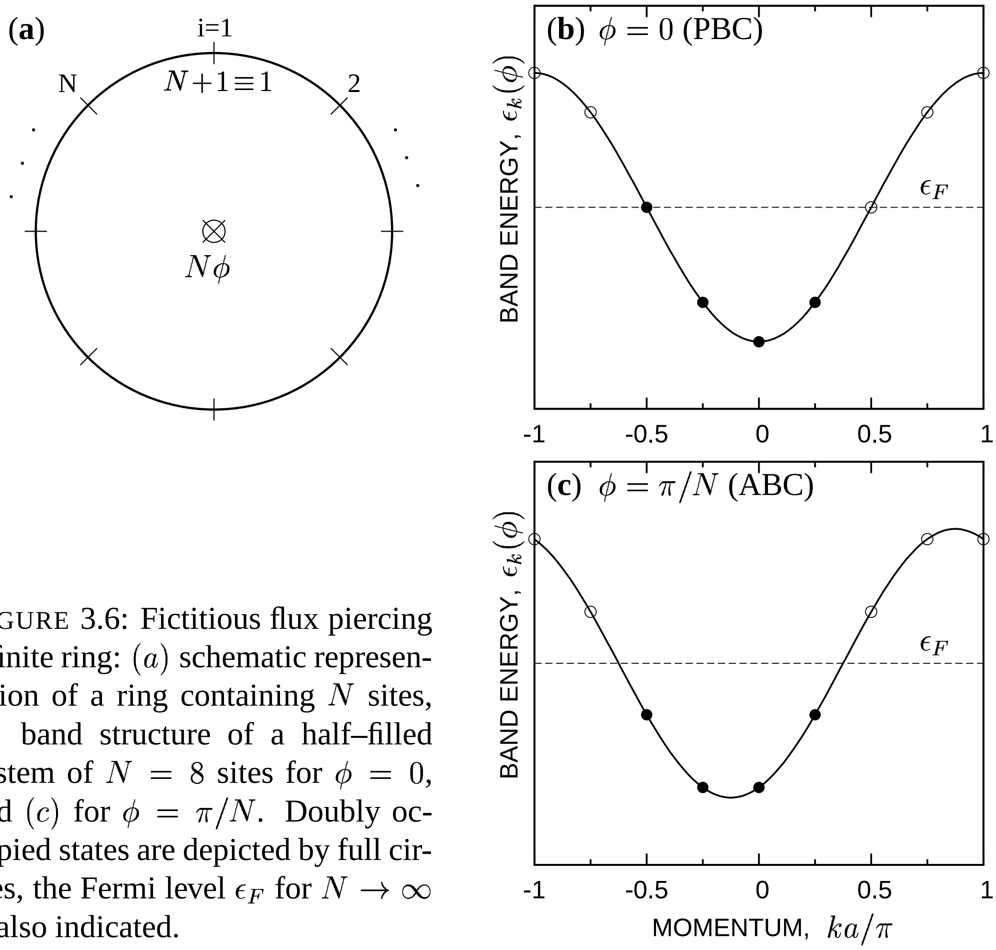

FIGURE 3.6: Fictitious flux piercing a finite ring: (a) schematic representation of a ring containing N sites, (b) band structure of a half–filled system of $N = 8$ sites for $\phi = 0$, and (c) for $\phi = \pi/N$. Doubly occupied states are depicted by full circles, the Fermi level ϵ_F for $N \to \infty$ is also indicated.

Different choices of $\varphi_{j,j+1}$ corresponding to the same sum (3.28) lead to the Hamiltonians (3.27) that are equivalent up to the unitary transformation. This is because vector potential itself is defined up to the gauge transformation

$$\mathbf{A}(\mathbf{r}) \to \mathbf{A}(\mathbf{r}) + \nabla\chi(\mathbf{r}),$$

(where $\chi(\mathbf{r})$ is arbitrary scalar field), so one can have any values of $\varphi_{j,j+1}$ preserving the sum rule (3.28), by simple adjusting $\chi(\mathbf{r})$ appropriately. Thus, one usually choose between two possibilities:

(i) equal phase differences $\varphi_{1,2} = \ldots = \varphi_{N-1,N} = \varphi_{N,1} = \phi$, or

(ii) the phase difference concentrated at a single (i.e. terminal) bond $\varphi_{1,2} = \ldots = \varphi_{N-1,N} = 0$, $\varphi_{N,1} = N\phi$.

Selection (i) is convenient for analytical purposes, as it allows us to study the translationally invariant system in the representation of the same symmetry, whereas

(ii) allows to work in real representation, and speed up numerical computations for $N\phi = 0$ or π. In these special cases, the transformation of the form (3.26) is unitary equivalent to (3.24), namely $\phi = 0$ for PBC and $\phi = \pi/N$ for ABC.

The diagonalization of the single–particle Hamiltonian (3.27) in the representation (i) easily leads to the band energy of the form

$$\epsilon_k(\phi) = 2t\cos(ka + \phi), \tag{3.29}$$

so the eigenvalues of the system in presence of a fictitious flux ϕ are just shifted in the momentum space. In effect, one can define the gauge–invariant momentum

$$Ka = ka + \phi, \tag{3.30}$$

to obtain the dispersion relation (3.29) in the usual form $\epsilon_K = 2t\cos(Ka)$. The illustration for $N = 8$ (so $N = 4n$) and the half–filled band case is provided in Figure 3.6. For $\phi = 0$ (PBC, *cf.* Figure 3.6b) we have a doubly–degenerate state on the Fermi level and system is frustrated. On the contrary, for $\phi = \pi/N$ (ABC, *cf.* Figure 3.6c) we arrive at the closed–shell configuration and this value corresponds to the minimal E_G. For $N = 4n + 2$ the situations is opposite, and one obtain the closed–shell (benzene–like) configuration in case of PBC. One can repeat an analogous consideration in the quarter–filled band case, to obtain that the ground–state energy minima correspond to PBC for $N = 8n + 4$, and to ABC for $N = 8n$, respectively.

The situation reviewed above for noninteracting particles does not change qualitatively, when the interaction is switched on. If only the topology of a Fermi surface is preserved, the rules for choosing between PBC and ABC will remain the same. Problems with applying the optimal boundary conditions become nontrivial in 2D, where various plane cluster configurations were analyzed ((Jaklič and Prelovšek, 2000)). One usually generalizes the equal–phases case (i) and optimizes two fictitious fluxes ϕ_x and ϕ_y to reach the minimum of E_G. Such procedure is, however, beyond the scope of this thesis.

In the remaining part of this Chapter we apply the boundary conditions that minimize the ground–state energy for the particular system size N. Such procedure, apart from providing the correct sign of Drude weight D (*cf.* Section 3.4.2), as we have mentioned already, leads also to a smooth convergence of the charge gap (*cf.* Section 3.3.4) and of the electron momentum distribution (*cf.* next Section). One exclusion is made when analyzing the density of states and the spectral function (*cf.* Section 3.4.1), where we plot the quantities for $N = 12$ using PBC, in order to demonstrate the frustration effect, similar to that shown in Figure 3.6a, but in the case of strongly–interacting system with a Slater gap.

3.3.3 Tomonaga–Luttinger scaling

We discuss now the electron momentum distribution of 1D chain of $N = 6 \div 16$ atoms to determine whether the system is either conducting (*Luttinger–liquid* state) or insulating at the localization threshold. But first, we briefly summarize the basic features of the homogeneous conductors, following Voit (1995).

Fermi liquid theory is based on a notion of quasi–particles evolving out of the particles (holes) of a Fermi gas upon adiabatically switching interactions (Landau, 1957; Landau, 1959; Nozières, 1964). They are in one–to–one correspondence with the bare particles and, specifically, carry the same quantum numbers and obey Fermi–Dirac statistics. The existence of such quasi–particles formally shows up through two main effects:

(i) a nonzero quasiparticle pole strength $z_{\mathbf{k}}$ in a single-particle propagator

$$G(\mathbf{k},\omega) = \frac{z_{\mathbf{k}}}{\omega - (\epsilon_{\mathbf{k}} - \epsilon_F) + i\delta \mathrm{sgn}(k - k_F)} + G_{\mathrm{incoh}}(\mathbf{k},\omega) \tag{3.31}$$

(with the standard notation), which gives them a finite lifetime τ diverging, however, as $\tau \sim (\epsilon_{\mathbf{k}} - \epsilon_F)^{-2}$ as the Fermi surface is approached, so that the quasi–particles are robust against small displacements away from k_F; and

(ii) finite jump Δn_F of the momentum distribution function $n_{\mathbf{k}} = \langle a_{\mathbf{k}}^{\dagger} a_{\mathbf{k}} \rangle$ at the Fermi ridge ($k = k_F$), exactly equal to the inverse quasi–particle mass renormalization $\Delta n_F = z_{k_F}$.

One–dimensional conductors are very special that they retain a Fermi surface (if defined as a set of points where the momentum distribution *or* its derivatives has singularities, see *below*) enclosing the same k–space volume as that of free fermions, in agreement with Luttinger's theorem[1] (Luttinger, 1960). However, there are *no fermionic quasi–particles*, and their elementary excitations are rather bosonic collective charge (*holons*) and spin (*spinons*) fluctuations dispersing with different velocities. An incoming electron decays into such charge– and spin–excitation branches, which then separate spatially with time (the so–called *charge–spin separation*).

To be more specific, salient properties of such 1D conductors include two principal features:

(i) a continuous momentum distribution function, showing the singularity near the Fermi level $k \approx k_F$ in the form (Solyom, 1979)

$$n_{k\sigma} = n_F + A\,|k_F - k|^{\theta}\,\mathrm{sgn}(k_F - k), \tag{3.32}$$

---

[1] This theorem holds true as long as there is no phase transitions (induced by the interaction) in the electron system.

where θ is a non–universal (*interaction–dependent*) exponent; in consequence, it yields the non–existence of fermionic quasi–particles (the quasi–particle residue in (3.31) vanishes as $z_k \sim |k_F - k|^\theta$ when $k \to k_F$);

(ii) similar power–law behavior of all physical properties, particularly of the single–particle density of states $\mathcal{N}(\omega) \sim |\omega - \mu|^\theta$ (*pseudogap*), that imply a finite Drude weight $D > 0$ for $\theta < 1$.

Those properties are generic for 1D conductors, but particularly prominent in a 1D model of interacting fermions (TLM) proposed by Tomonaga (1950) and Luttinger (1963), and solved exactly by Mattis and Lieb (1963) with the help of *bosonisation* technique. The notion of *Luttinger liquid* was coined by Haldane (1981) to describe these universal low–energy properties of gapless 1D quantum systems, and to emphasize that an asymptotic ($\omega \to \mu$, $k \to k_F$) description can be based on the Luttinger model in the same manner as the Fermi liquid theory is based on the concept of an ideal Fermi gas. In the case of lattice models, such as (extended) Hubbard, the Luttinger liquid behavior is predicted by the renormalization group (RG) mapping onto TLM (Solyom, 1979). Through such mapping, one can also expect the convergence of the momentum distribution $n_{k\sigma}$ (discrete for finite N) to the continuous power–law form (3.32) with increasing N. This belief was first checked numerically by Sorella et al. (1990) for the Hubbard model.

Here we present a similar approach to a finite 1D chain with long–range Coulomb interaction, described by the Hamiltonian (3.8). The corresponding electron–momentum distribution for half–filling ($N_e = N$) is depicted in Figure 3.7a in the linear, and in Figure 3.7b in the *log–log* scale. The data for $N = 4n$ (when using ABC) contain the substitution $ka \to ka + \pi/N$ (*cf.* Eq. 3.30), to get the gauge–invariant momentum distribution. In order to extract the exponent θ accurately from the data for finite N, it was necessary to include also the higher scaling corrections. They can be obtained from the Tomonaga mapping in the form of an expansion in power of $\ln(\pi/|k_F - k|a)$,

$$\ln|n_F - n_{k\sigma}| = -\theta \ln z + b \ln\ln z + c + \mathcal{O}(1/\ln z), \tag{3.33}$$

where $z \equiv \pi/|k_F - k|$. This singular form is required by the especially slow approach to the RG fixed point (Solyom, 1979); neglecting logarithmic corrections one can extract from the derivative $d\ln|n_F - n_{k\sigma}|/d\ln z$ the asymptotic form (3.32) for $k \approx k_F$. Solid lines in Figures 3.7a and 3.7b represent the formula (3.33), the best fitted values of the parameters θ, b and c are listed in Table 3.7. The exponent θ is also ploted in Figure 3.7c as a function of the lattice parameter a showing, that it crosses the critical value $\theta = 1$ (corresponding to the metal–insulator boundary in 1D) for $a_{\text{crit}} = 2.60a_0$. We also provide *residual sum of squares* (*cf.* inset in Figure 3.7c) to show, that a quality of the fit (3.33) is worst for $a \approx a_{\text{crit}}$, where the system is close to the metal–insulator transition.

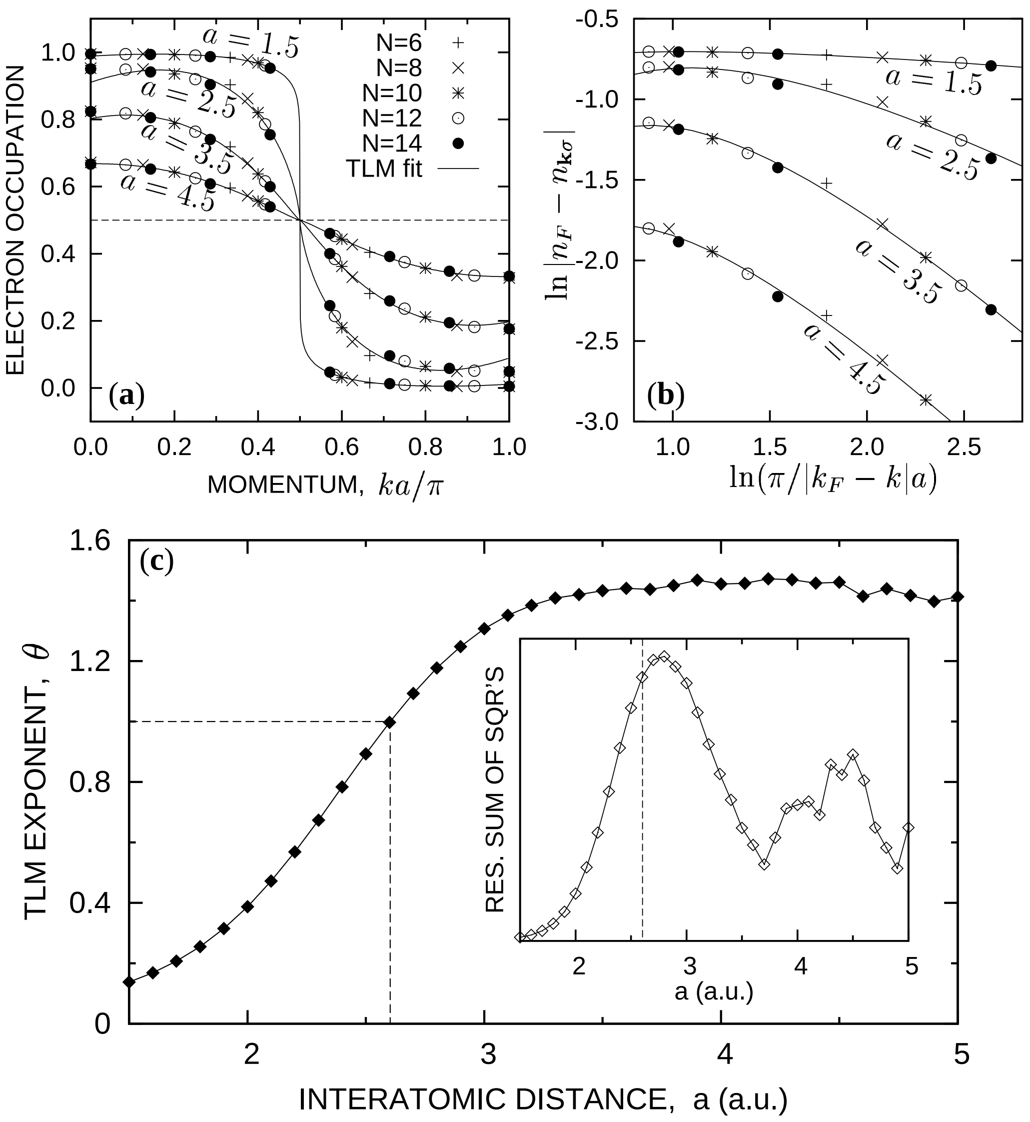

FIGURE 3.7: Luttinger–liquid scaling for a *half–filled* 1D chain of $N = 6 \div 14$ atoms with *long–range* Coulomb interactions: (a) momentum distribution for electrons in the linear and (b) log–log scale, continuous lines represent the fitted singular expansion in powers of $\ln(\pi/|k_F - k|a)$ (see main text for details); (c) Tomonaga–Luttinger model exponent θ vs. lattice parameter a (specified in a_0) and (in the *inset*) the corresponding residual sum of squares. The solid lines in Figures (a) and (b) represent the TLM fitting of Eq. (3.33).

TABLE 3.7: The fitted parameters of the singular expansion (3.33) for the electron momentum distribution in the half–filled 1D chain with inclusion of long–range Coulomb interactions. The standard deviation σ is also specified in each case.

a/a_0	θ	$\sigma(\theta)$	b	$\sigma(b)$	c	$\sigma(c)$
1.5	0.138	0.015	0.147	0.024	-0.567	0.015
2.0	0.387	0.055	0.425	0.089	-0.346	0.053
2.5	0.893	0.122	0.971	0.196	0.084	0.118
3.0	1.307	0.128	1.315	0.207	0.357	0.125
3.5	1.433	0.085	1.264	0.137	0.262	0.082
4.0	1.455	0.186	1.113	0.299	-0.032	0.180
4.5	1.462	0.109	1.057	0.176	-0.384	0.106
5.0	1.413	0.133	0.943	0.214	-0.823	0.129

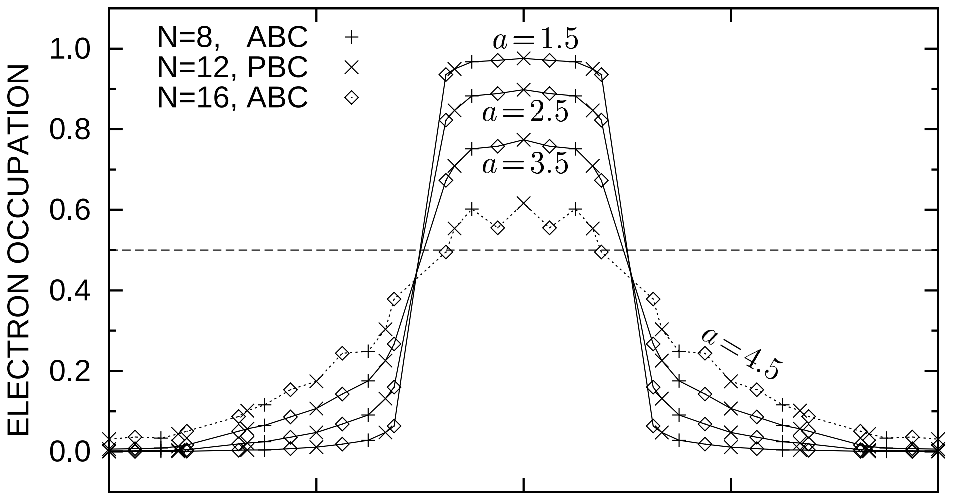

FIGURE 3.8: Momentum distribution $n_{k\sigma}$ for electrons on a chain of $N = 8 \div 16$ atoms in the *quarter–filled* band case ($N_e = N/2$). Lines are drawn as a guide to the eye only. Values of the lattice parameter a are specified in units of a_0.

TABLE 3.8: The fitted parameters of the singular expansion (3.33) for half–filled 1D chain described by the Hubbard model.

a/a_0	θ	$\sigma(\theta)$	b	$\sigma(b)$	c	$\sigma(c)$
1.5	0.229	0.030	0.237	0.048	-0.537	0.029
2.0	0.803	0.100	0.855	0.162	-0.078	0.097
2.5	1.283	0.109	1.259	0.176	0.217	0.106
3.0	1.420	0.075	1.230	0.121	0.116	0.073
3.5	1.415	0.048	1.083	0.078	-0.163	0.047
4.0	1.436	0.069	1.033	0.111	-0.456	0.067
4.5	1.445	0.166	1.000	0.268	-0.801	0.161
5.0	1.371	0.037	0.873	0.060	-1.218	0.036

The electron momentum distribution for the quarter–filled band case ($N_e = N/2$) is shown in Figure 3.8. The available number of datapoints was too small to fit the singular formula (3.33) to a reasonable accuracy, so the lines in the plot are the guide to the eye only. However, the smooth behavior of the Luttinger–liquid type is evident for $a \lesssim 4a_0$, whereas it changes dramatically for the larger values of a. The correspondence with the charge–density wave transition mentioned in Section 3.3.1 seems also visible.

The results for the half–filled *Hubbard model*, presented for comparison in Figure 3.9 (and in Table 3.8) are qualitatively very similar to those in Figure 3.7 (when the long–range interactions are included). The critical value of the lattice parameter $a_{\text{crit}} = 2.16a_0$ also does not differ drastically from the previous one. This is because such nanoscopic systems may always show a conducting behavior in the large–density limit as the external electron tunnels through a finite potential barrier. Therefore, such half–filled band systems, both with– and without inclusion of the long–range interactions can be regarded as close to the metal–insulator transition, with no contradiction to the RG result by Fabrizio (1996). This discussion is completed by the calculation of the charge–energy gap in the next section, as well as of the system spectral function and the conductivity in Section 3.4.

The above results illustrate the important role of choosing appropriate boundary conditions when studying such nanoscopic systems. Similar analysis performed entirely for PBC has lead to quite different physical conclusions (Rycerz and Spałek, 2003a). Namely, we obtained the Fermi–ridge discontinuity and a quasiparticle mass divergence at the localization (MIT) threshold.

The situation depicted in this section does not settle completely the issue of applicability of the Tomonaga–Luttinger concepts to nanoscopic chains. Namely,

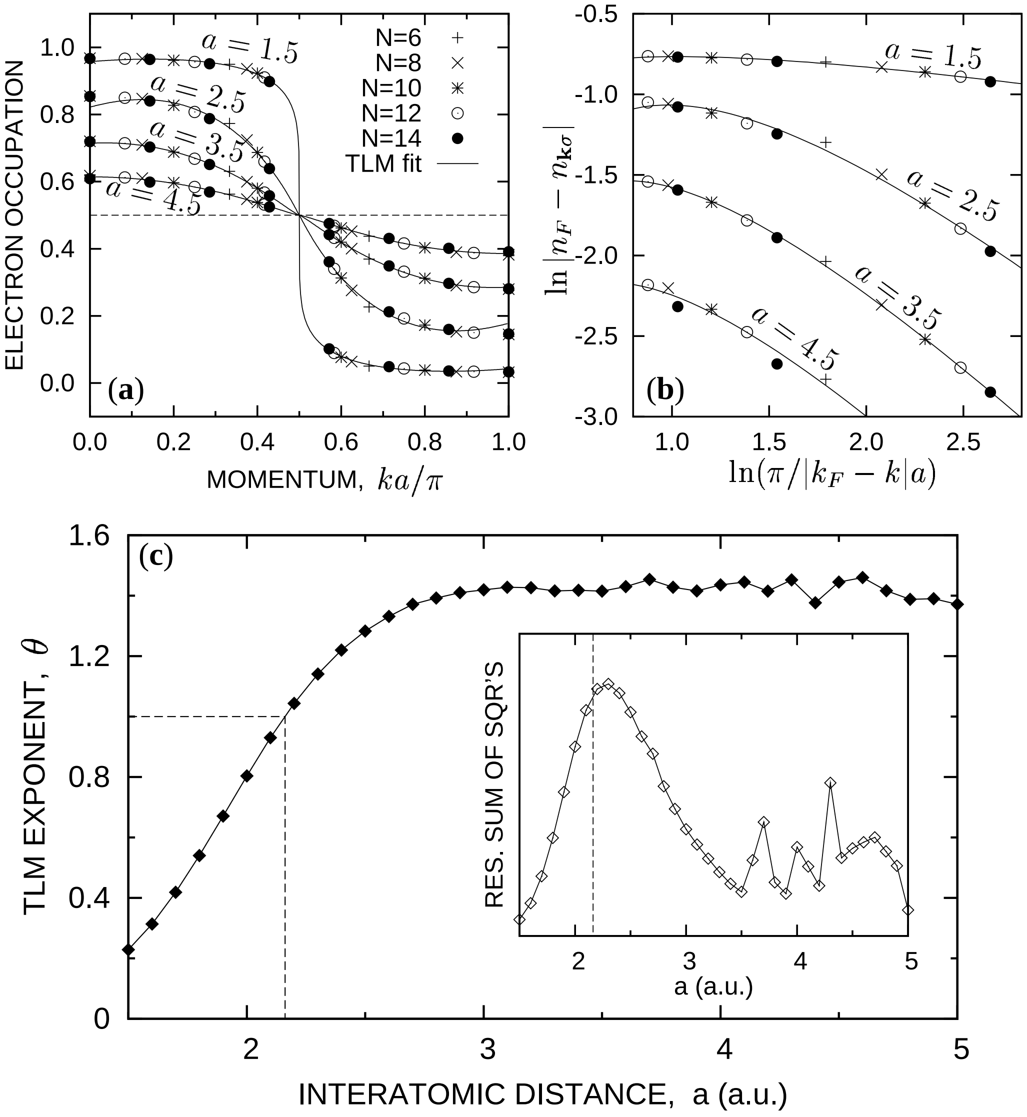

FIGURE 3.9: Luttinger–liquid scaling for half–filled 1D chain described by the Hubbard model: (a) momentum distribution for electrons in the linear and (b) log–log scale, continuous lines represent the fitted singular expansion (3.33); (c) Tomonaga–Luttinger model exponent θ vs. lattice parameter a (specified in a_0) and (in the *inset*) the corresponding residual sum of squares.

the Tomonaga–Luttinger distribution function (3.32) is, strictly speaking, valid only close to the Fermi surface, where $|k - k_F| \ll k_F$. As one can see from Figures 3.7a and 3.9a, there are no points very close to k_F. Additionally, the fitting of the theoretical expansion (3.33) is definitly worse deeply below the Fermi surface. Under these circumstances, our older interpretation (Spałek and Rycerz, 2001; Rycerz, Spałek, Podsiadły and Wójcik, 2002; Rycerz and Spałek, 2003a) seems plausible, but only for the half–filled band case. On this basis, one can clearly see that we need to extend our approach to larger N in order to distinguish between the Fermi– and TL–liquid concepts in a clear fashion. This fundametal problem will be critically reviewed by us in the near future.

3.3.4 Finite–size scaling estimate of MIT

For a further verification, whether the system is metallic or insulating in the Luttinger–liquid like regime presented in previous section, we perform an extrapolation with $1/N \to 0$ of the charge–gap defined (for the *half–filling*) as

$$\Delta E_C(N) = E_G^{N+1} + E_G^{N-1} - 2E_G^N, \tag{3.34}$$

where $E_G^{N_e}$ is the ground-state energy of the system containing N_e electrons. The corresponding numerical results are shown in Figure 3.10. The extrapolation with $1/N \to 0$ performed using the 2–nd and the 3–rd order polynomials provides nonzero value of ΔE_C for any lattice parameter a; only for the lowest examined value $a = 1.5a_0$, $E_G^{N_e}$ reaches zero within the extrapolation error; for other values, it is nonzero. The gap also is significantly smaller than the corresponding Hartree–Fock (HF) value, in the regime $a \lesssim 4.5a_0$, that suggests some kind of reorganization of the dielectric state, e.g. from the Slater– to the Mott–type, as discussed for parametrized models by Resta and Sorella (1999) and by Korbel, Wójcik, Klejnberg, Spałek, Acquarone and Lavagna (2003). This hypothesis is verified by estimating the system conductivity in Section 3.4.2. One should also note the finite–size scaling on ΔE_C seems to be quite insensitive on the boundary conditions, namely the independent parabolic extrapolations with $1/N \to 0$ for $N = 4n$ and $N = 4n + 2$, when PBC are using (Rycerz and Spałek, 2003b), lead to the results which are very close to those presented in Figure 3.10.

The situation becomes completely different when we consider the *quarter–filled* band case $N_e = N/2$ (*cf.* Figure 3.11). The parabolic extrapolation with $1/N \to 0$ provides now the value of the charge–gap $\Delta E_C \approx 0$ (within the errorbars) for lattice parameter $a \lesssim 2a_0$. In the range of $a/a_0 = 2.5 \div 4.5$ the gap reaches nonzero values (significantly greater than the corresponding errorbars), but random dispersion of the datapoints suggests instability of the performed extrapolation due to nonanalytic behavior of ΔE_C when the system is close to the

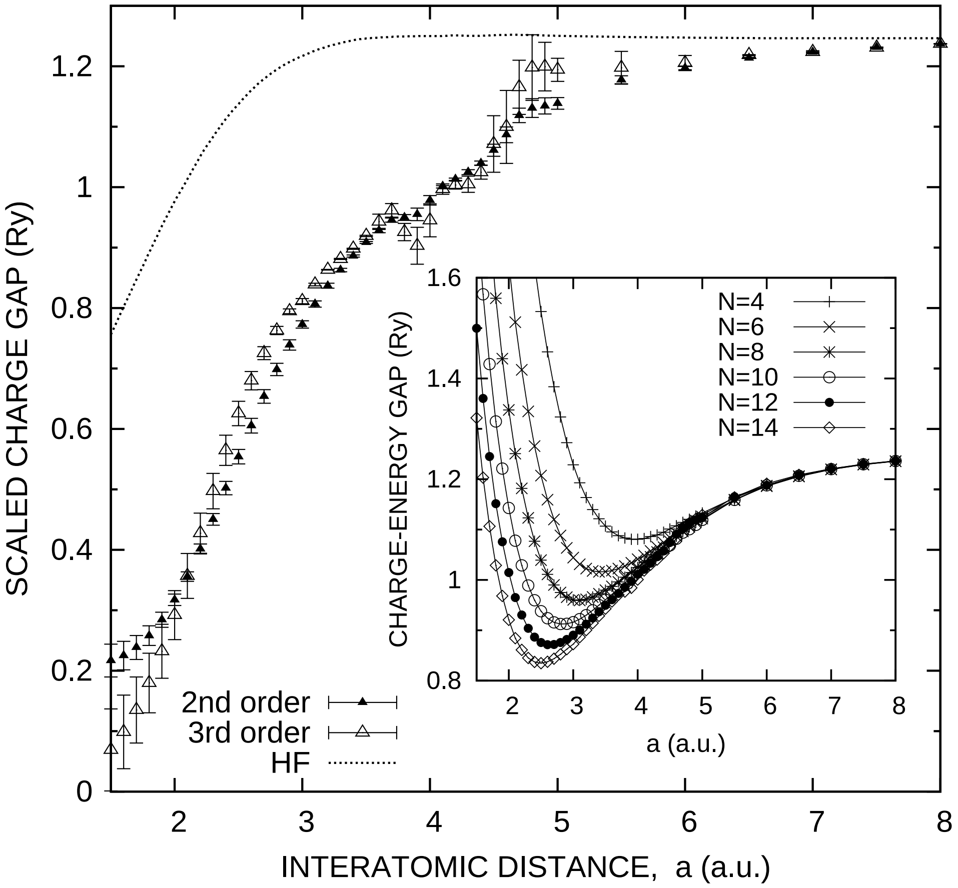

FIGURE 3.10: Charge–energy gap obtained through finite–size scaling for the chains of $N = 4 \div 14$ atoms. The 2–nd and the 3–rd order polynomials have been fitted to perform the extrapolation with $1/N \to \infty$. The corresponding Hartree–Fock value (the Slater gap) for an infinite system is also drawn (*dotted* line). The *inset* exhibits the original data used for the scaling.

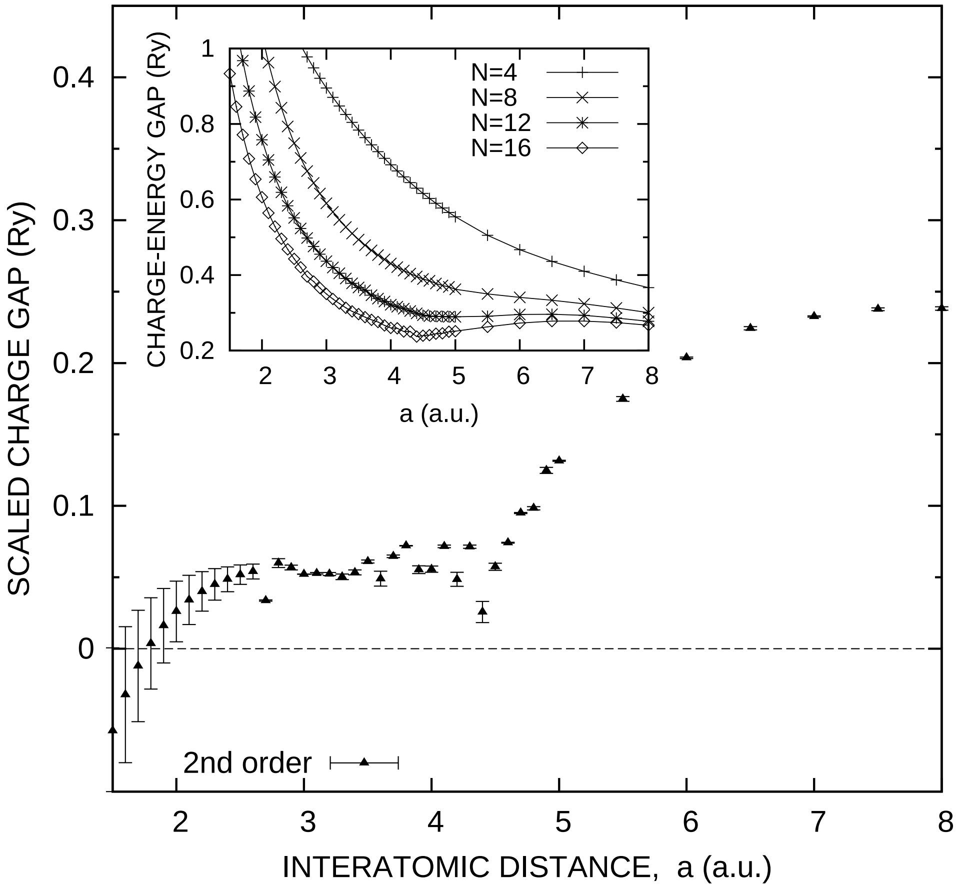

FIGURE 3.11: Charge–energy gap obtained through finite–size scaling for the chains of $N = 4 \div 16$ atoms in the *quarter–filled* band case. The 2–nd order polynomial has been fitted to perform the extrapolation with $1/N \to \infty$. *Inset* provides the original data used for the scaling.

metal–insulator transition. For $a \gtrsim 4.5a_0$ the gap smoothly grows to a nonzero value corresponding to the insulating charge–density wave state, identified in Section 3.3.1. The more precise position of the MIT point is determined in Section 3.4.2, where we calculate the Drude weight for the system.

3.4 Spectral and transport properties

In this Section we utilize the standard method of calculating dynamical properties within the Lanczos algorithm (*cf.* Section 2.2.2) to determine the single–particle density of states, the spectral function, the charge stiffness, and the optical conductivity of a correlated 1D chain of $N = 6 \div 16$ atoms. We analyze the evolution of all these properties with the lattice parameter a in the framework of EDABI method (*cf.* Section 2.1). As in previous Section, we use optimal values of the inverse orbital size α_{min} obtained in Section 3.1.2 (*cf.* Table 3.1) for the Gaussian–type STO–3G basis (see Appendix A), and discuss the main points in relation to the similar system described by the Hubbard model, as well as apply it to the quarter–filled system with long–range Coulomb interactions.

3.4.1 Spectrum of single–particle excitations

The evolution of the single-particle density of states $\mathcal{N}(\omega) = \sum_{\mathbf{k}} A(\mathbf{k}, \omega)$, where $A(\mathbf{k}, \omega)$ is the spectral function, with the increasing a is shown in Figure 3.12 for

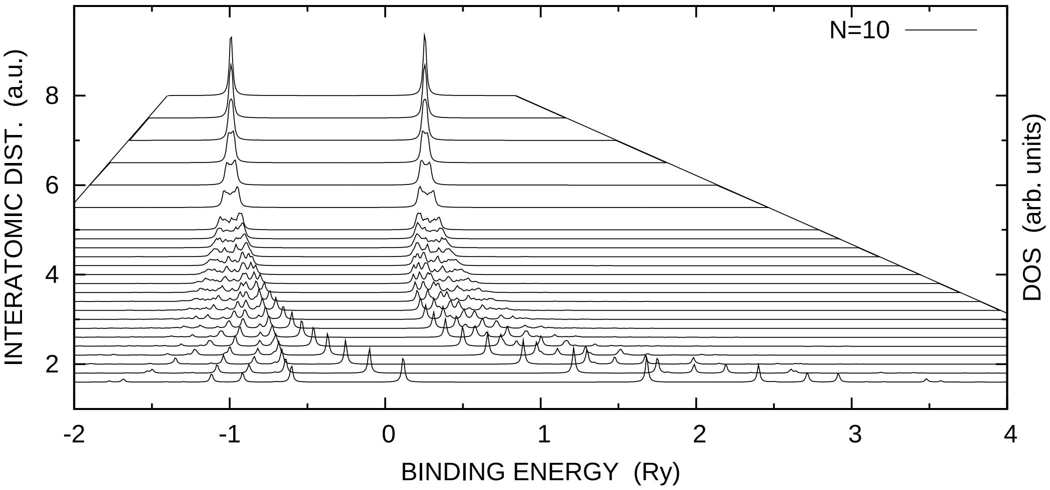

FIGURE 3.12: Single–particle density of states $\mathcal{N}(\omega) = \sum_{\mathbf{k}} A(\mathbf{k}, \omega)$ for 1D chain of $N = 10$ atoms in the *half–filled* band case. *Note* the pronounced incoherent spectrum for $a/a_0 = 3 \div 4$.

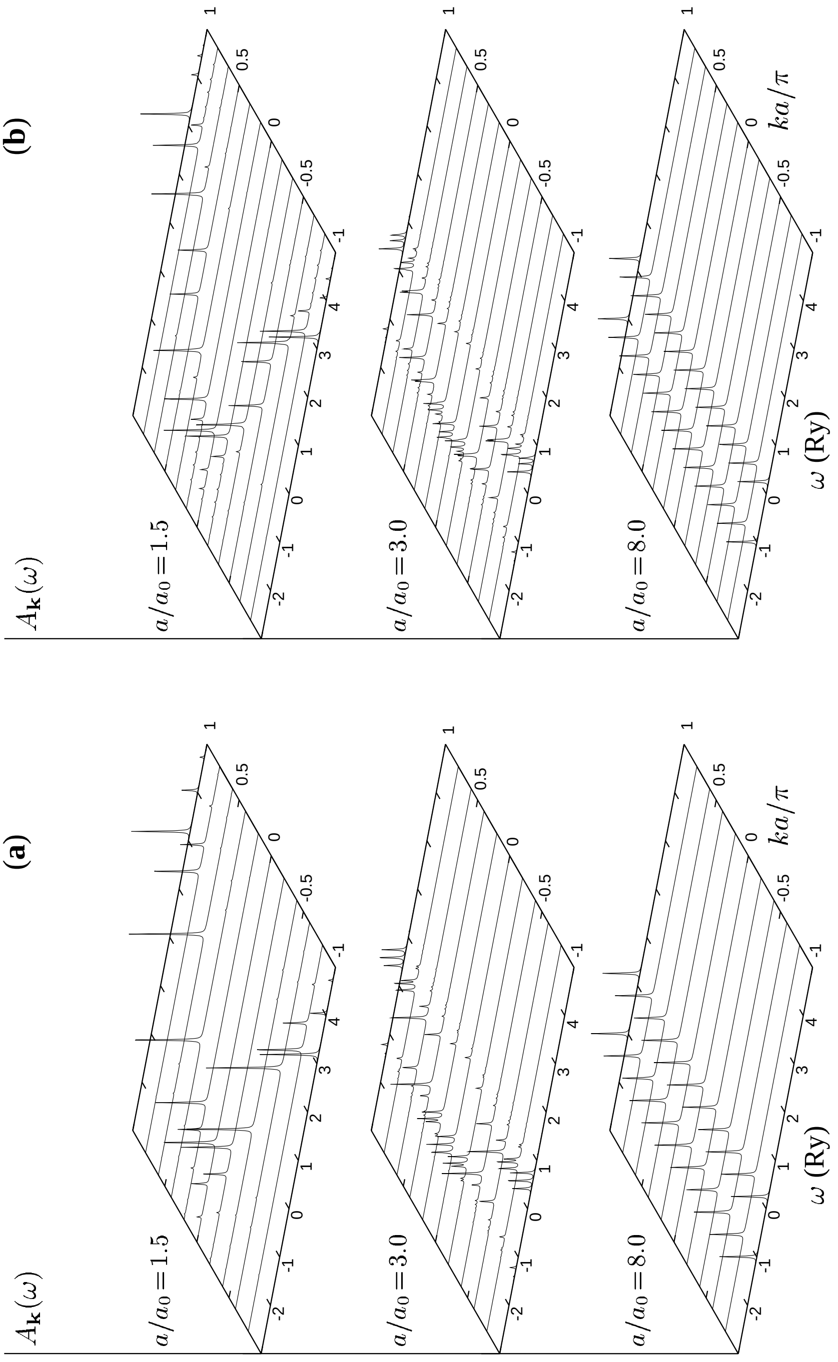

FIGURE 3.13: Spectral functions $A(\mathbf{k}, \omega)$ for the 1D chains of $N = 10$ (a) and $N = 12$ (b) atoms. True periodic boundary conditions (PBC) are used in both cases. *Note* a clear band dispersion curves for $a = 1.5a_0$.

the *half–filled* ($N_e = N$) system described by the Hamiltonian (3.8). The spectral function is defined in the standard manner (*cf.* Eq. 2.24), i.e.

$$A(\mathbf{k},\omega) = \sum_n \left|\left\langle \Psi_n^{N\pm1}\right| c^{\pm}_{\mathbf{k}\sigma} \left|\Psi_0^N\right\rangle\right|^2 \delta\left[\omega - \left(E_n^{N\pm1} - E_0^N\right)\right], \tag{3.35}$$

where the upper (lower) sign correspond to $\omega > \mu$ ($\omega < \mu$), respectively, $|\Psi_n^N\rangle$ is the n-th eigenstate of the system containing N particles, E_n^N is the corresponding eigenenergy, and the matrix element $\langle\Psi_n^{N\pm1}|c^{\pm}_{\mathbf{k}\sigma}|\Psi_0^N\rangle$, with $c^{+}_{\mathbf{k}\sigma} \equiv a^{\dagger}_{\mathbf{k}\sigma}$ and $c^{-}_{\mathbf{k}\sigma} \equiv a_{\mathbf{k}\sigma}$, is calculated within the Lanczos technique set up by Dagotto (1994) and described in details in Section 2.2.2 (*cf.* Eq. 2.29). For plotting purposes we have used analytical representation of Dirac delta (2.25) with $\epsilon = 0.01$ Ry. In the metallic range ($a \lesssim 2.5a_0$) the quasiparticle peaks are well defined, but an incoherent tail is always present and grows in strength with the increasing a. In effect, in the intermediate regime of $a/a_0 = 3 \div 4$ the lower and the upper Hubbard bands are formed, which, in turn, continuously evolve into discrete atomic levels located at the positions $\omega = \epsilon_a$ and $\omega = \epsilon_a + U$, when $a \to \infty$. Those limiting peak positions correspond to the ground (H^0) and excited (H^-) atomic states. Probably, the most interesting feature of this spectrum is its incoherent nature for $a \sim 3a_0$, where the band and the interaction energies are comparable and where the Luttinger liquid exponent cross the critical value $\theta = 1$ (*cf.* Section 3.3.3) corresponding to the metal–insulator boundary.

Additional illustration of the spectrum evolution is provided by the spectral functions plotted in Figure 3.13. The chain of $N = 10$ atoms (or generally $N = 4n + 2$), for which there are no quasiparticle states at the Fermi level, can be regarded as a nanoscopic metal in the small a limit, since the separation between the single–particle levels are mainly determined by the geometrical quantization of their momenta (cf. *top panel* in Fig.3.13a, where a clear band dispersion can be seen). For $N = 12$ ($N = 4n$), however, the situation is slightly different, as the states at the Fermi level are split (cf. *top panel* in Fig.3.13b). This phenomenon looks like the presence of Slater–split states at the Fermi level, but may also appear as a signature of the charge–spin separation in 1D system, *cf.* Voit (1995). We do not use here antiperiodic boundary conditions for $N = 4n$, as discussed in Section 3.3.2, to illustrate the frustration of the same type as depicted schematically in Figure 3.6b, here encoutered for a correlated system treated in a rigorous manner.

3.4.2 Charge stiffness and optical conductivity

We start the discussion with the real part of the optical conductivity $\sigma(\omega)$ at zero temperature (Shastry and Sutherland, 1990; Millis and Coppersmith, 1990), which is determined by the real part of the linear response to the applied electric field, and can be written as

$$\sigma(\omega) = D\delta(\omega) + \sigma_{\text{reg}}(\omega), \tag{3.36}$$

where the regular part is

$$\sigma_{\text{reg}}(\omega) = \frac{\pi}{N} \sum_{n \neq 0} \frac{\left| \langle \Psi_n | \, j_p \, | \Psi_0 \rangle \right|^2}{E_n - E_0} \delta \left(\omega - (E_n - E_0) \right), \tag{3.37}$$

whereas the Drude weight (*charge stiffness*) D is given by

$$D = -\frac{\pi}{N} \langle \Psi_0 | \, H_t \, | \Psi_0 \rangle - \frac{2\pi}{N} \sum_{n \neq 0} \frac{\left| \langle \Psi_n | \, j_p \, | \Psi_0 \rangle \right|^2}{E_n - E_0}, \tag{3.38}$$

with the hopping term H_t as in Eq. (3.8) and the current operator

$$j_p = it \sum_{j\sigma} (a_{j\sigma}^\dagger a_{j+1\sigma} - a_{j+1\sigma}^\dagger a_{j\sigma}). \tag{3.39}$$

Here the states $|\Psi_n\rangle$ in Eqs. (3.37) and (3.38) are the eigenstates of Hamiltonian (3.8) corresponding to the eigenenergies E_n, with boundary conditions that minimize the ground–state energy for a given system size N (*cf.* Section 3.3.2).

The total integrated spectral weight under $\sigma(\omega)$ satisfies the well–known sum rule (Maldague, 1977)

$$\int_0^\infty \sigma(\omega) d\omega = -\frac{\pi}{2N} \langle \Psi_0 | \, H_t \, | \Psi_0 \rangle, \tag{3.40}$$

(note that $\int_0^\infty \delta(\omega) d\omega = 1/2$). Using the Hellmann–Feynman relation,

$$\langle \Psi_0 | \, H_t \, | \Psi_0 \rangle = t \frac{\partial}{\partial t} E_G, \tag{3.41}$$

one can independently obtain $\langle \Psi_0 | \, H_t \, | \Psi_0 \rangle$ from the ground–state energy E_G (Baeriswyl, Carmelo and Luther, 1986).

As originally noted by Kohn (1964), the Drude weight D can be calculated from the dependence of the ground–state energy on fictitious flux ϕ, passing through the system (*cf.* Section 3.3.2)

$$D = \frac{\pi}{N} \left. \frac{\partial^2 E_G(\phi)}{\partial \phi^2} \right|_{\phi=0}, \tag{3.42}$$

which can be shown to be equivalent to the expression of Eq. (3.38). Namely, expanding the single–particle Hamiltonian $H_t(\phi)$ of the form (3.27) in the equal–phases case

$$\int_{\mathbf{R}_j}^{\mathbf{R}_{j+1}} \mathbf{A}(\mathbf{r}) \cdot d\mathbf{r} \equiv \phi,$$

we obtain for small ϕ

$$H_t(\phi) = t\sum_{j\sigma}\left(e^{i\phi}a^\dagger_{j\sigma}a_{j+1\sigma} + e^{-i\phi}a^\dagger_{j+1\sigma}a_{j\sigma}\right) \approx$$
$$t\sum_{j\sigma}\left[\left(1+i\phi-\phi^2/2\right)a^\dagger_{j\sigma}a_{j+1\sigma} + \left(1-i\phi-\phi^2/2\right)a^\dagger_{j+1\sigma}a_{j\sigma}\right]. \tag{3.43}$$

Since the interaction terms in the Hamiltonian (3.8) do not change when ϕ is introduced, we can write down (up to a constant)

$$H(\phi) = H_t(\phi) + H_{\text{int}} \approx H(0) + \phi j_p - \frac{1}{2}\phi^2 H_t, \tag{3.44}$$

where we have used the current operator j_p given by Eq. (3.39). Applying the second–order perturbation scheme to $H(\phi)$, in order obtain the ground–state energy $E_G(\phi)$ up to $\sim \phi^2$ terms, we arrive at

$$E_G(\phi) \approx E_G(0) + \phi\left\langle\Psi_0\right| j_p \left|\Psi_0\right\rangle - \frac{\phi^2}{2}\phi\left\langle\Psi_0\right| H_t \left|\Psi_0\right\rangle - \phi^2\sum_{n\neq 0}\frac{\left|\left\langle\Psi_n\right| j_p \left|\Psi_0\right\rangle\right|^2}{E_n - E_0}. \tag{3.45}$$

Substituting Eq. (3.45) to the definition (3.42) and differentiating, one can easily obtain the expression (3.38).

The above derivation is formally valid for both PBC and ABC cases, provided that terminal hopping terms in Eq. (3.39) and (3.43) could be appropriately redefined according to (3.24). However, one should carefully check, which boundary conditions correspond to the mimimal E_G for a given system size N, because otherwise the perturbation scheme (and the linear response theory itself) fails, leading e.g. to the negative value of D. Following the discussion in Section 3.3.2, for 1D systems, we choose PBC for $N = 4n + 2$ and ABC for $N = 4n$. The averages in Eq. (3.38) are estimated within the Lanczos method as set up by Dagotto (1994) and described in Section 2.2.2 (*cf.* Eq. 2.29).

Kohn (1964) provided also a general argument that, in the limit of large N, D would be vanishing exponentially for an insulating system. It should remain finite, however, for a metallic system, giving the effective ratio of the number of carriers per site $\bar{n}$ to their effective mass m. Namely, by integrating the band energy (3.29) in the range $-k_F \leqslant k \leqslant k_F$ (where the Fermi momentum $k_F = \pi\bar{n}/2a$ does not depend on ϕ, supposing that the flux is adiabatically switched on) we get for noninteracting electrons:

$$\frac{E_G(\phi)}{N} = \sum_\sigma \frac{1}{2\pi}\int_{-k_F}^{k_F}\epsilon_k(\phi)d\phi = \frac{8t}{\pi}\sin\frac{\pi\bar{n}}{4}\cos\left(\phi - \frac{\pi\bar{n}}{4}\right) \tag{3.46}$$

Differentiating Eq. (3.46) with respect to ϕ. one can easily obtain the well–known Drude formula

$$D = \frac{\pi e^2 \bar{n}}{m} \overset{\text{a.u.}}{=} 2\pi \bar{n}\,|t|\,,$$

as the carrier mass $m = 1/2|t|$ in atomic units. Therefore, one can use the Drude weight D as a characteristic of the metal–insulator transition.

For finite system of N atoms D is always nonzero due to a finite tunneling probability through a potential barrier of a finite width. Because of that, the finite–size scaling with $1/N \to \infty$ has to be performed for D. Here we use, following Góra et al. (1998) the parabolic extrapolation

$$\ln|D^*_N| = a + b(1/N) + c(1/N)^2, \tag{3.47}$$

where D^*_N denotes the *normalized Drude weight*

$$D^* = -\frac{N}{\pi}\frac{D}{\langle H_t\rangle} \tag{3.48}$$

for the system of N sites (the averaging takes place for the ground state $|\Psi_0\rangle$), that provides the value in the range $0 \leqslant D^* \leqslant 1$, and thus can be regarded as an order parameter for MIT.

The results for 1D system of $N = 6 \div 14$ atoms in the *half–filled* band case are shown in Figure 3.14. We present, for comparative purposes, the data for the system with long–range Coulomb interaction (*cf.* Figure 3.14a) together with those corresponding to the Hubbard model (*cf.* Figure 3.14b). All the values of D^*_N used for the scaling (3.47) are gathered in Tables 3.9 and 3.10 together with resulting D^*_∞ and its relative errors (we stop at the lattice parameter a for which $D^*_\infty = 0$ in the range of errorbars). In both the cases of long–range (*cf.* Table 3.9) and on–site (*cf.* Table 3.10) interaction, the extrapolated Drude weight D^*_∞ become significantly grater then zero (of 2σ value) only for small lattice parameters $a \leqslant 2.6a_0$ and $a \leqslant 2.1a_0$, respectively. The limiting values match those obtained in Section 3.3.3, for which the Luttinger–liquid exponent cross the critical values $\theta = 1$, corresponding to the metal–insulator boundary. The above results suggests transition–like behavior in such 1D systems at half–filling, however, the optical conductivity $\sigma_{\text{reg}}(\omega)$, drawn in Figure 3.15, shows the isolated Hubbard peak at $\omega \approx U$ and no interband transitions present in conducting system. Due to this fact, and to the nonzero value of the charge–gap for any a (*cf.* Section 3.3.4), one should regard both the half–filled systems studied here as the Mott–insulators in the large N limit.

The situation become again completely different at *quarter–filing* (QF). The normalized Drude weight of QF systems of $N = 8 \div 16$ atoms, depicted in Figure 3.16a, shows a highly–conducting behaviour ($D^* \approx 1$) for $a \lesssim 3.5a_0$ and gradually

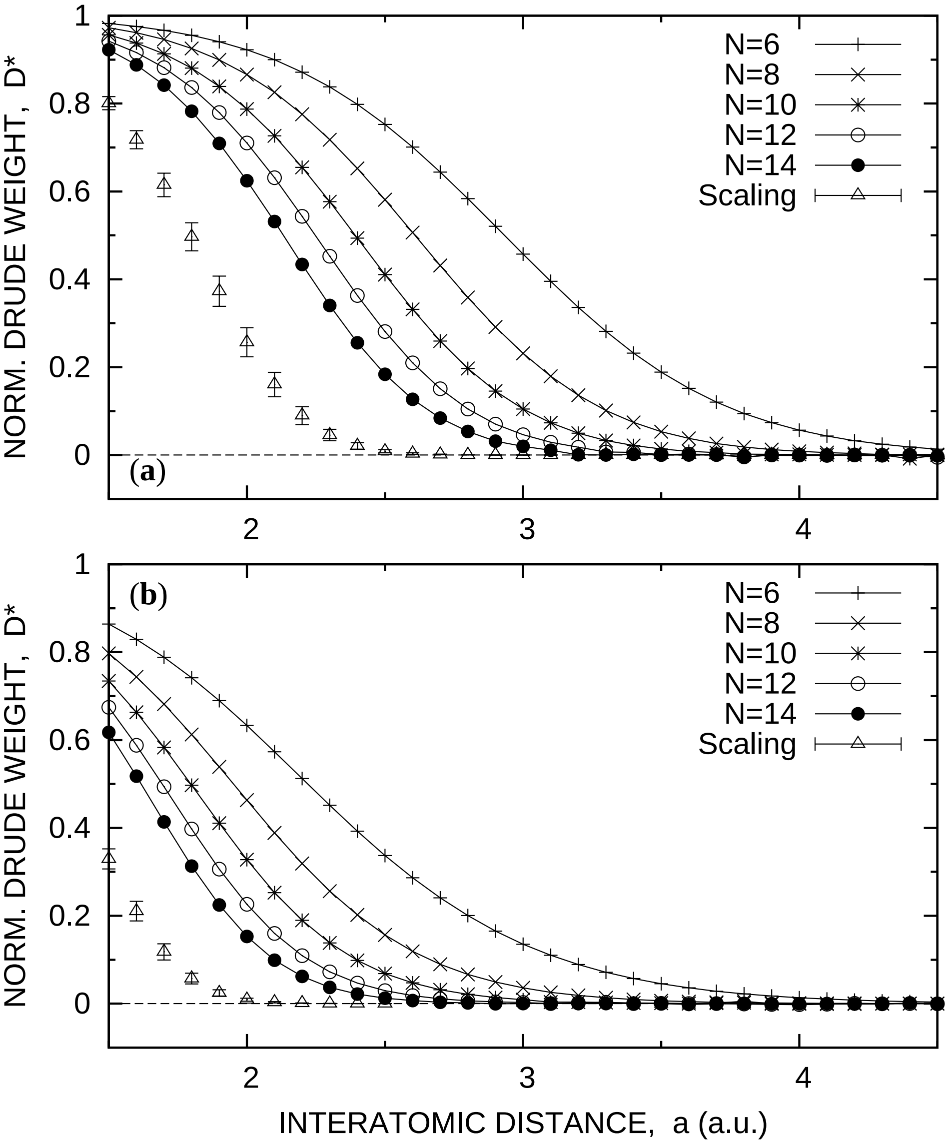

FIGURE 3.14: The normalized Drude weight for 1D system in the *half–filled* band case with the long–range Coulomb interactions (a) and with the Hubbard U term only (b). The values of D^*_∞ obtained through finite size scaling with $1/N \to \infty$ are also provided. True periodic boundary conditions (PBC) are used for $N = 4n + 2$, the antiperiodic (ABC) for $N = 4n$.

TABLE 3.9: Normalized Drude weight D^*_N, the extrapolated value D^*_∞, and its relative error for 1D half–filled system with long–range Coulomb interactions.

a/a_0	D^*_{14}	D^*_{12}	D^*_{10}	D^*_8	D^*_6	D^*_∞	$\sigma(D^*_\infty)/D^*_\infty$
1.5	0.9225	0.9420	0.9563	0.9727	0.9822	0.8008	0.019
1.6	0.8879	0.9162	0.9378	0.9612	0.9754	0.7175	0.029
1.7	0.8419	0.8817	0.9130	0.9459	0.9667	0.6148	0.043
1.8	0.7826	0.8365	0.8805	0.9256	0.9552	0.4967	0.064
1.9	0.7095	0.7794	0.8389	0.8992	0.9406	0.3728	0.092
2.0	0.6245	0.7105	0.7875	0.8660	0.9222	0.2567	0.129
2.1	0.5315	0.6310	0.7265	0.8254	0.8996	0.1606	0.172
2.2	0.4338	0.5431	0.6549	0.7755	0.8714	0.0899	0.228
2.3	0.3403	0.4523	0.5766	0.7179	0.8379	0.0455	0.287
2.4	0.2554	0.3631	0.4937	0.6524	0.7982	0.0207	0.352
2.5	0.1839	0.2812	0.4109	0.5813	0.7526	0.0087	0.420
2.6	0.1269	0.2096	0.3315	0.5065	0.7009	0.0033	0.489
2.7	0.0840	0.1508	0.2595	0.4312	0.6441	0.0012	0.566
2.8	0.0536	0.1049	0.1972	0.3586	0.5836	0.0004	0.641
2.9	0.0315	0.0706	0.1456	0.2914	0.5208	0.0001	0.920
3.0	0.0196	0.0461	0.1047	0.2314	0.4575	0.0000	–

TABLE 3.10: Normalized Drude weight D^*_N, the extrapolated value D^*_∞, and its relative error for 1D half–filled system described by Hubbard model.

a/a_0	D^*_{14}	D^*_{12}	D^*_{10}	D^*_8	D^*_6	D^*_∞	$\sigma(D^*_\infty)/D^*_\infty$
1.5	0.6173	0.6742	0.7342	0.7973	0.8640	0.3294	0.070
1.6	0.5180	0.5879	0.6632	0.7437	0.8291	0.2106	0.106
1.7	0.4136	0.4935	0.5831	0.6817	0.7883	0.1178	0.155
1.8	0.3131	0.3973	0.4973	0.6127	0.7416	0.0573	0.215
1.9	0.2246	0.3063	0.4106	0.5390	0.6896	0.0244	0.286
2.0	0.1529	0.2259	0.3276	0.4631	0.6331	0.0092	0.364
2.1	0.0991	0.1598	0.2527	0.3884	0.5731	0.0032	0.449
2.2	0.0619	0.1094	0.1896	0.3190	0.5123	0.0010	0.540
2.3	0.0372	0.0724	0.1382	0.2561	0.4514	0.0003	0.639
2.4	0.0218	0.0467	0.0985	0.2018	0.3927	0.0001	0.739
2.5	0.0124	0.0294	0.0687	0.1561	0.3372	0.0000	–

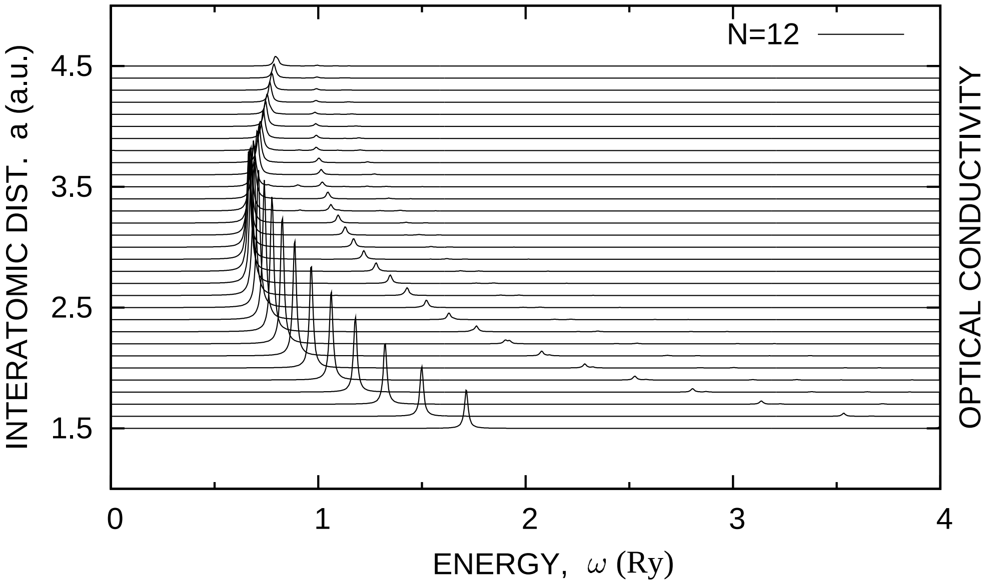

FIGURE 3.15: The regular part of the optical conductivity $\sigma_{\mathrm{reg}}(\omega)$ for *half–filled* 1D chain of $N = 12$ atoms. The long–range Coulomb interactions are included.

transforms to zero in the range $a/a_0 = 4 \div 5$. Also the regular part of conductivity $\sigma_{\mathrm{reg}}(\omega)$ (*cf.* Figure 3.16b) demonstrates the interband transitions in the metallic range, those vanish at $a \approx 4.5a_0$ (for $N = 16$). Such behavior provides the model case for transformation from a nanoscopic metal in the small a limit to the localized charge–ordered system (*cf.* Section 3.3.1) for larger a.

3.5 A brief overview

In this Chapter we have presented a fairly complete description of finite 1D chain in the framework of EDABI method, which combines the *exact* diagonalization of many–fermion Hamiltonian in the Fock space with a subsequent *ab–initio* readjustment of the single–particle (Wannier) function. The ground–state and dynamical properties have been obtained as a function of the lattice parameter a and the microscopic parameters have been determined explicitly. Our approach thus *extends* the current theoretical treatments to the *strongly correlated systems* within the parametrized (second–quantized) models by providing the determination of those parameters and, in turn, determining the fundamental properties of the correlated state explicitly as a function of a.

Technically, we determine at each step the microscopic parameters taking the Wannier functions composed of the Gaussian–type orbitals with an adjusted size,

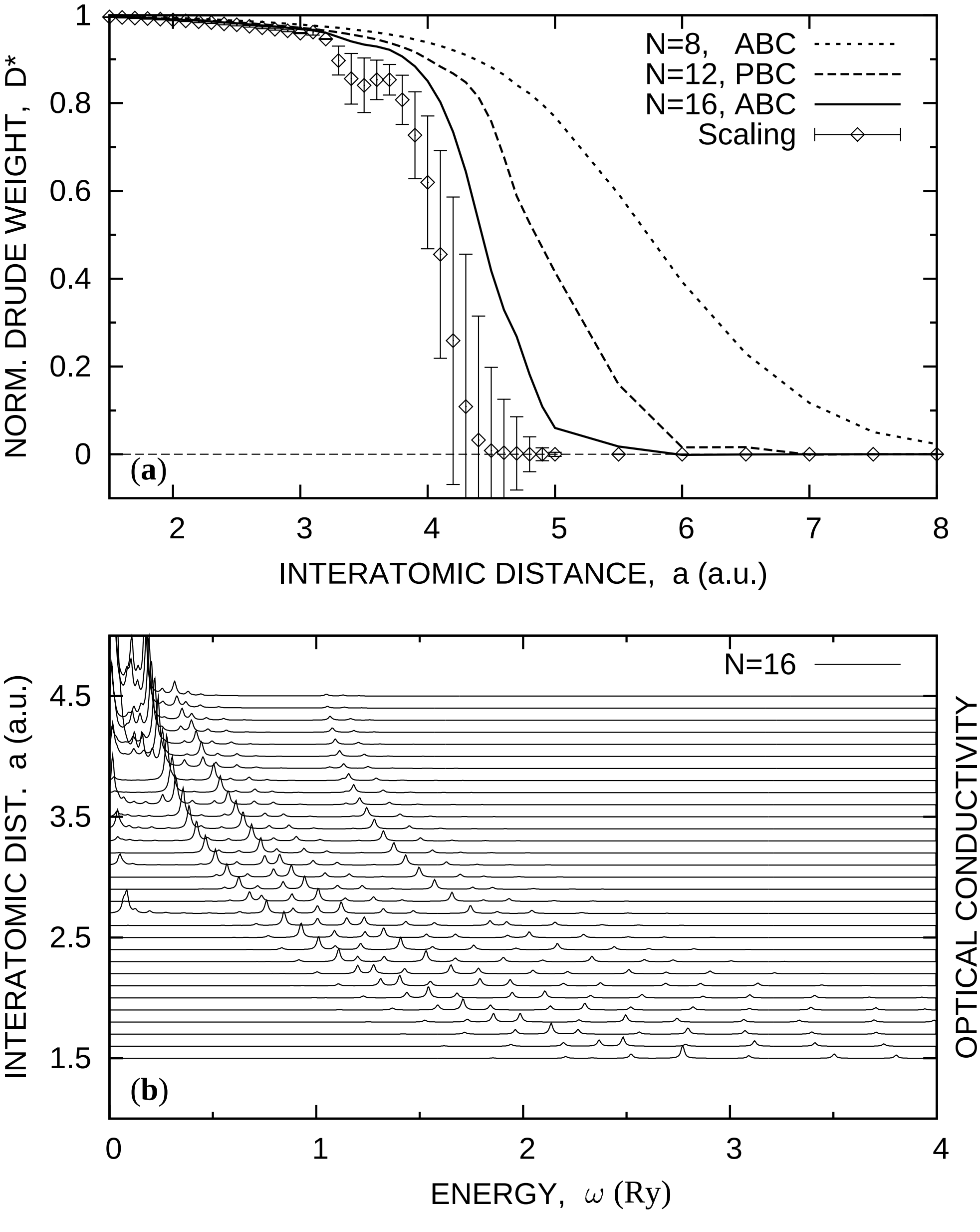

FIGURE 3.16: Optical conductivity for the *quarter–filled* chain with long–range Coulomb interaction: (a) normalized Drude weight vs. lattice parameter a (specified in a_0) and its values extrapolated with $1/N \to 0$ (the Aitken method has been used to estimate the extrapolation errors); (b) regular part of the conductivity, $\sigma_{\text{reg}}(\omega)$ for $N = 16$ atoms.

diagonalize the Hamiltonian in the Fock space within the Lanczos method, and thus obtained ground state energy is readjusted again by changing variationally the size of the orbitals, calculating the changed parameters and performing again the diagonalization in the Fock space, and so on, until the global minimum is reached for given a. To speed up the procedure, we organize the study in two steps. *First,* we determine the optimal inverse orbital size α_{min} as a function of a for relatively small systems of $N = 6 \div 10$ atoms. *Second,* as the convergence of α_{min} for $N \geqslant 8$ is remarkable, we use the extrapolated values for $N > 10$, up to the largest studied system of $N = 16$ atoms. Such convergence is strongly dependent on a proper application of the *tight–binding approximation* for the system with long–range Coulomb interactions, as the charge screening in 1d is less effective. Only by including properly the long–range attractive interaction to the ions and the repulsive interactions between the electrons and ions, we reach a valid atomic limit at large distance a. We discuss this problem in detail in Section 3.1. Also the relation to our previous approach employing the Slater–type orbitals is provided in Section 3.2.

In the major part of this Chapter, we analyze the situation with one electron per atom (the *half–filled* band case), including the *long–range* Coulomb interactions. Physical properties of such nanoscopic system containing $N = 6 \div 14$ atoms are compared with those obtained when only the on–site (Hubbard U) term is included (supposing the same values of the model parameters in both situations). Basic ground–state correlation functions and the Luttinger–liquid type of the electron momentum distribution (*cf.* Section 3.3) suggest the *crossover transition* from the metallic to the insulating (spin–ordered) state with the increasing a in both cases of the system with– and without the long–range interactions (but metallic behavior is manifested to much stronger degree when the long–range part of the Coulomb interactions is included). However, the finite–size scaling with $1/N \rightarrow 0$, performed on the charge–energy gap shows the insulating nature of the ground state for the large N limit, in agreement with the renormalization–group results for the *infinite* system with two Fermi points (Fabrizio, 1996). Such an apparently contradictory nature of the nanoscopic systems is confirmed by an analysis of their spectral and transport properties (*cf.* Section 3.4). On one hand, the quasiparticles are well–defined in the spectral function, but the incoherent part is always present and it strength grows systematically with the increasing a (the energy gap is also present in the density of states for any a). Analogously, the Drude weight is nonzero in the small a limit (and critical values of a agree with those obtained form the Luttinger–liquid exponent in both cases with and without the long–range interactions), but the regular part of the optical conductivity exhibits the insulating behavior.

An illustrative example of the nanonscopic system with a clear transformation from the nanometal to the nanoinsulator with charge–density wave order is provided for a similar system in the *quater–filled* band case (and when including the long–range Coulomb interactions). For that system, the Drude weight changes gradually from its maximal value to zero, and the other studied properties evolve appropriately with the increasing lattice parameter a. The intermediate range of a, where the evolution takes place, also shrink rapidly with increasing N, suggesting the zero–temperature transition in the large N limit. To the best of our knowledge, such a transition has not been identified before for 1D system of $S = 1/2$ electrons.

The above analysis, for both the half– and the quarter–filled band cases is very sensitive to the choice of the boundary conditions for a finite system. This problem is widely studied in existing literature (Jullien and Martin, 1982; Rościszewski and Oleś, 1993), we reviewed it in Section 3.3 and have provided its relation to the fictitious–flux approach by Kohn (1964), as well as have used it to define the electric conductivity in a standard manner (*cf.* Section 3.4).

In the next Chapter we apply the EDABI method to the analysis of a simple (3D) H_4 cluster and in Chapter 5 we discuss a novel type of quantum ladders with the completely frustrated spins. The ladder is the first step in approaching the molecular hydrogen cristal.

Chapter 4

Basic 3D system: H_4 cluster

In this Chapter we analyze the stability of 3D clusters containing two H_2 molecules within the EDABI method (*cf.* Section 2.1). We focus here on two different geometries of the cluster, with (i) parallel and (ii) perpendicular orientation of the molecular axes, as depicted schematically in Figure 4.1, where the geometrical parameters a and b are also defined. Such an analysis constitutes a starting point for the complete study of ground–state and dynamical properties of the fermionic ladders, presented in the *next* Chapter. The instability of the molecules for short distance between them seems also meaningful for the hydrogen metallicity at high pressure. The latter aspect is discussed in the end part of this Chapter.

4.1 Model Hamiltonian

Here we restrict ourselves, as in the *previous* Chapter, to considering the *extended Hubbard model* with long–range part of the Coulomb interaction. Namely, the

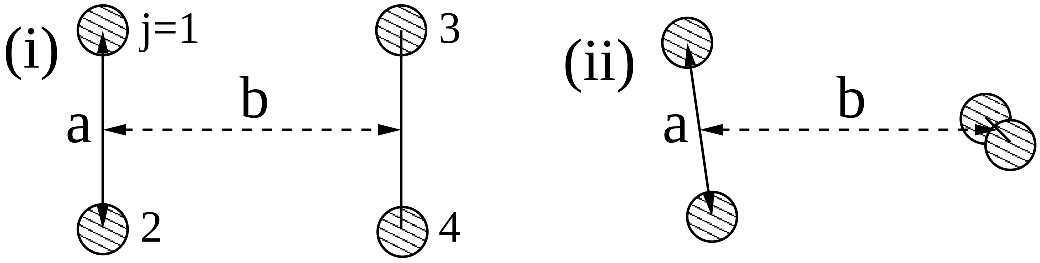

FIGURE 4.1: Schematic representation of the H_4 cluster geometries: (i) parallel and (ii) perpendicular orientation of H_2 molecules. Geometrical parameters of the cluster are: the bond length a and the intermolecular distance b. The numbering order of the lattice sites j is also provided.

system Hamiltonian reads

$$H = \epsilon_a^{\text{eff}} \sum_i n_i + \sum_{ij\sigma} t_{ij} a_{i\sigma}^{\dagger} a_{j\sigma} + U \sum_i n_{i\uparrow} n_{i\downarrow} + \sum_{i<j} K_{ij} \delta n_i \delta n_j, \tag{4.1}$$

where the effective atomic energy is defined in the standard manner (3.7), the indexes assume the values $i, j = 1 \ldots 4$, and the numbering order is fixed as in Figure 4.1. The novel elements in the Hamiltonian (4.1) are the second– and the third–neighbor hopping terms, $t_{13} = t_{24} \equiv t_2$ and $t_{14} = t_{23} \equiv t_3$, respectively. They cannot be neglected as in the Hamiltonian (3.8), since for the particular values of the geometrical parameters a and b one can, in principle, get $t_1 \approx t_2 \approx t_3$.

The analysis is performed again with the Gaussian STO–3G basis (*cf.* Appendix A), and the inverse orbital size α is optimized with respect to the system ground–state energy E_G, as usually in the framework of the EDABI method. The Lanczos method for the diagonalization of the Hamiltonian in the Fock space (*cf.* Section 2.2) is now replaced by standard numerical routines (Press et al., 1992), since the corresponding matrix size is $N_{\text{st}} = 36$ for the half–filled band sector ($N_e = N = 4$) and the total z–component of spin is $S^z_{\text{tot}} = 0$.

4.1.1 The Wannier basis

The microscopic parameters in the Hamiltonian (4.1) are defined for the Wannier basis, which is constructed in two steps. *First,* we define the orthogonalized molecular Wannier–like functions

$$w_1^a = \beta^a \left(\Psi_1 - \gamma^a \Psi_2 \right), \qquad w_2^a = \beta^a \left(\Psi_2 - \gamma^a \Psi_1 \right) \tag{4.2}$$

(and analogously for the sites $i = 3$ and 4), where the coefficients

$$\beta_a = \frac{1}{\sqrt{2}} \left(\frac{1 + \sqrt{1 - S_1^2}}{1 - S_1^2} \right)^2, \qquad \gamma_a = \frac{S_1}{1 + \sqrt{1 - S_1^2}}. \tag{4.3}$$

The overlap integrals of the atomic functions Ψ_i are, due to the system symmetry, given by

$$S_0 \equiv \langle \Psi_i | \Psi_i \rangle = 1, \qquad S_1 \equiv \langle \Psi_1 | \Psi_2 \rangle = \langle \Psi_3 | \Psi_4 \rangle,$$
$$S_2 \equiv \langle \Psi_1 | \Psi_3 \rangle = \langle \Psi_2 | \Psi_4 \rangle, \qquad S_3 \equiv \langle \Psi_1 | \Psi_4 \rangle = \langle \Psi_2 | \Psi_3 \rangle. \tag{4.4}$$

Molecular orbitals, corresponding to the functions (4.2)

$$\Phi_{12}^0 = \frac{1}{\sqrt{2}} \left(w_1^a + w_2^a \right) = \frac{1}{\sqrt{2}} \beta^a \left(1 - \gamma^a \right) \left(\Psi_1 + \Psi_2 \right), \tag{4.5}$$

$$\Phi_{12}^{\pi} = \frac{1}{\sqrt{2}} \left(w_1^a - w_2^a\right) = \frac{1}{\sqrt{2}} \beta^a \left(1 + \gamma^a\right) \left(\Psi_1 - \Psi_2\right), \qquad (4.6)$$

(and analogously for the sites $i = 3$ and 4), have nonzero intermolecular overlaps

$$\left\langle \Phi_{12}^0 | \Phi_{34}^0 \right\rangle = \langle w_1 | w_3 \rangle + \langle w_1 | w_4 \rangle = (\beta^a)^2 \left(1 - \gamma^a\right)^2 (S_2 + S_3), \qquad (4.7)$$

$$\left\langle \Phi_{12}^{\pi} | \Phi_{34}^{\pi} \right\rangle = \langle w_1 | w_3 \rangle - \langle w_1 | w_4 \rangle = (\beta^a)^2 \left(1 + \gamma^a\right)^2 (S_2 - S_3), \qquad (4.8)$$

whereas $\langle \Phi_{12}^0 | \Phi_{34}^{\pi} \rangle = \langle \Phi_{12}^{\pi} | \Phi_{34}^0 \rangle = 0$. Since that, in the *second* step, we define the orthogonal Bloch functions for the cluster

$$\widetilde{\Phi}_{12}^0 = \beta^0 \left(\Phi_{12}^0 - \gamma^0 \Phi_{34}^0\right), \qquad \widetilde{\Phi}_{34}^0 = \beta^0 \left(\Phi_{34}^0 - \gamma^0 \Phi_{12}^0\right), \qquad (4.9)$$

$$\widetilde{\Phi}_{12}^{\pi} = \beta^{\pi} \left(\Phi_{12}^{\pi} - \gamma^{\pi} \Phi_{34}^{\pi}\right), \qquad \widetilde{\Phi}_{34}^{\pi} = \beta^{\pi} \left(\Phi_{34}^{\pi} - \gamma^{\pi} \Phi_{12}^{\pi}\right), \qquad (4.10)$$

where the coefficients $\beta^{0,\pi}$ and $\gamma^{0,\pi}$ have the form as in Eq. (4.3) with overlap S_1 replaced by $\langle \Phi_{12}^0 | \Phi_{34}^0 \rangle$ and $\langle \Phi_{12}^{\pi} | \Phi_{34}^{\pi} \rangle$, given by Eqs. (4.7) and (4.8), respectively. Thus, the orthogonal Wannier functions for the cluster are given by the transformation of the form inverse to that in Eqs. (4.5) and (4.6), namely

$$w_1 = \frac{1}{\sqrt{2}} \left(\widetilde{\Phi}_{12}^0 + \widetilde{\Phi}_{12}^{\pi}\right), \qquad w_2 = \frac{1}{\sqrt{2}} \left(\widetilde{\Phi}_{12}^0 - \widetilde{\Phi}_{12}^{\pi}\right), \qquad (4.11)$$

and analogously for the sites $i = 3$ and 4.

The subsequent substitutions of Eqs. (4.5-4.6) to (4.9-4.10), and then to Eqs. (4.11), with appropriate definitions of the coefficients β^a, γ^a, $\beta^{0,\pi}$, and $\gamma^{0,\pi}$, may leads one to an expansion for the Wannier functions in the form

$$w_1 = \mathrm{B}_0 \Psi_1 + \mathrm{B}_1 \Psi_2 + \mathrm{B}_2 \Psi_3 + \mathrm{B}_3 \Psi_4, \qquad (4.12)$$

with explicitly defined coefficients $\mathrm{B}_0 \dots \mathrm{B}_3$. Such definitions are, however, quite long and useless, since in practice we perform the substitutions mentioned above numerically, for given geometrical parameters a and b, and the inverse orbital size α. The described construction is well defined for any values of the parameters, as the values under the square roots in Eq. (4.3), as well as in analogical expressions for $\beta^{0,\pi}$ and $\gamma^{0,\pi}$, are always positive.

4.1.2 Microscopic parameters

Numerical values of the effective atomic energy ϵ_a^{eff}, hopping integrals $t_1 \dots t_3$, the intra– and intersite Coulomb repulsions U and $K_1 \dots K_3$, are gathered in Table 4.1 for the cluster geometry (i) and in Table 4.1 for (ii). All the data were obtained for the Gaussian STO–3G basis and corresponds to the optimal values of the inverse

TABLE 4.1: Microscopic parameters (in Ry) for the H_4 cluster configuration (i) calculated in the Gaussian STO–3G basis. Corresponding values of the inverse orbital size $\alpha_{\min}$ and the bond length $a_{\min}$ are provided in Table 4.3.

b/a_0	$\epsilon_a^{\mathrm{eff}}$	t_1	t_2	t_3	U	K_1	K_2	K_3
1.7	-0.2354	-0.8610	-0.6622	0.0822	1.811	1.027	0.947	0.728
2.0	-0.3088	-0.8791	-0.5137	0.0617	1.802	1.032	0.872	0.692
2.5	-0.4233	-0.8390	-0.3268	0.0352	1.748	1.007	0.750	0.619
3.0	-0.4925	-0.7983	-0.2067	0.0220	1.702	0.984	0.649	0.553
3.5	-0.5319	-0.7685	-0.1290	0.0150	1.671	0.967	0.567	0.497
4.0	-0.5533	-0.7492	-0.0785	0.0103	1.653	0.957	0.500	0.449
5.0	-0.5689	-0.7316	-0.0267	0.0037	1.639	0.949	0.401	0.373
6.0	-0.5707	-0.7275	-0.0084	0.0007	1.638	0.948	0.334	0.318
8.0	-0.5692	-0.7269	-0.0006	-0.0000	1.640	0.949	0.250	0.243
10.0	-0.5684	-0.7268	-0.0000	-0.0000	1.641	0.950	0.200	0.197
20.0	-0.5673	-0.7272	-0.0000	-0.0000	1.642	0.951	0.100	0.100
∞	-0.5671	-0.7273	0	0	1.642	0.951	0	0

TABLE 4.2: Microscopic parameters (in Ry) for the H_4 cluster configuration (ii) calculated in the Gaussian STO–3G basis. Corresponding values of the inverse orbital size $\alpha_{\min}$ and the bond length $a_{\min}$ are provided in Table 4.4.

b/a_0	$\epsilon_a^{\mathrm{eff}}$	t_1	t_2	t_3	U	K_1	K_2	K_3
1.6	-0.5352	-0.5423	-0.2986	-0.2986	1.650	0.911	0.816	0.816
2.0	-0.4511	-0.7496	-0.2230	-0.2230	1.732	0.991	0.772	0.772
2.5	-0.4863	-0.7820	-0.1451	-0.1451	1.711	0.986	0.680	0.680
3.0	-0.5221	-0.7721	-0.0923	-0.0923	1.683	0.972	0.598	0.598
3.5	-0.5467	-0.7558	-0.0571	-0.0571	1.661	0.961	0.530	0.530
4.0	-0.5613	-0.7423	-0.0342	-0.0342	1.646	0.953	0.473	0.473
5.0	-0.5715	-0.7293	-0.0115	-0.0115	1.637	0.947	0.387	0.387
6.0	-0.5719	-0.7264	-0.0038	-0.0038	1.636	0.947	0.326	0.326
8.0	-0.5692	-0.7269	-0.0003	-0.0003	1.640	0.949	0.247	0.247
10.0	-0.5685	-0.7268	-0.0000	-0.0000	1.641	0.950	0.198	0.198
20.0	-0.5673	-0.7272	-0.0000	-0.0000	1.642	0.951	0.100	0.100
∞	-0.5671	-0.7273	0	0	1.642	0.951	0	0

orbital size α_{min} and the bond length a_{min} provided in the *next* Section. We also choose the local minimum $a < b$, where it is not the global one (*cf.* next Section). The limiting values for the intermolecular distance $b \to \infty$ corresponds to the exact solution of the hydrogen molecule treated as a two–side problem (Spałek, Oleś and Chao, 1981; de Boer and Schadschneider, 1995), for which the ground–state energy is given by

$$\begin{aligned} E_G(H_2) &= 2\epsilon_a + \frac{U+K_1}{2} - \sqrt{(U-K_1)^2/4 + 4t_1^2} + \frac{2}{R_{12}} \\ &= 2\epsilon_a^{\text{eff}} + \frac{U-K_1}{2} - \sqrt{(U-K_1)^2/4 + 4t_1^2}, \end{aligned} \tag{4.13}$$

where $\epsilon_a^{\text{eff}} \equiv \epsilon_a + (K_1 + 2/R_{12})/2$ (in Ry) and the remaining parameters are analogical to those in the cluster Hamiltonian (4.1), providing the Wannier basis reduce to the form of Eq. (4.2) in limit $b \to \infty$.

4.2 The optimized ground–state energy

The Hamiltonian (4.1) is now diagonalized in the Fock space using standard numerical routines (Press et al., 1992) and the resulting ground–state energy E_G is optimized with respect to the inverse orbital size α in the Gaussian STO–3G basis (*cf.* Appendix A). In this manner, one can consider E_G as a function of two parameters: the bond length a and the intermolecular distance b (*cf.* Figure 4.1).

We analyze first the dependence $E_G(a)$ for a given b and the optimal inverse orbital size $\alpha = \alpha_{\text{min}}(a)$, which is presented in Figure 4.2 for the cluster geometry (i) and in Figure 4.3 for (ii). In the case of parallel molecular axis (i), the local minimum of $E_G(a)$ appears for $b < 1.65a_0$ at the point $a_{\text{min}} < b$ (*cf.* Figure 4.2a). For the critical value of $b_{\text{crit}}^{(i)} = 2.39a_0$ the minimum for $a_{\text{min}} < b$ is equivalent to that for $a_{\text{min}} > b$, and become the global one for the values of the intermolecular distance $b > b_{\text{crit}}$. The situation is very similar in the case of cluster geometry (ii), corresponding to perpendicular orientation of the molecular axes (*cf.* Figure 4.3a). The critical value of b is now $b_{\text{crit}}^{(ii)} = 1.88a_0$, the local minimum of $E_G(a)$ at $a_{\text{min}} < b$ disappear for $b = 1.59a_0$. Significant differences for the cluster geometries (i) and (ii) are present, however, in the inverse orbital size $\alpha_{\text{min}}(a)$, which is almost independent on a in the case (ii) (*cf.* Figure 4.3b) in comparison to the case (i) (*cf.* Figure 4.2b). The appearance of such differance shows that the closed–shell molecular orbital configuration (*note* the data for free molecules in the limit $b \to \infty$ are drawn in Figures 4.2 and 4.3 as the *dashed* lines) is strongly preffered in the case (ii), whereas electron correlations play a crucial role for the planar cluster geometry (i).

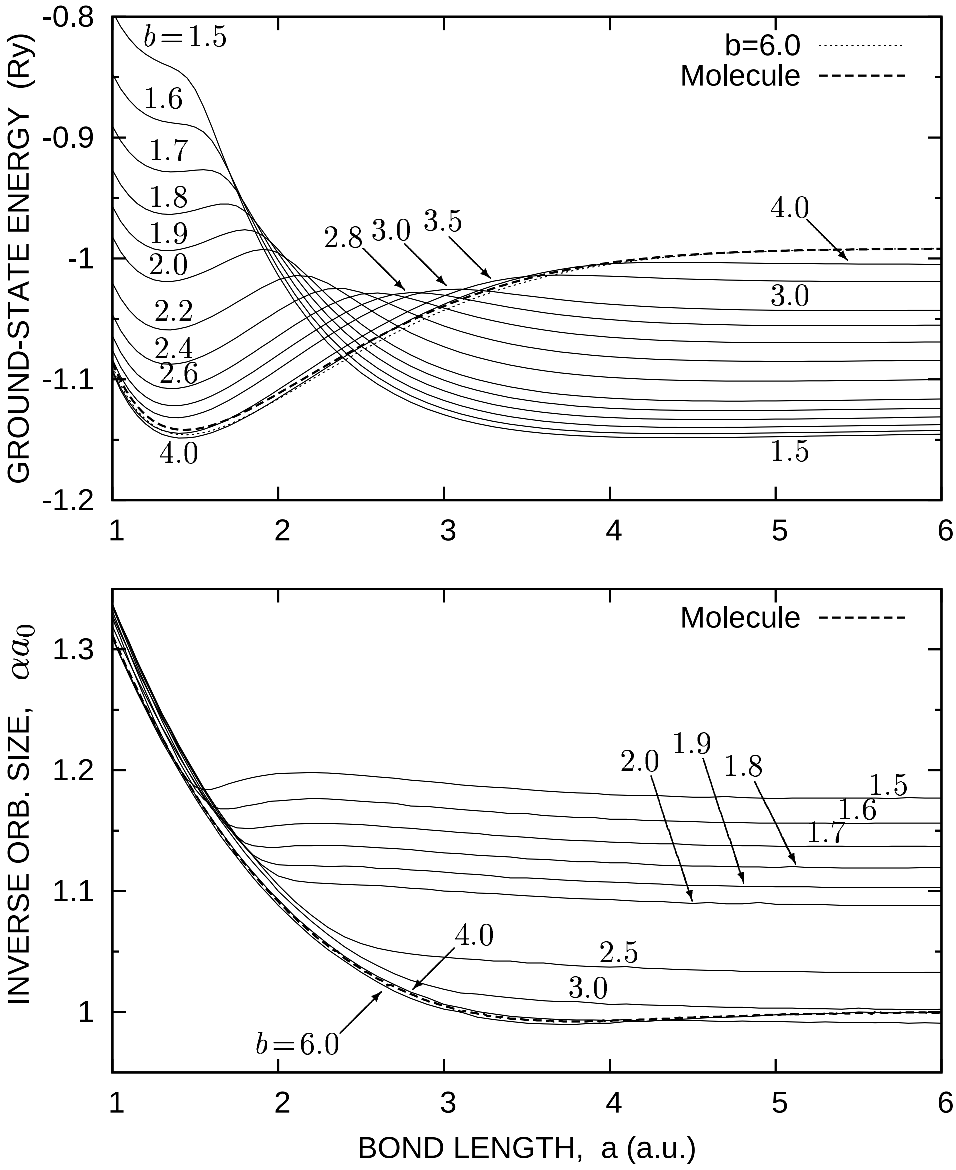

FIGURE 4.2: The optimized ground–state energy per atom (a) and the optimized inverse orbital size (b) for the planar H_4 cluster (i). The *dashed* lines represent the results for H_2 molecule. The values of the bond length a and the intermolecular distance b are specified in the units of a_0.

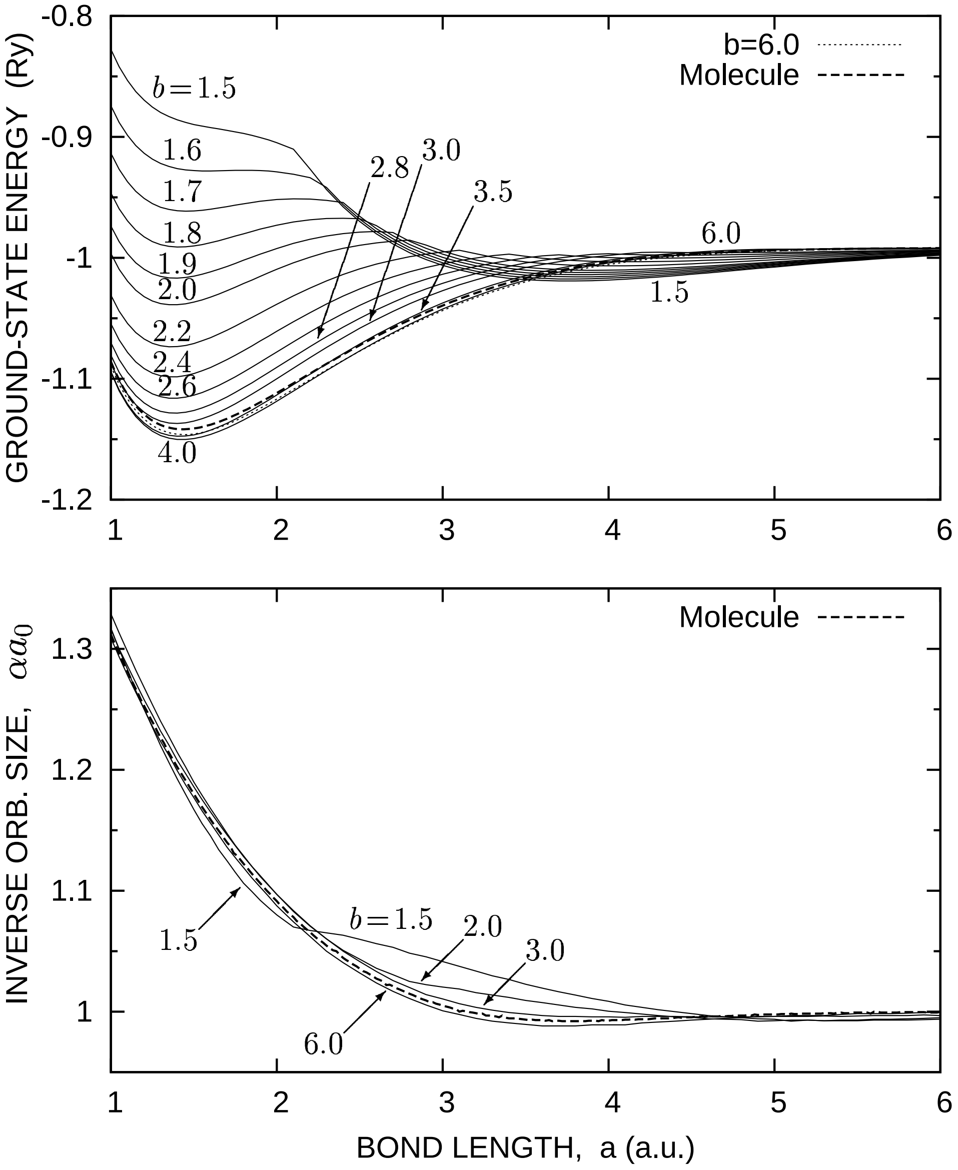

FIGURE 4.3: The optimized ground–state energy per atom (a) and the optimized inverse orbital size (b) for the cluster geometry (ii). The characteristics for H_2 molecule (the *dashed* lines) are recovered in the large–b limit. The values of the bond length a and the intermolecular distance b are specified in a_0.

TABLE 4.3: The optimal bond length a_{min}, inverse orbital size α_{min}, and the ground–state energy E_G per atom for the planar H_4 cluster (i). The corresponding energy of the molecular dimer $E_G(2\mathrm{H}_2)$ is also provided.

b/a_0	a_{min}/a_0	$\alpha_{\mathrm{min}}a_0$	E_G/N	$E_G(2\mathrm{H}_2)/N$
1.7	1.3627	1.2231	-0.928424	-0.922411
2.0	1.3291	1.2395	-1.019152	-1.016365
2.5	1.3518	1.2304	-1.098551	-1.097314
3.0	1.3829	1.2157	-1.131770	-1.131167
3.5	1.4075	1.2041	-1.144613	-1.144317
4.0	1.4238	1.1969	-1.148598	-1.148454
5.0	1.4373	1.1911	-1.148093	-1.148056
6.0	1.4390	1.1908	-1.145975	-1.145964
8.0	1.4375	1.1924	-1.143651	-1.143649
10.0	1.4366	1.1929	-1.142756	-1.142755
20.0	1.4357	1.1940	-1.141908	-1.141908
∞	1.4356	1.1943	-1.141783	

TABLE 4.4: The optimal bond length a_{min}, inverse orbital size α_{min}, and the ground–state energy E_G per atom for the cluster geometry (ii). The corresponding energy of the molecular dimer $E_G(2\mathrm{H}_2)$ is also provided.

b/a_0	a_{min}/a_0	$\alpha_{\mathrm{min}}a_0$	E_G/N	$E_G(2\mathrm{H}_2)/N$
1.6	1.5796	1.1568	-0.928235	-0.923390
2.0	1.3759	1.2206	-1.038891	-1.037968
2.5	1.3725	1.2193	-1.108116	-1.107803
3.0	1.3947	1.2091	-1.136931	-1.136809
3.5	1.4153	1.2000	-1.147566	-1.147519
4.0	1.4292	1.1937	-1.150310	-1.150293
5.0	1.4397	1.1894	-1.148674	-1.148672
6.0	1.4400	1.1897	-1.146200	-1.146200
8.0	1.4377	1.1926	-1.143705	-1.143705
10.0	1.4367	1.1929	-1.142774	-1.142774
20.0	1.4357	1.1940	-1.141908	-1.141908
∞	1.4356	1.1943	-1.141783	

The above observation is further confirmed by the data gathered in Tables 4.3 and 4.4, where we compared the ground–state energy E_G, obtained within the EDABI method (and corresponding to the local minimum $a_{\rm min} < b$) with that of the molecular dimer configuration $E_G(2\mathrm{H}_2)$. The latter values were calculated with the help of an exact expression (4.13), in with we substitute the microscopic parameters by their values for the H_4 cluster (*cf.* Tables 4.1 and 4.2). Such approach corresponds to the variational wavefunction for the cluster in the form $|\Psi(\mathrm{H}_4)\rangle \approx |\Psi(\mathrm{H}_2)\rangle\,|\Psi(\mathrm{H}_2)\rangle$, since the K_2 and K_3 terms do not play the role due to zero dipole momentum of the molecules. As we expect, the variational approach leads to the values of $E_G(2\mathrm{H}_2)$ closer to the exact E_G in the case (ii) than for the planar cluster (i), *cf.* Table 4.4 and 4.3, respectively.

4.2.1 Absolute stability

Figures 4.2 and 4.3 exhibit also another feature of the H_4 cluster: the global energy minimum in the parameter (a, b) space. The existence of such minimum around $b \approx 4a_0$ is clear, since the curve $E_G(a)$ for $b = 6a_0$ lay below those for $b = 3.5a_0$ and $6a_0$, and the limiting curve for $b \to \infty$ (H_2 molecule) is above each of them (*cf.* Figures 4.2a and 4.3a, the situation is very similar for both cluster configurations). The precise positions of the global E_G minima are the following:

$$b^{(i)}_{\rm min} = 4.32a_0, \qquad a^{(i)}_{\rm min} = 1.4303a_0, \qquad \alpha^{(i)}_{\rm min} = 1.1937a_0^{-1},$$

$$E_G^{\mathrm{min}(i)}/N = -1.149061\ \mathrm{Ry} \tag{4.14}$$

for the planar cluster geometry (i), and

$$b^{(ii)}_{\rm min} = 4.13a_0, \qquad a^{(ii)}_{\rm min} = 1.4318a_0, \qquad \alpha^{(ii)}_{\rm min} = 1.1927a_0^{-1},$$

$$E_G^{\mathrm{min}(ii)}/N = -1.150396\ \mathrm{Ry} \tag{4.15}$$

for the geometry (ii). The corresponding minimum for free H_2 molecule (the $b \to \infty$ limit) is provided e.g. in the last row of Table 4.3. The binding energies for molecules in (i) and (ii) clusters are, respectively: $\Delta E_G^{(i)}/N = 7.3 \cdot 10^{-3}$ Ry and $\Delta E_G^{(ii)}/N = 8.6 \cdot 10^{-3}$ Ry.

The shape of the ground–state energy surface $E_G(a, b)$ is illustrated in Figures 4.4 and 4.5 for both considered cluster geometries. The contour plots in the parameter plane (*cf.* Figure 4.4a and 4.5a) shows the energy minima on the both sides of the symmetry axis $a = b$, corresponding to the square configuration of the planar (i) cluster, and $a = \sqrt{2}b$ for the tetrahedral configuration in the case (ii), as depicted in Figures 4.4b and 4.5b, respectively. The evolution of the $E_G(a)$ minima with b, and the catastrophe for $b = b_{\rm crit}$, discussed in the *previous* Section,

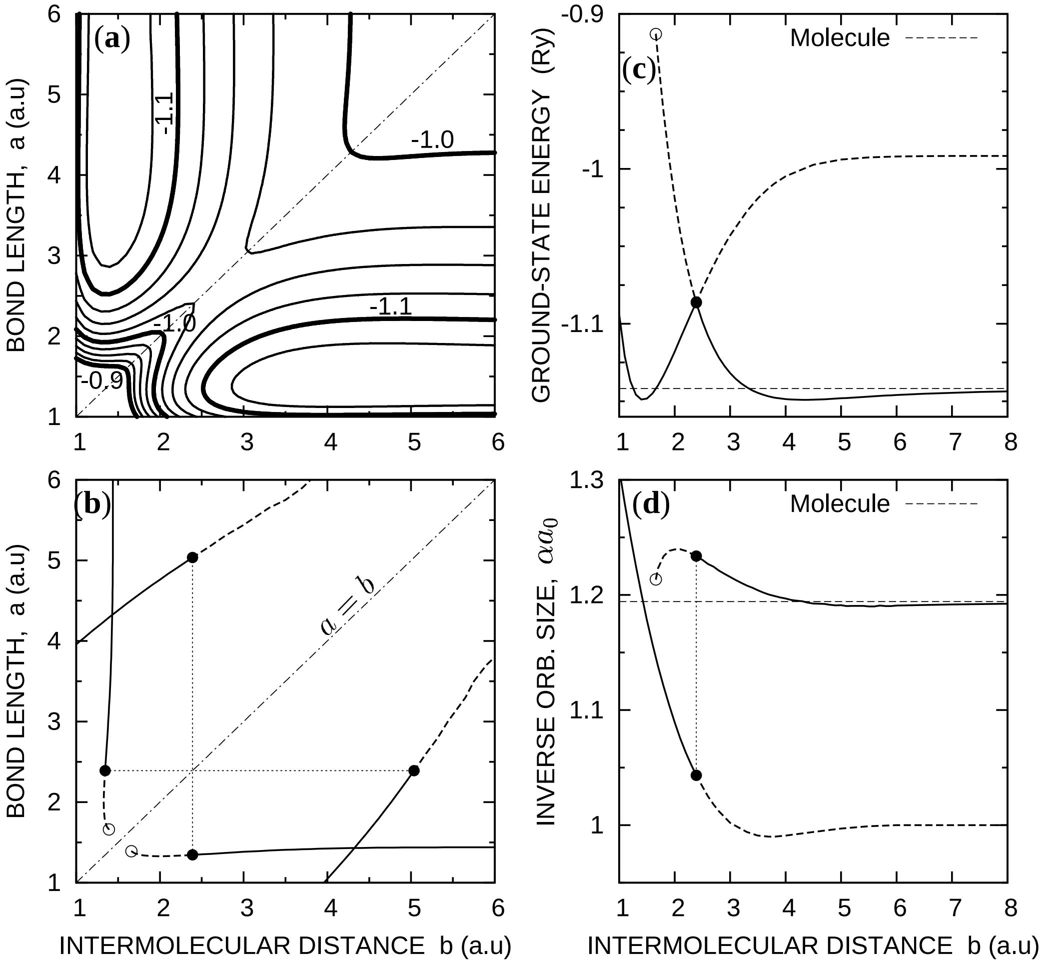

FIGURE 4.4: The ground–state energy surface $E_G(a, b)$ for the planar cluster geometry (i): (a) contour plot in the parameter plane, (b) representation of global (*solid* lines) and local (*dashed* lines) conditional minima in respect to a for a given b and vice–versa, (c) ground–state energy E_G vs. b for global and local conditional minima, and (d) the corresponding optimized inverse orbital size $\alpha_{\min}$. *Full circles* marks the equivalent (global) energy minima, *open* – the points where the local minima vanish. The symmetry axis (*dashed–dot* line) on the parameter plane and the results for H_2 molecule (*thin dashed* line) are also shown.

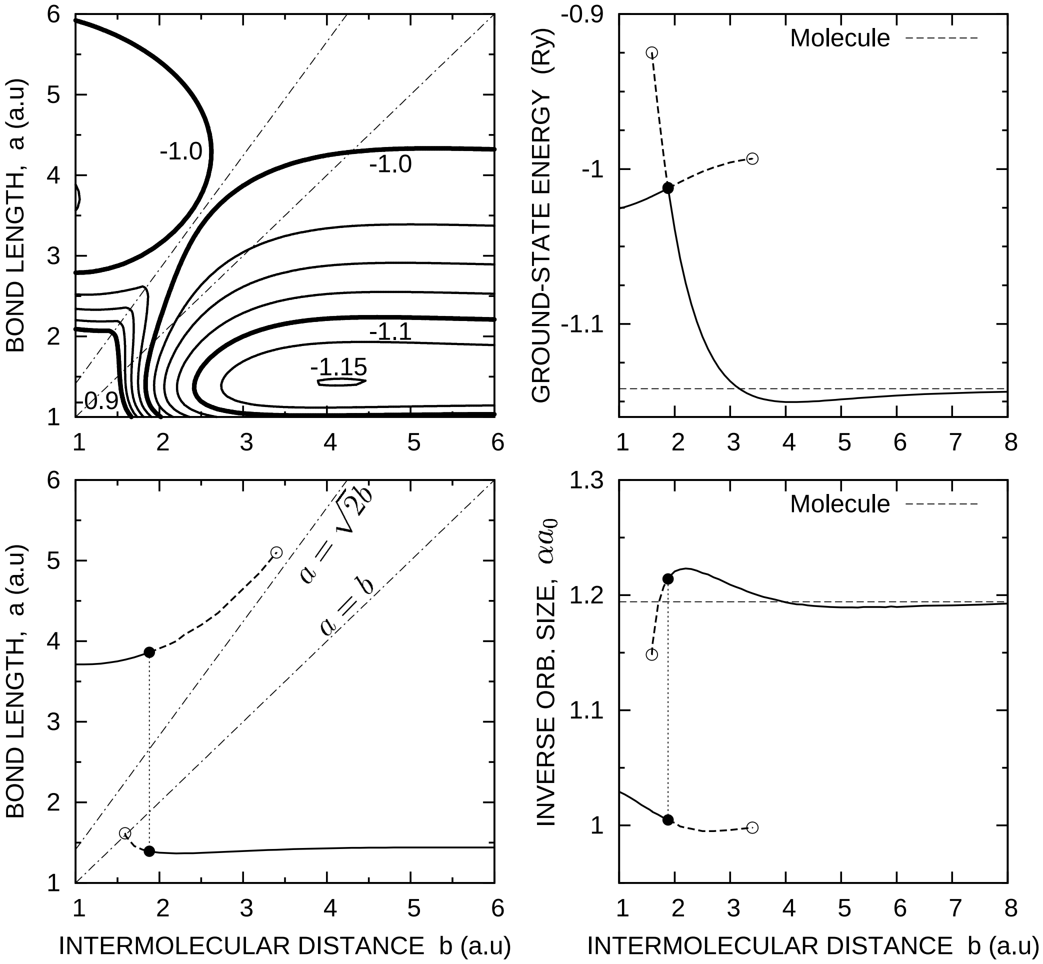

FIGURE 4.5: The ground–state energy surface $E_G(a,b)$ for the cluster geometry (ii): (a) contour plot in the parameter plane, (b) representation of global (*solid* lines) and local (*dashed* lines) conditional minima in respect to a for a given b, (c) ground–state energy E_G vs. b for global and local conditional minima, and (d) the corresponding optimized inverse orbital size α_{min}. The tetrahedral configuration ($a=\sqrt{2}b$) is marked on the parameter plane with the *dot–dashed* line. The remaining symbols are the same as in Figure 4.4.

can be now explained in terms of the conditional energy minima with respect to a, for a given b (*cf.* Figure 4.4c and 4.5c). The optimal ground–state energy is continuous in the point $b = b_{\mathrm{crit}}$, whereas its derivative, as well as both optimized parameters a and α (*cf.* Figure 4.4d and 4.5d) show discontinuity. Such behavior suggests the presence of the first–order phase transition in the thermodynamic limit.

4.2.2 Configurations of the high symmetry

As one can read form the contour plots in Figures 4.4a and 4.5a, the conditional minimization of the ground–state energy for the square ($a = b$) configuration of the planar (i) cluster, and the tetrahedral ($a = \sqrt{2}b$) for the case (ii), leads to the saddle points at (a, b) plane in both cases. In other words, the ground–state energies of the above high–symmetry configurations are higher than the values for the global minima (4.14) and (4.15). They are also significantly higher than the energy of free H_2 molecule, namely, we get:

- $b_{\mathrm{min}} = 2.6810a_0$, $\alpha_{\mathrm{min}} = 1.0406a_0$, $E_G^{\mathrm{min}} = -1.028790$ Ry,
  for the square $a\!=\!b$, (i); and

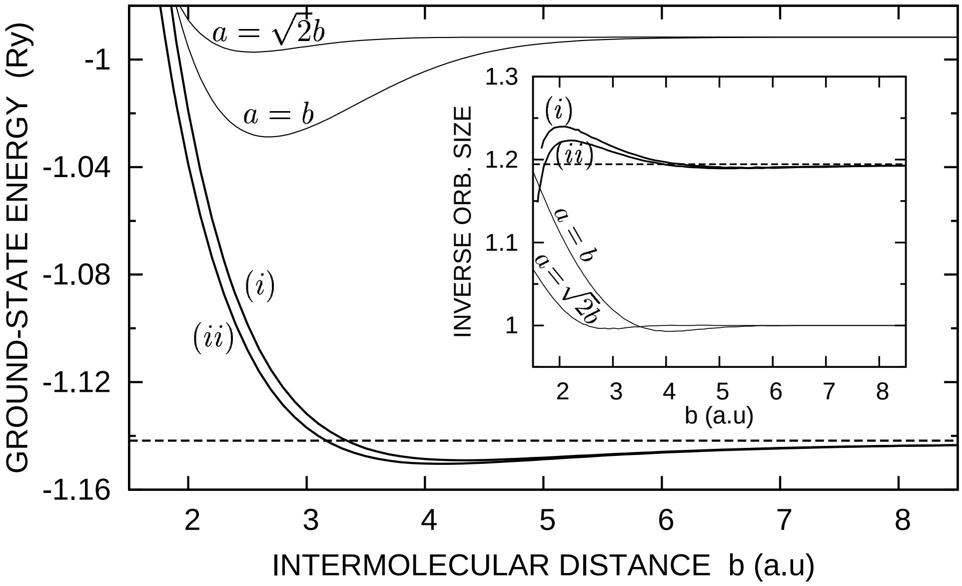

FIGURE 4.6: Ground–state energies of the high–symmetry configuration (the *square* and the *tetrahedron*) compared with those corresponding to the optimal bond length a_{min} for the H_4 planar cluster (i) and the spacial configuration (ii). *Inset* provides optimal values of the inverse orbital size α_{min}.

- $b_{\rm min} = 2.5447 a_0$, $\alpha_{\rm min} = 0.9994 a_0$, $E_G^{\rm min} = -0.997250$ Ry, for the tetrahedron $a = \sqrt{2} b$, (ii).

The situation is illustrated in a function of the intermolecular distance b in Figure 4.6, where also the corresponding values of the optimal inverse orbital size $\alpha_{\rm min}$ are shown with the *inset*.

The above results are another way of showing that the molecules in free H_4 cluster preserve their identity, since the optimal bond length $a_{\rm min}$ in Eqs. (4.14) and (4.15) is about three times smaller than the corresponding intermolecular distance $b_{\rm min}$. The system could be driven by external forces to the high–symmetry configurations, in which the identity of the molecules is lost. However, such a transformation requires a relatively high energy. The situation is qualitatively similar in the case of 3D hydrogen crystal, where the dissociation of the molecules into atoms and the resulting metal–insulator transition (MIT) appears at ultra–high pressure (Hemley and Ashcroft, 1998; Nellis, 2000). The last aspect of electronic states is discussed in the *next* Section.

4.3 Physical discussion

The solid hydrogen is predicted (Wigner and Huntington, 1935; Ceperley and Alder, 1986) to become metallic at megabare pressures. Experimental evidence for such a pressure–induced MIT were found first in the 250 GPa range at 77 K by Mao and Hemley (1989), and than at 150 GPa for the room temperature 295 K (Hemley and Mao, 1989; Hemley and Mao, 1990). Although the results for H_4 cluster presented in this Chapter seem, in principle, to be unrelated to the situation in 3D crystallite hydrogen with the *hcp* structure, some interesting common features with *ab initio* calculations have been observed.

It was reported by Chacham and Louie (1991) that the influence of an orientational order is crucial for the metalization pressure. The fully ordered phase undergoes a metalization due to band overlap at the volume $V = 2.50$ cm^3/mol, whereas the disordered phase at $V = 1.89$ cm^3/mol, which correspond to the critical pressures of 151 and 300 GPa, respectively. Our model system, the H_4 cluster, shows qualitatively a very similar behavior, since the planar geometry (i) could be regarded as a fully ordered phase (*parallel* molecular axes) and the disordered phase contains a significant fraction of the geometry (ii). The quantitative results for such a small system are far from the thermodynamic limit, since e.g. the critical value of intermolecular distance $b_{\rm crit}^{(i)} = 2.39 a_0$ corresponds to the volume $V = 0.86$ cm^3/mol for the ideal *hcp* structure. However, the qualitative agreement is remarkable and suggests the crucial role of the electron correlations in the hydrogen metalization, as the correlated interaction of dipolar moments is most effective for the parallel orientation of the molecules. A separate question concerns the possible metallization at lower pressure, before dissociation (Mao and Hemley, 1994); that transition has no connection with the structure of H_4 cluster considered.

The problem seems to be a very interesting subject of study e.g. within the dynamical mean–field theory combined with *ab initio* calculations (Anisimov, Potaryaev, Korotin, Anokhin and Kotliar, 1997; Nekrasov, Held, Blümer, Potaryev, Anisimov and Vollhardt, 2000), where one can treat electron correlations exactly in the limit of large coordination number. In the remaining part of the thesis we concentrate on low dimensional systems, such as the fermionic ladders, which are discussed in the next Chapter, in order to treat the metallization due to band overlap first in a rigorous manner, within the EDABI method.

Chapter 5

The fermionic ladders

The fermionic ladders, considered in this Chapter, are interesting objects to study within the EDABI method for the two main reasons. *First,* one can look for the metal–insulator transition (due to the band overlap) when the system geometry corresponds to 1D molecular crystal, in analogy to the hydrogen metalization in 3D (Mao and Hemley, 1994). Although such considerations are limited to the small cluster, we have the major advantage of treating such a system in a rigorous manner, including the electron correlations. *Second,* an interesting question concerns the presence of the *dielectric catastrophe* (Resta and Sorella, 1999) associated with the molecule dissociation, when the system evolves from the band insulator (in the molecular–crystal phase) to the Mott–Hubbard insulator (i.e. independent 1D atomic chains). Thus, changing the ladder geometry, we can analyze both MIT due to band overlap in a molecular crystal phase and that associated with the molecule dissociation.

We focus here, as in the *preceding* Chapter, on two different geometrical configurations of the ladder: (i) with parallel and (ii) with perpendicular orientation of the molecules, as depicted schematically in Figure 5.1. Exploring of the two–dimensional parameter space, defined by the bond length a and the intermolecular

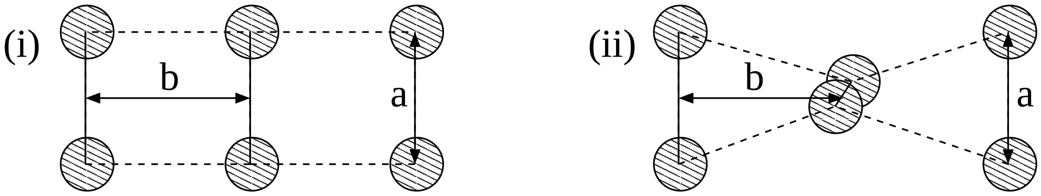

FIGURE 5.1: Schematic representation of the two ladder geometries: (i) parallel and (ii) perpendicular orientation of the molecules. Geometrical parameters of the ladder are: the bond length a and the intermolecular distance b.

distance b, involves a large computational effort for the system sizes $N = 8 \div 12$ atoms. A large part of this space is also physically uninteresting, as in the model case of H_4 cluster. Because of that, we proceed here as follows: *First,* we determine the system properties as a function of the intermolecular distance b, for the optimal bond length $a = a_{\min}$, and for both the geometrical configurations (i) and (ii). *Then,* we analyze the most interesting static and dynamical correlation functions versus a, for specific values of b (close to the dissociation point $b = b_{\text{crit}}$), and for the planar geometry (i). The latter choice is persuaded by the fact, that for the perpendicular molecule orientation (ii) dissociation splits the system into four independent atomic chains, that leads to a small number of sites per chain $(N/4)$ for the system size $N \leqslant 12$.

5.1 The Hamiltonian and microscopic parameters

We now consider a ladder of $N = 8 \div 12$ atoms, each containing a single valence electron (hydrogenic–like atoms), including the *long–range* part of the Coulomb interaction exactly (the microscopic parameters are calculated in the Gaussian STO–3G basis, that leads to analytical expressions for the three– and four–site terms on the atomic level, *cf.* Appendix A). The system Hamiltonian has again the form of the *extended* Hubbard model

$$H = \epsilon_a^{\text{eff}} \sum_i n_i + \sum_{[ij]\sigma} t_{ij} a_{i\sigma}^{\dagger} a_{j\sigma} + U \sum_i n_{i\uparrow} n_{i\downarrow} + \sum_{i<j} K_{ij} \delta n_i \delta n_j, \tag{5.1}$$

where the effective atomic level ϵ_a^{eff} is given by Eq. (3.7), $\delta n_i \equiv n_i - 1$, the brackets $[ij]$ denotes the summation over the indexes i and j belonging to the same rectangle in Figure 5.1, so we include the hopping terms up to the third neighbor $t_1 \ldots t_3$ ($t_{||i,j||} \equiv t_{ij}$), and the notation for intra– and intersite Coulomb repulsion is standard, U and $K_{||i,j||} \equiv K_{ij}$, respectively. The discrete metric $||i,j||$ is given by the neighbor rank in a molecular crystal configuration, namely

$$||i,j|| = 2 \left| \lfloor i/2 \rfloor - \lfloor j/2 \rfloor \right| + \left| (i \bmod 2) - (j \bmod 2) \right|, \tag{5.2}$$

where $\lfloor x \rfloor$ is the floor function of x, and $\bmod$ denotes the modulo division, defined as $x \bmod y = x - y \lfloor x/y \rfloor$ (Graham, Knuth and Patashnik, 1994). The ladder geometries (i) and (ii) lead to the same Hamiltonian in the second–quantized form of Eq. (5.1), the differences are encoded in the microscopic parameters ϵ_a^{eff}, t_{ij}, U, and K_{ij}. These parameters are calculated in the basis of Wannier functions $\{w_i(\mathbf{r})\}$, composed of $1s$–like Gaussian–type orbitals with the optimized inverse radii α (*cf.* Appendix A).

The construction of the Wannier basis for the ladder proceeds analogously to that presented in Section 4.1.1. The only modification is that of the orthogonal

TABLE 5.1: Microscopic parameters (in Ry) of the planar ladder (i), calculated in the Gaussian STO–3G basis. Corresponding values of the optimal bond length a_{min} and the inverse orbital size α_{min} are provided in Table 5.3.

b/a_0	$\epsilon_a^{\mathrm{eff}}$	t_1	t_2	t_3	U	K_1	K_2	K_3
2.0	0.0404	-1.1576	-0.4252	0.1113	1.968	1.130	0.944	0.752
2.5	-0.2909	-0.9671	-0.2566	0.0589	1.817	1.047	0.778	0.642
3.0	-0.4399	-0.8639	-0.1609	0.0346	1.729	0.999	0.660	0.562
3.5	-0.5133	-0.8028	-0.1013	0.0220	1.678	0.971	0.571	0.500
4.0	-0.5506	-0.7659	-0.0628	0.0142	1.649	0.955	0.501	0.450
4.5	-0.5683	-0.7449	-0.0380	0.0087	1.635	0.947	0.446	0.408
5.0	-0.5754	-0.7340	-0.0225	0.0049	1.630	0.944	0.401	0.373
6.0	-0.5767	-0.7270	-0.0074	0.0010	1.631	0.944	0.334	0.317
7.0	-0.5742	-0.7261	-0.0022	0.0001	1.634	0.946	0.286	0.276
8.0	-0.5723	-0.7262	-0.0005	-0.0000	1.636	0.947	0.250	0.243
10.0	-0.5698	-0.7267	-0.0000	-0.0000	1.639	0.949	0.200	0.197
20.0	-0.5674	-0.7274	-0.0000	-0.0000	1.642	0.951	0.100	0.100

TABLE 5.2: Microscopic parameters (in Ry) calculated in the Gaussian STO–3G basis for the ladder configuration (ii). Corresponding values of the optimal bond length a_{min} and the inverse orbital size α_{min} are provided in Table 5.3.

b/a_0	$\epsilon_a^{\mathrm{eff}}$	t_1	t_2	t_3	U	K_1	K_2	K_3
2.0	-0.3722	-0.7987	-0.1296	-0.1296	1.658	0.960	0.785	0.785
2.5	-0.4628	-0.8188	-0.0937	-0.0937	1.688	0.974	0.690	0.690
3.0	-0.5210	-0.7936	-0.0623	-0.0623	1.663	0.962	0.602	0.602
3.5	-0.5538	-0.7675	-0.0398	-0.0398	1.643	0.951	0.531	0.531
4.0	-0.5709	-0.7484	-0.0245	-0.0245	1.631	0.944	0.473	0.473
4.5	-0.5786	-0.7362	-0.0147	-0.0147	1.626	0.941	0.426	0.426
5.0	-0.5810	-0.7293	-0.0088	-0.0088	1.625	0.941	0.387	0.387
6.0	-0.5786	-0.7254	-0.0032	-0.0032	1.628	0.943	0.326	0.326
7.0	-0.5750	-0.7255	-0.0011	-0.0011	1.633	0.945	0.281	0.281
8.0	-0.5729	-0.7256	-0.0003	-0.0003	1.636	0.947	0.247	0.247
10.0	-0.5698	-0.7268	-0.0000	-0.0000	1.639	0.949	0.198	0.198
20.0	-0.5673	-0.7274	-0.0000	-0.0000	1.642	0.951	0.100	0.100

functions given by Eqs. (4.9) and (4.10), since the molecular orbitals $\Phi^{0,\pi}_{\langle ij\rangle}$ (defined in Eqs. (4.5) and (4.6) for $\langle ij\rangle = \langle 12\rangle$) have a nonzero overlap with those on the left and right, $\Phi^{0,\pi}_{\langle ij\rangle-1}$ and $\Phi^{0,\pi}_{\langle ij\rangle+1}$, respectively. The bracket $\langle ij\rangle$ denotes the pair of atoms belonging to the same molecule in the ladder, so e.g. $\langle 34\rangle - 1 \equiv \langle 12\rangle$, $\langle 34\rangle + 1 \equiv \langle 56\rangle$, etc. (for the numbering order the same as that for the H_4 cluster in Figure 4.1). Therefore, Eqs. (4.9) and (4.10) are replaced by

$$\tilde{\Phi}^{0,\pi}_{\langle ij\rangle} = \beta^{0,\pi}\left[\Phi^{0,\pi}_{\langle ij\rangle} - \gamma^{0,\pi}\left(\Phi^{0,\pi}_{\langle ij\rangle-1} + \Phi^{0,\pi}_{\langle ij\rangle+1}\right)\right], \tag{5.3}$$

in analogy to the expansion (3.9) for the nanochain. The coefficients $\gamma^{0,\pi}$ and $\beta^{0,\pi}$ are given by expressions having the form of Eqs. (3.10) and (3.11), with overlap integrals S_m ($m = 1\ldots 3$) substituted by

$$\left\langle \Phi^{0}_{\langle ij\rangle} | \Phi^{0}_{\langle ij\rangle+m} \right\rangle = (\beta^a)^2\,(1-\gamma^a)^2\,(S_{2m} + S_{2m+1}), \tag{5.4}$$

$$\left\langle \Phi^{\pi}_{\langle ij\rangle} | \Phi^{\pi}_{\langle ij\rangle+m} \right\rangle = (\beta^a)^2\,(1+\gamma^a)^2\,(S_{2m} - S_{2m+1}), \tag{5.5}$$

where β_a and γ_a are given by Eq. (4.3), and the overlap integrals in the atomic basis are defined as $S_{||i,j||} \equiv \langle \Psi_i | \Psi_j \rangle$. We again have $\langle \Phi^{0}_{\langle ij\rangle} | \Phi^{\pi}_{\langle ij\rangle+m} \rangle = 0$ due to the reflection symmetry. The remaining part of the construction is the same as in the case of H_4 discussed in Section 4.1.1.

The model parameters, corresponding to the intermolecular distance $b/a_0 = 2 \div 20$, and the optimal values of the bond length a_{min} and inverse orbital size α_{min} (*see* next Section), are presented in Tables 5.1 and 5.2 for the parallel (i) and the perpendicular (ii) orientation of molecules, respectively. Similarly as in the case of a nanochain (*cf.* Chapter 3), we perform the Richardson extrapolation with the lattice size $N \to \infty$ to obtain the size–independent values of the effective atomic energy ϵ_a^{eff} and the hopping integrals $t_1 \ldots t_3$.

5.2 The optimized ground–state energy

The Hamiltonian (5.1) is diagonalized in the Fock space with the help of Lanczos technique (*cf.* Section 2.2). As the microscopic parameters ϵ_a^{eff}, $t_1 \ldots t_3$, U, and K_{ij} are calculated numerically in the Gaussian STO–3G basis, the bond length a and the inverse orbital size α of the $1s$–like state are subsequently optimized to obtain the ground state energy E_G as a function of the intermolecular distance b. The results for $N = 10$ are presented in Figure 5.2. Due to the closed–shell molecular crystal configuration of the system ground state, the data *almost do not depend on the system size* (e.g., analogical results for $N = 8$ fit onto those shown in Figure 5.2 up to the pixel size). The corresponding values of the optimal bond length a_{min} and the inverse orbital size α_{min}, provided in the *insets* of Figure 5.2,

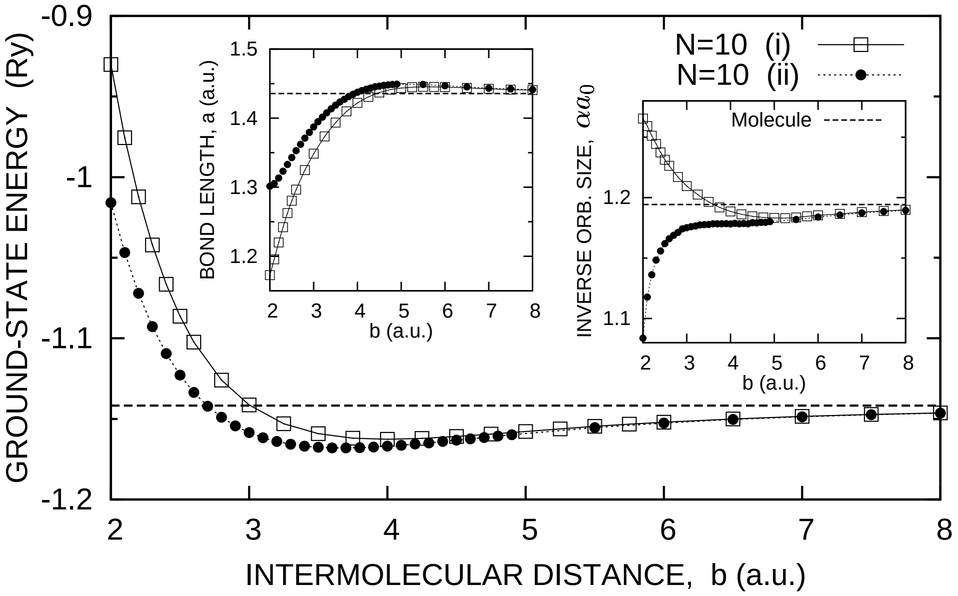

FIGURE 5.2: The ground–state energy per atom for the ladder of $N = 10$ atoms with periodic boundary conditions. *Insets* provide the values of the optimal bond length $a_{\min}$ (*left*) and the inverse orbital size $\alpha_{\min}$ (*right*). The Gaussian–type orbitals (STO–3G basis) have been used.

TABLE 5.3: The optimal bond length $a_{\min}$, inverse orbital size $\alpha_{\min}$, and the ground–state energy for the ladder of $N = 10$ atoms.

	Parallel (i)			Perpendicular (ii)		
b/a_0	$a_{\min}$	$\alpha_{\min}$	E_G/N	$a_{\min}$	$\alpha_{\min}$	E_G/N
2.0	1.173	1.265	-0.9301	1.301	1.084	-1.0158
2.5	1.280	1.231	-1.0862	1.343	1.162	-1.1228
3.0	1.349	1.210	-1.1413	1.387	1.175	-1.1585
3.5	1.394	1.196	-1.1591	1.419	1.178	-1.1676
4.0	1.422	1.189	-1.1626	1.437	1.179	-1.1670
4.5	1.437	1.185	-1.1609	1.446	1.179	-1.1632
5.0	1.444	1.183	-1.1578	1.449	1.180	-1.1590
6.0	1.445	1.185	-1.1521	1.447	1.184	-1.1525
7.0	1.443	1.188	-1.1485	1.443	1.187	-1.1487
8.0	1.441	1.190	-1.1463	1.441	1.189	-1.1464
10.0	1.438	1.192	-1.1441	1.438	1.192	-1.1442
20.0	1.436	1.194	-1.1421	1.436	1.194	-1.1421

are also listed in Table 5.3 for both the ladder geometries (i) and (ii). The global minima of the ground–state energy E_G are achieved for:

$$b_{\text{min}}^{(i)} = 4.00a_0, \qquad a_{\text{min}}^{(i)} = 1.422a_0, \qquad \alpha_{\text{min}}^{(i)} = 1.189a_0,$$
$$E_G^{\text{min}(i)}/N = -1.1626\text{ Ry}, \tag{5.6}$$

for the planar ladder geometry, and

$$b_{\text{min}}^{(ii)} = 3.67a_0, \qquad a_{\text{min}}^{(ii)} = 1.426a_0, \qquad \alpha_{\text{min}}^{(i)} = 1.178a_0,$$
$$E_G^{\text{min}(ii)}/N = -1.1680\text{ Ry}, \tag{5.7}$$

for the case of perpendicular molecule orientation (ii). These values leads to the binding energies of the molecules in ladders $\Delta E_G^{(i)}/N = 20.8 \cdot 10^{-3}$ Ry and $\Delta E_G^{(ii)}/N = 26.2 \cdot 10^{-3}$ Ry, respectively, that are about three times larger than the corresponding $\Delta E_G^{(i)}$ and $\Delta E_G^{(ii)}$ in the H_4 cluster (*cf.* Section 4.2.1). One should also note the maxima of the optimal bond length a_{min} as a function of b, as well as the minima of $\alpha_{\text{min}}(b)$ (*cf.* Figure 5.2, *insets*), which are close to the global minima of E_G (5.6) and (5.7), and correspond to the attractive interaction in the system.

The optimized ground–state energy E_G studied as a function of a for a fixed b, is depicted in Figure 5.3 for the planar ladder geometry (i). $E_G(a)$ shows a very similar behavior to that observed in the case of H_4 cluster (*cf.* Section 4.2); the critical values of the intermolecular distance b, corresponding to the molecule dissociation, are now equal to

$$b_{\text{crit}}^{(i)} = 2.06(1)a_0 \qquad \text{and} \qquad b_{\text{crit}}^{(ii)} = 1.93(2)a_0,$$

for the respective ladder geometries. The number in brackets indicates an extrapolation error (with $1/N \to 0$) on the last decimal place, estimated from the data for the system sizes $N = 8 \div 12$. In the first case (i) the system splits into two independent atomic chains with the lattice parameter $a_{\text{chain}} = b$, whereas in the second case (ii) four resulting chains are characterized by $a_{\text{chain}} = 2b$. Such scenario is caused by the constrains in the system, supposed arbitrarily to reduce the number of geometrical parameters to a and b only. However, the obtained values of b_{crit} seem valuable since they illustrate, together with the related data for the H_4 cluster, the convergence of $b_{\text{crit}}^{(i)}$ and $b_{\text{crit}}^{(ii)}$ to each other when increase the system dimensionality. The dissociation has again the nature of the first–order phase transition, since it corresponds to the switching between the well–separated minima of the ground state energy $E_G(a)$ with respect to the bond length a, which is significantly smaller than b (and decrease) when approaching the critical value $b \approx b_{\text{crit}}$ (*cf.* Table 5.3).

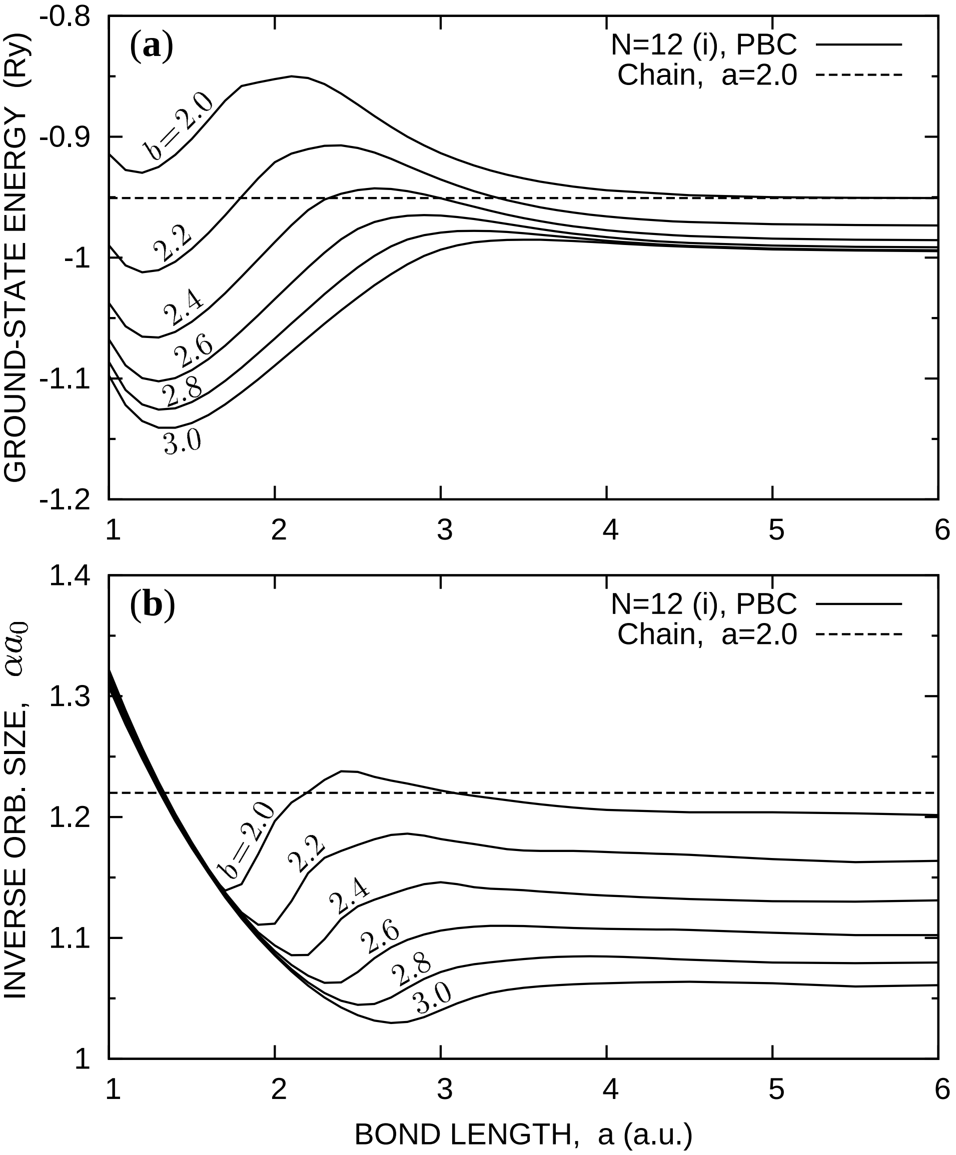

FIGURE 5.3: Ground–state energy per atom for the planar ladder of $N=12$ atoms (a) with a fixed intermolecular distance b (specified in the units of Bohr radius a_0), and (b) the corresponding values of the optimal inverse orbital size α_{min}. Periodic boundary conditions are used. The results for the atomic chain (*dashed* lines) with a lattice parameter $a \lesssim b_{\text{crit}}$ are shown for the comparison.

5.3 Ground–state properties

In this Section we analyze the ladder ground–state properties, first as a function of the intermolecular distance b for the optimal values of the bond length $a_{\rm min}$ and inverse orbital size $\alpha_{\rm min}$ (determined in the *previous* Section) and for both ladder configurations (i) and (ii) (*cf.* Figure 5.1), and then as a function of the bond length a for few fixed values of b (close to the critical distance $b_{\rm crit}$ determined in the *previous* Section) and for the planar ladder geometry (i). The *periodic* or *antiperiodic* boundary conditions are used to minimize the ground–state energy for the system containing $N = 8 \div 12$ atoms, as discussed in Section 3.3.2. We concentrate here on the ladders with one electron per atom (corresponding to *hydrogenic–like* atoms).

5.3.1 Spin and charge correlation functions

In Figure 5.4 we present the spin– and charge–density fluctuations for the ladder of $N = 12$ atoms as a function of the discrete distance $\|i,j\|$ defined by Eq. (5.2).

The spin–spin correlation function $\langle \mathbf{s}_i \cdot \mathbf{s}_j \rangle$ shows an almost exponential decay with $\|i,j\|$ for the planar ladder geometry (i) (*cf.* Figure 5.4a) and decrease abruptly on the second–neighbor for the perpendicular molecule orientation (ii) (*cf.* Figure 5.4b). Such behavior is caused by the spin frustration in the system of two perpendicularly orientated molecules (ii) on the neighboring sites. The sign of spin–spin correlation functions is alternating with $\|i,j\|$, due to the short–range *kinetic exchange* interaction. An interesting feature of the planar ladder (i) is a nonzero value of $\langle \mathbf{s}_i \cdot \mathbf{s}_j \rangle$ on further neighbors, even for a relatively large lattice parameter $b/a_0 = 3 \div 4$, since one can expect the closed–shell (*spin–singlet*) molecular crystal configuration to not show the magnetic order. This illustrates again the important role of the electron correlations for the system of the planar geometry, in analogy to the results for the H_4 cluster (*cf.* Section 4.2).

The situation is quite different in the case of charge–density correlation function $\langle \Delta n_i \Delta n_j \rangle$, which also decays exponentially with the neighbor distance $\|i,j\|$, but is rather insensitive on a change of the intermolecular distance b for both the considered ladder geometries (*cf.* Figure 5.4c and 5.4d). This behavior illustrates the long–range nature of the electron correlations induced by the intermolecular Coulomb interaction present in the Hamiltonian (5.1). The sign order of $\langle \Delta n_i \Delta n_j \rangle$, depicted schematically in Figures 5.4e and 5.4f), is also nontrivial. In the case of planar geometry (i), the long–range order with the domains containing three molecules (*half* of the system size) is energetically preferred, in spite of the domain–wall occurrence (*cf.* Figure 5.4e). The case of perpendicular geometry (ii) looks analogically (*cf.* Figure 5.4f), as the similar charge order is present in two separated sublattices, each containing a single molecule. Thus, the long–

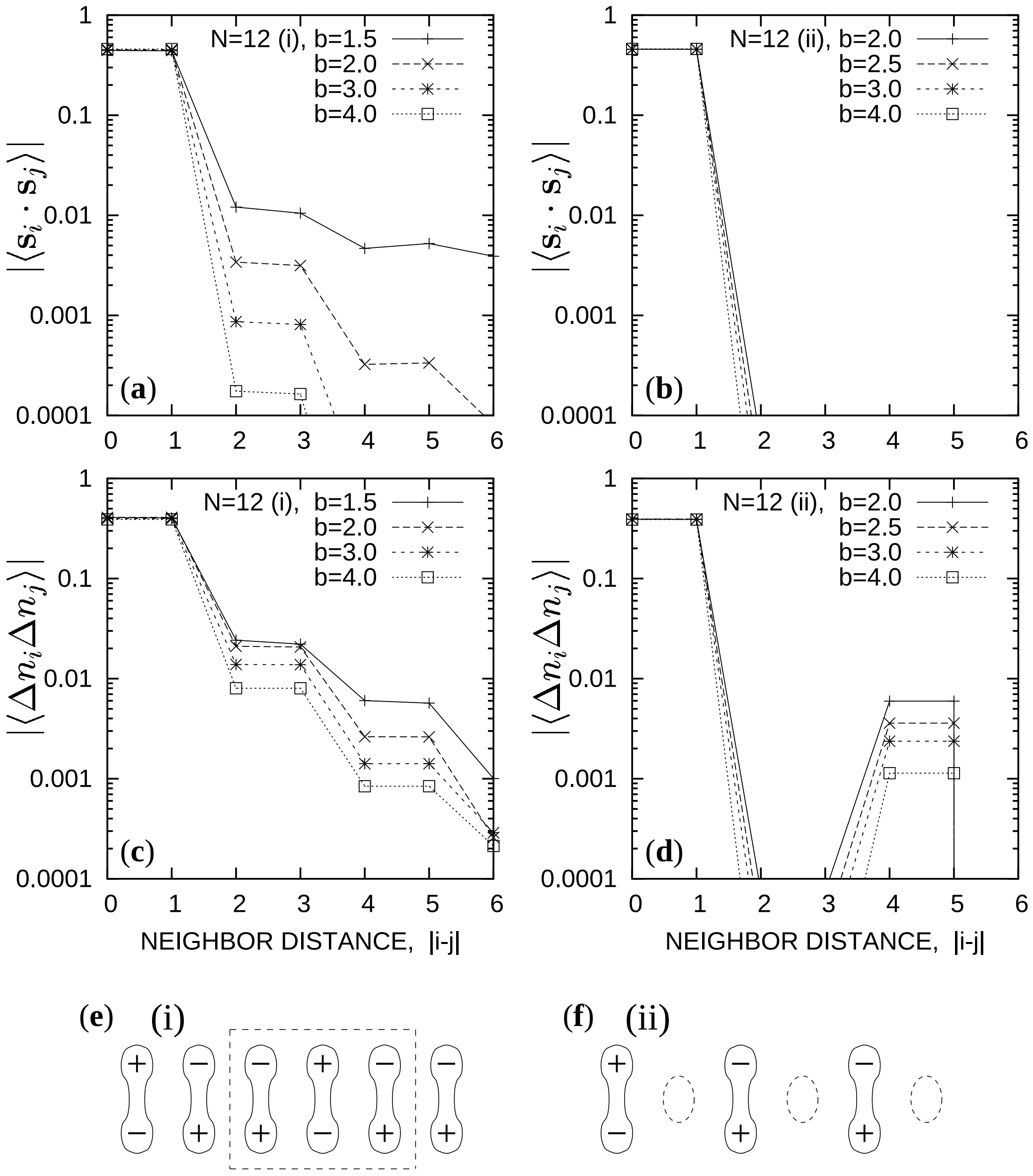

FIGURE 5.4: Spin and charge correlation functions for the ladder of $N = 12$ atoms with periodic boundary conditions: (a) the spin–spin fluctuation for the planar geometry (i), and (b) for the case of perpendicular (ii) molecule orientation; (c) and (d) — the charge–charge fluctuations for the ladder geometries (i) and (ii), respectively; and (e), (f) — the charge–density sign order for the two geometries. *Note* the logarithmic y–axis scale in Figures (a) – (d).

range charge order for the geometry (ii) survives the frustration present in the nearest–neighbor interaction of two perpendicularly orientated electric dipoles. The corresponding results for $N = 8$ shows the charge frustration even in the planar case (i), since the three–molecule domain configuration is again preferred in comparison to the strictly alternant order. Also, the momentum distribution differs remarkably from that for the atomic chain (*cf.* Chapter 3).

5.3.2 Electron and hole momentum distributions

We analyze here the electron–momentum distribution function, defined as

$$n_{0\mathbf{k}\sigma} = \langle a^{\dagger}_{0k\sigma} a_{0\mathbf{k}\sigma} \rangle, \qquad n_{\pi\mathbf{k}\sigma} = \langle a^{\dagger}_{\pi\mathbf{k}\sigma} a_{\pi\mathbf{k}\sigma} \rangle, \tag{5.8}$$

for the bonding and anti–bonding bands, respectively. The results for the ladder with an optimal bond length a_{min}, containing $N = 8$ and 12 atoms, are shown in Figure 5.5. In the case of planar geometry (i) (*cf.* Figure 5.1), and for the small values of the bond length b, one can note the presence of holes in the bonding (*cf.* Figure 5.5a) and electrons in the anti–bonding band (*cf.* Figure 5.5b), centered around the momenta $k = \pi/b$ and $k = 0$, respectively. The situation for the perpendicular geometry (ii) looks similarly in the case of the bonding band (*cf.* Figure 5.5c), whereas in the anti–bonding bound electrons are uniformly in the Brillouin zone (*cf.* Figure 5.5d). Such picture follows from that based on the dispersion relations for the noninteracting system

$$\epsilon_{0\mathbf{k}} = -t_1 + 2(t_2 + t_3)\cos kb, \qquad \epsilon_{\pi\mathbf{k}} = t_1 + 2(t_2 - t_3)\cos kb, \tag{5.9}$$

if we note that $t_2 = t_3$ for the geometry (ii), due to the system symmetry. A very small amount of the particle–hole excitations away from the band overlap point, for which $|t_1| - 2|t_2| < 0$, allows one to consider the system as a molecular crystal (see *next* Section for the charge gap data).

The situation changes dramatically when direct band overlap takes place in the momentum space. One can arrive at such a situation by changing the bond length a (and, as a result, the intramolecular hopping t_1) for a fixed value of the intermolecular distance b (so t_2 remains almost constant). The resulting electron momentum distribution for the planar ladder (i) is presented in Figure 5.6. We observe the systematic flow of the quasiparticles from the bonding to the anti–bonding band until the half–filled band situation (in the system with one electron per atom) is achieved, e.g. for $a \gtrsim 3a_0$ if $b = 2a_0$ (*cf.* Figures 5.6a and 5.6b), and for $a \gtrsim 4a_0$ if $b = 3a_0$ (*cf.* Figures 5.6c and 5.6d). To describe such process quantitatively, we define the total number of particle–hole excitations

$$N_0^h \equiv \sum_{\mathbf{k}\sigma} \langle a_{0\mathbf{k}\sigma} a^{\dagger}_{0\mathbf{k}\sigma} \rangle = N_\pi^e \equiv \sum_{\mathbf{k}\sigma} \langle a^{\dagger}_{\pi\mathbf{k}\sigma} a_{\pi\mathbf{k}\sigma} \rangle \tag{5.10}$$

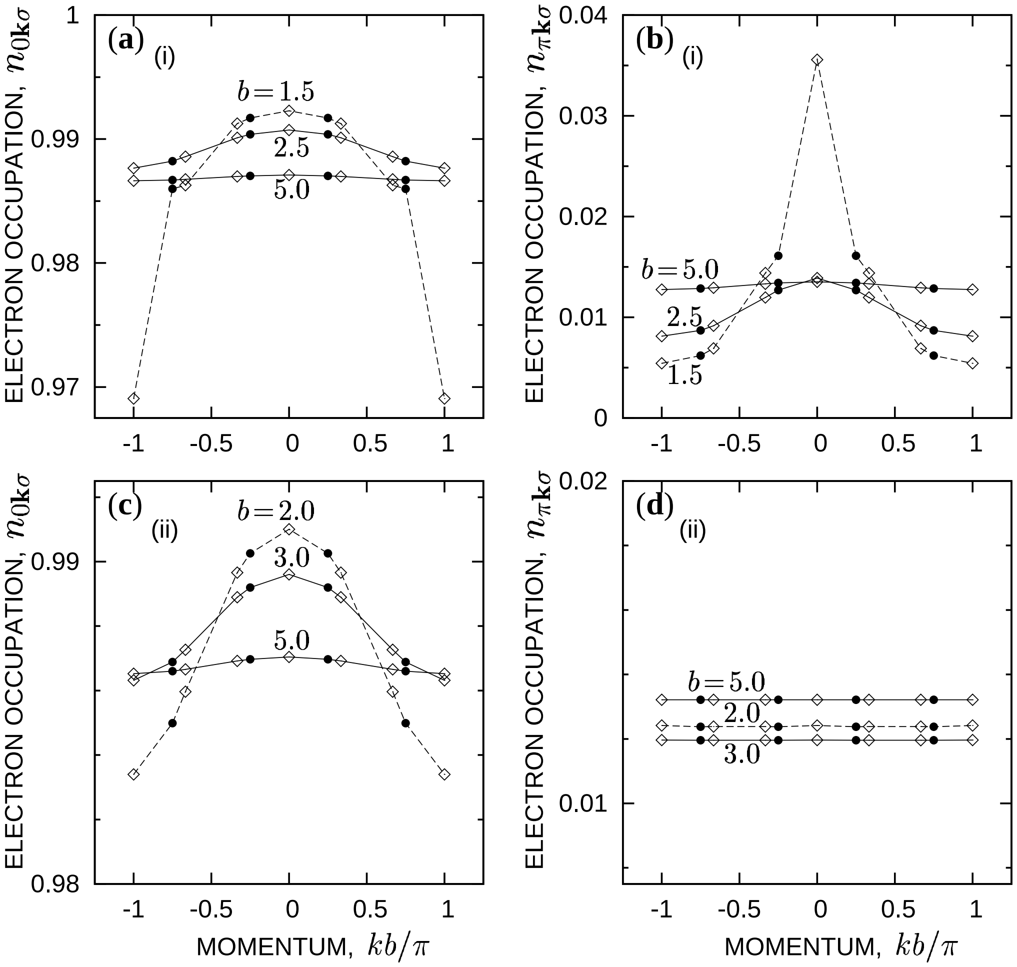

FIGURE 5.5: Electron momentum distribution for the ladder with the optimized bond length $a_{\min}$: (a) the bonding and (b) the antibonding band occupations for the planar ladder configuration (i); (c) the bonding and (d) the antibonding band occupation for the perpendicular molecule orientation (ii). *Dots* mark the results for $N = 8$ atoms with ABC, *diamonds* – for $N = 12$ with PBC. The values of the intermolecular distance b are specified in a_0.

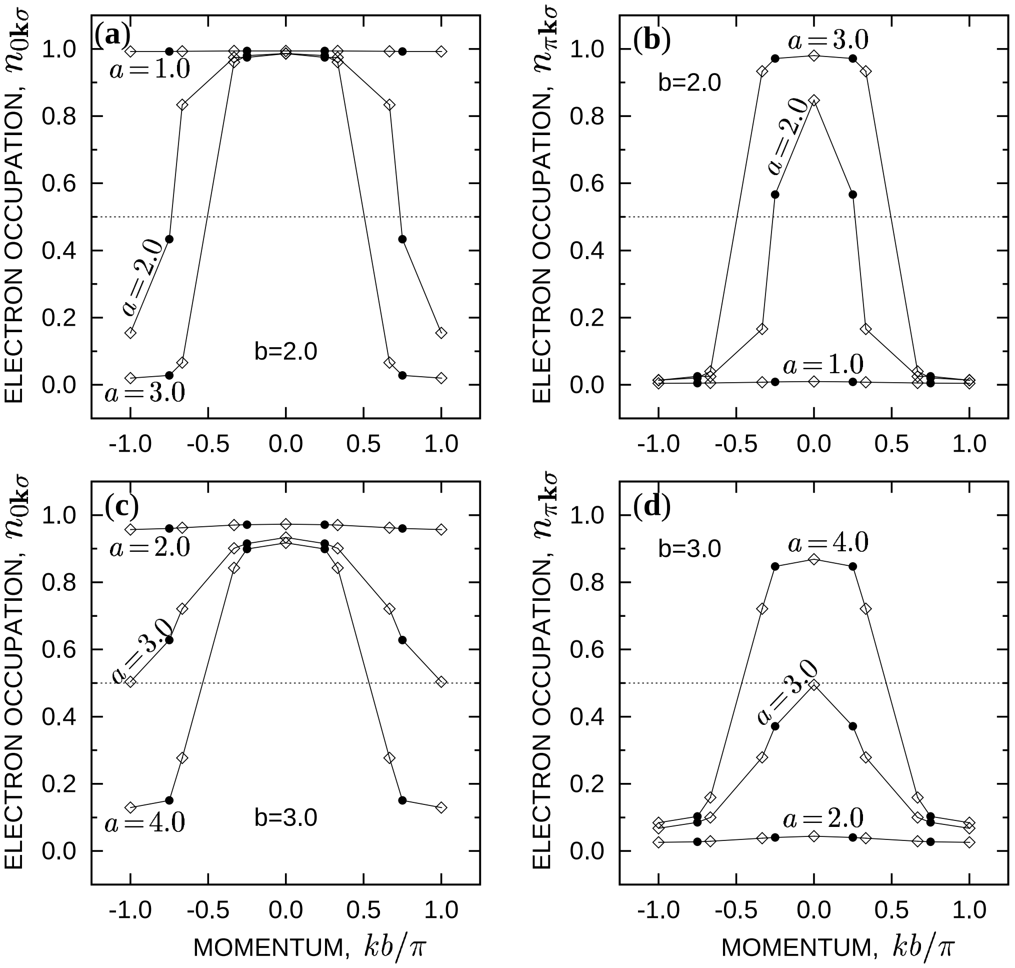

FIGURE 5.6: Evolution of the electron momentum distribution for the planar ladder (i) with varying bond length a (specified in a_0): (a) the bonding and (b) the antibonding band occupations for the value of the intermolecular distance $b = 2a_0$; (c) the bonding and (d) the antibonding band occupation fors $b = 3a_0$. Symbols are the same as in Figure 5.5.

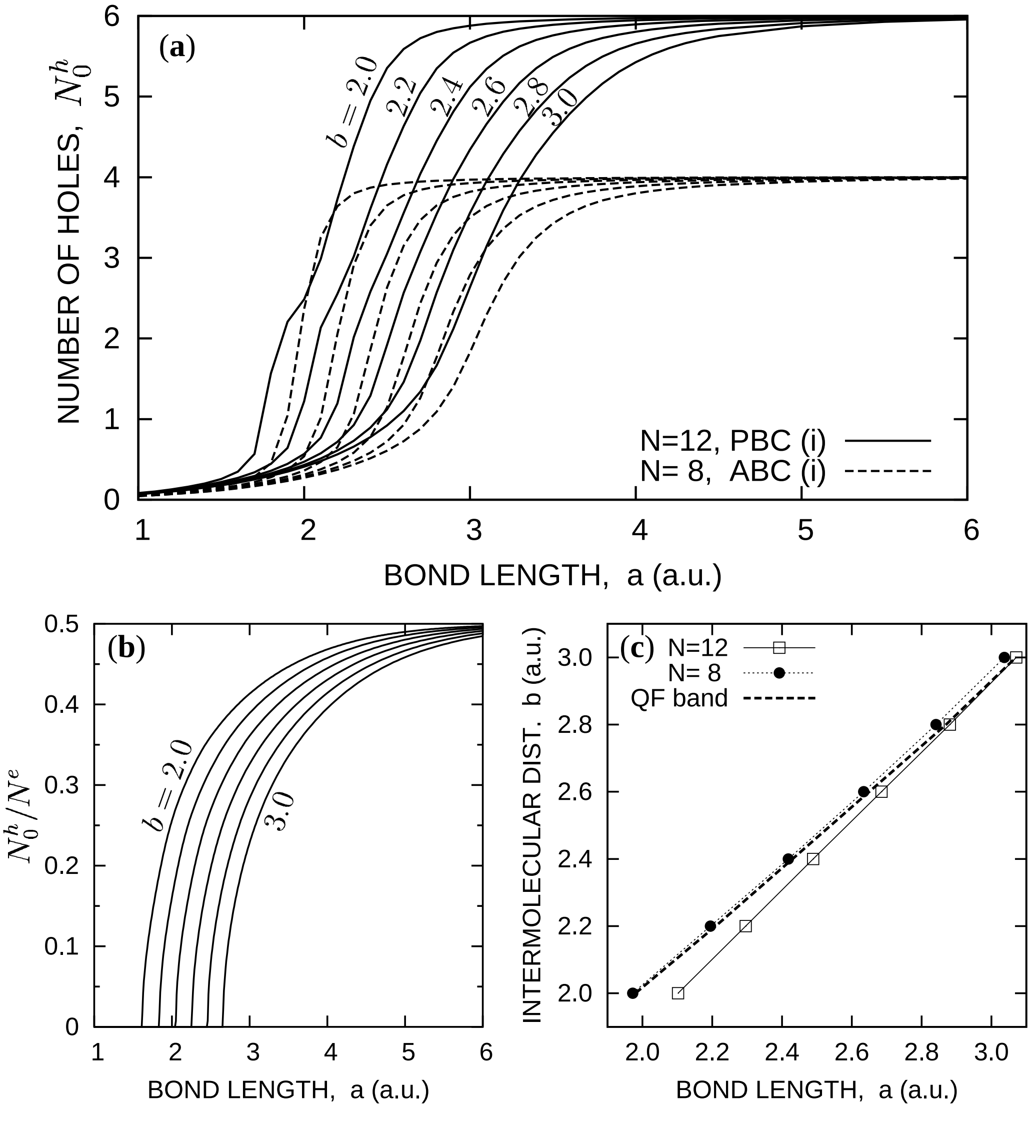

FIGURE 5.7: Effective band filling for the planar ladder (i) versus the bond length a: (a) the number of holes in the bonding band N_0^h, (b) the carrier density N_0^h/N for the noninteracting band model, and (c) positions of the *effective quarter–filling* (QF) points obtained from exact–diagonalization data and from the band model. The values of the intermolecular distance b are specified in a_0.

(note that the total number of electrons is $N_e = N$). The numerical values of N_0^h, provided in Figure 5.7a, shows the crossover transition from the molecular crystal to the system with a half–filled band, which takes place for $a/a_0 = 2 \div 3$, and looks very similarly for both studied system sizes $N = 8$ and 12 (for the purpose of this analysis we suppose ABC for $N = 8$ and PBC for $N = 12$, the problem of choosing BC when varying a is discussed in the *next* Section). The corresponding carrier densities N_0^h/N, obtained from a simple 2–band model with the dispersion relation given by Eq. (5.9), are shown in Figure 5.7b. These results differs significantly from that presented in Figure 5.7a, since such a band model shows the critical behavior

$$N_0^h/N \propto D \propto |t_1 - t_{1\mathrm{crit}}|^{1/2} \sim (a - a_{\mathrm{crit}})^{1/2},$$

absent in the interacting 1D system due to nonexistence of the quasiparticles (*cf.* Section 3.3.3). However, the values of a and b corresponding to the *effective quarter–filling* (QF), for which $N_0^h = N_\pi^e = N/2$, do not differ significantly when obtained from the band model end from the band model and from ED results for $N = 8$ and 12 (*cf.* Figure 5.7c).

The latter aspect seems important from the theoretical point of view. Both the molecular crystal ($a \approx a_{\mathrm{min}} < b$), and the free chain with the half–filled band ($a \gg b$) are predicted to have a zero conductivity: first one due to the closed–shell configuration, the second due to the weak coupling RG analysis by Fabrizio (1996), which relate the metallic or insulating character of the 1D system at a half–filling to the number of Fermi points. Nevertheless, around the effective quarter–filling ($a \approx b$), the ladder has four Fermi points in the momentum space, and there are no relevant *umklapp* processes which could drive the system to an insulating phase (Fabrizio, 1996). Becuse of that, one can expect the ladder metallicity around the $N_0^h = N/2$ line, as shown in Figure 5.7c. We verify this hypothesis in the remaining part of this Chapter by estimating the system charge gap (the *next* Section) and the Drude weight (in Section 5.4.2).

5.3.3 Charge–energy gap

In Figure 5.8 we present the charge gap defined by Eq. (3.34), for both parallel (i) and perpendicular (ii) orientation of the molecules with the optimal bond length a_{min} in each case. Since the system ground–state has the closed–shell configuration, the data for $N = 8$ and 12 fit almost exactly to the perturbational result for the molecular crystal

$$\Delta E_C \approx \Delta E_C(\mathrm{H}_2) - 4\,|t_2|\,, \tag{5.11}$$

where

$$\Delta E_C(H_2) \equiv -2\,|t_1| + K_1 + \sqrt{(U - K_1)^2 + (4t_1)^2}$$

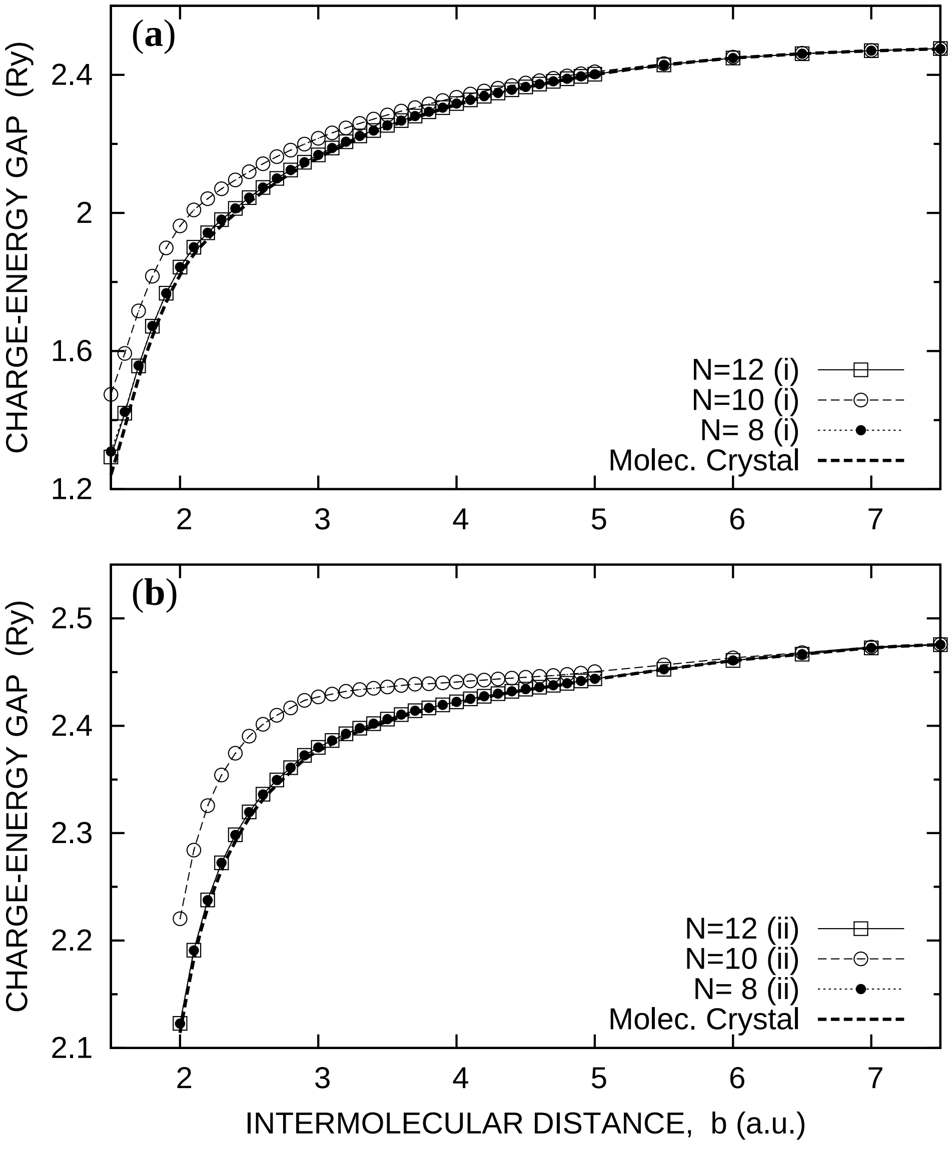

FIGURE 5.8: Charge energy gap versus intermolecular distance b for the ladder with optimized bond length a_{min}: (a) the planar geometry (i) and (b) the perpendicular molecule orientation (ii). The perturbational result for the molecular–crystal solution (*thick dashed* lines) is shown for comparison.

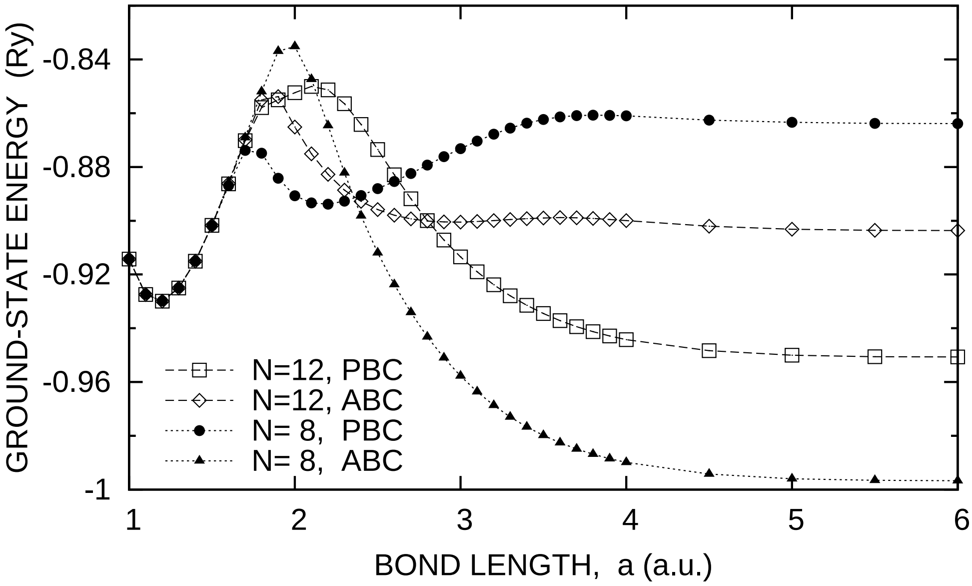

FIGURE 5.9: The boundary–condition effect on the ground–state energy for the planar ladders of $N = 8$ and 12 atoms, with the fixed $b = 2a_0$ and varying a.

denotes the energy gap for the H_2 molecule treated as a two–site problem, and $-4\,|t_2|$ is the effective gap narrowing due to the intermolecular hoppings t_2 and t_3. The differences for $N = 10$ represents the finite–size effect caused by the frustration due to odd number of molecules $N/2 = 5$, that raise the ground–state energy when one electron is added to or subtracted from the system.

Before analyzing the results for the planar ladder with varying bond length a, let us discuss briefly the boundary–condition problem for such system, illustrated in Figure 5.9. In the molecular–crystal range $a \approx a_{\min}$, the ground–state energy E_G is almost independent of BC. However, we found it is always lower for PBC, which also leads to the positive Drude weight (*cf.* next Section). On the other hand, for $a \gg b$, the system is divided into two separate atomic chains of $N/2$ sites each, so the minimal ground–state energy corresponds to PBC for $N = 8n + 4$ (so e.g. for $N = 12$) and to ABC for $N = 8n$. In the intermediate range of $a \sim b$ we have a single switching point for $N = 8$ (in which optimal boundary conditions change from PBC to ABC), and two switching points for $N = 12$ (between which the system prefers ABC).

The charge–energy gap for the planar ladder (i) with the fixed intermolecular distance $b = 2a_0$ and $3a_0$ is shown in Figure 5.10. We choose the optimal BC for a given a, as mentioned above. The results obtained through the linear extrapolation with $1/N \to 0$ (drawn as *solid* lines) show minimum at $a \approx 3a_0$ for $b = 2a_0$ that lays significantly below the limiting value for $a \gg b$. The weaker minimum at

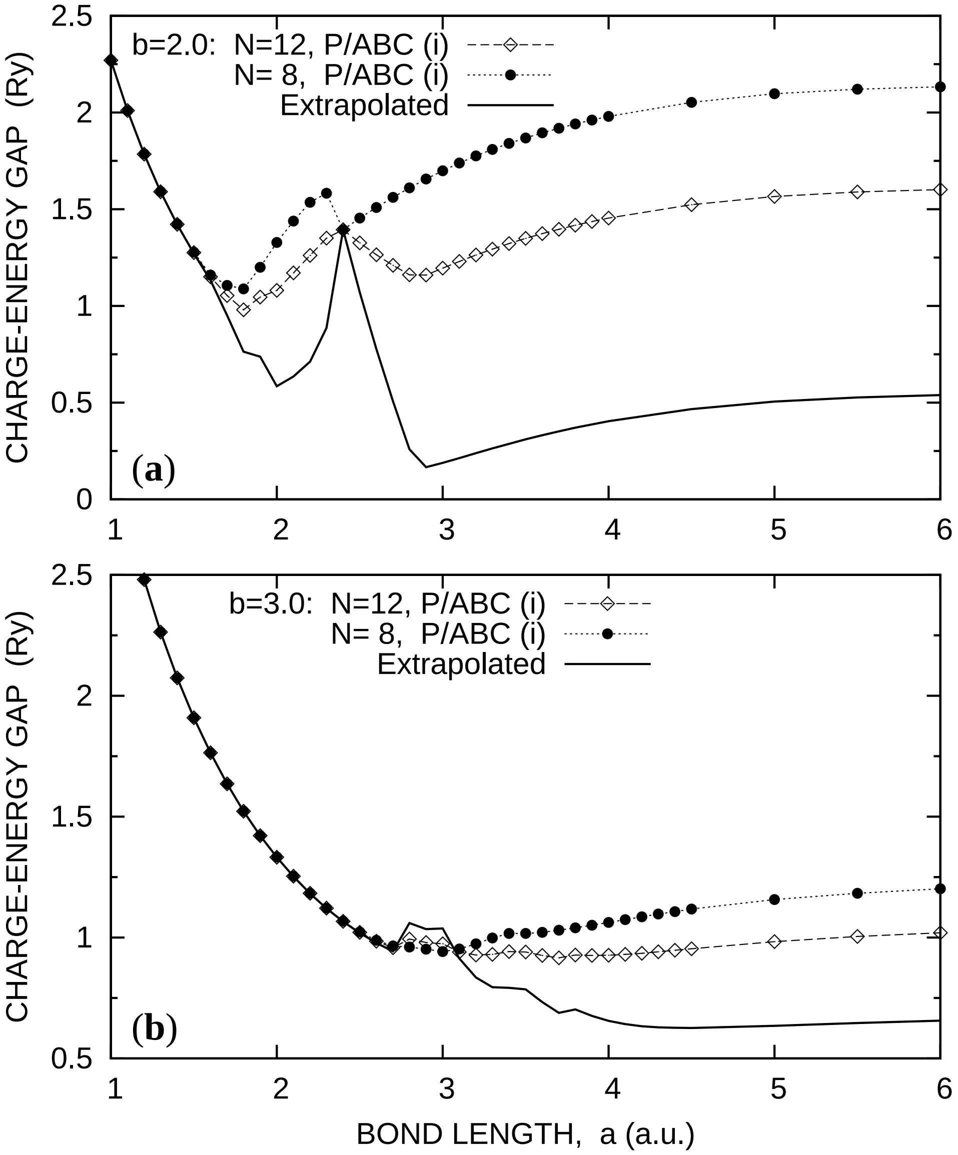

FIGURE 5.10: The charge–energy gap for the planar ladder (i) versus the bond length a. The intermolecular distance b is fixed as (a): $b = 2a_0$ and (b): $b = 3a_0$. The periodic/antiperiodic boundary conditions are chosen to minimize the ground–state energy. The finite–size scaling results are drawn as *solid* lines.

$a \approx 4.5a_0$ for $b = 3a_0$ is also visible. Such behavior suggests the metallicity appearance in the intermediate range of $a \sim b$, where the system transforms form the band– to the Mott–type insulator. However, the scaling quality is relatively poor, since the data for at least $N = 16$ are not available at this time (the data for $N = 10$, or generally $N \neq 4n$, cannot be used in the finite–size scaling, since they show the frustration caused by the odd number of molecules, $N/2$).

5.4 Spectral and transport properties

In this Section we present the ladder dynamical properties calculated with the Lanczos algorithm (*cf.* Section 2.2.2). Analogously as for the system ground–state, we analyze first the ladder with an optimized bond–length $a_{\rm min}$ (so the *molecular–crystal* range) for the both parallel (i) and perpendicular (ii) orientations of the molecules (*cf.* Figure 5.1), and then the planar ladder (i) with varying a. The latter case corresponds to the transformation from the band– to the Mott–type insulator, for which a nonzero conductivity is expected due to a dielectric catastrophe (Resta and Sorella, 1999).

5.4.1 Single–particle density of states

The evolution of the single–particle density of states (*cf.* Section 3.4.1 for the definition) with varying ladder geometry is illustrated in Figures 5.11 and 5.12. In the molecular crystal range $a = a_{\rm min}$ and for the planar ladder geometry (i), the quasiparticle peaks are well–defined for small values of $b \lesssim 3a_0$ (*cf.* Figure 5.11a). With increase b they get closer to each other, and the incoherent part of the spectrum increases in strength and forms the quasi–continuous subbands (corresponding to the bonding and the anti–bonding bands) for the intermediate range of $b/a_0 = 4 \div 5$. These bands evolve to the discrete peaks, corresponding to the ground (H_2^0) and excited (H_2^-) molecular states. The bonding band in the ladder with perpendicular molecule orientation (ii) shows an identical behavior (*cf.* Figure 5.11b) as described above. The antibonding band for such ladder geometry has the form of a discrete peak for any b, as predicted by the dispersionless form of Eq. (5.9), obtained for $t_2 = t_3$.

The density of states for the planar ladder (i) with a fixed $b = 2a_0$ and varying a (*cf.* Figure 5.12) evolves from the set of discrete peaks in the molecular–crystal range of $a \sim 1.5a_0$, to the strongly incoherent spectra for the intermediate $a/a_0 = 2 \div 4$, and again to the set of peaks when the system halves into separate chains of $N/2$ atoms. The ladder of $N = 12$ atoms has also a minimal charge–gap for $a \approx 2.5a_0$, comparable with the separation of quasiparticle states due to the geometrical quantization of the momenta. Such a picture suggests a metallic

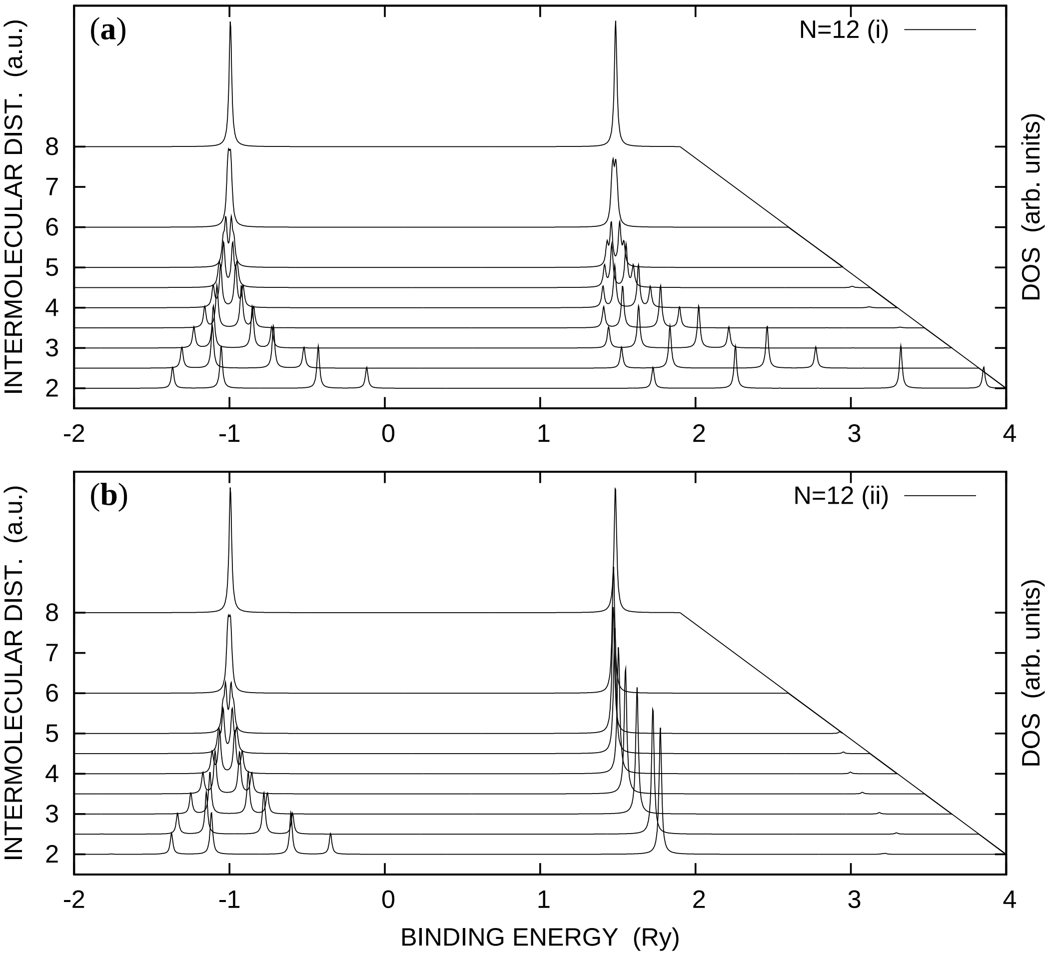

FIGURE 5.11: Density of states for the ladder of $N = 12$ atoms with optimized bond length $a_{\min}$: (a) the parallel (i) and (b) perpendicular (i) orientation of the molecules. True periodic boundary conditions (PBC) are used.

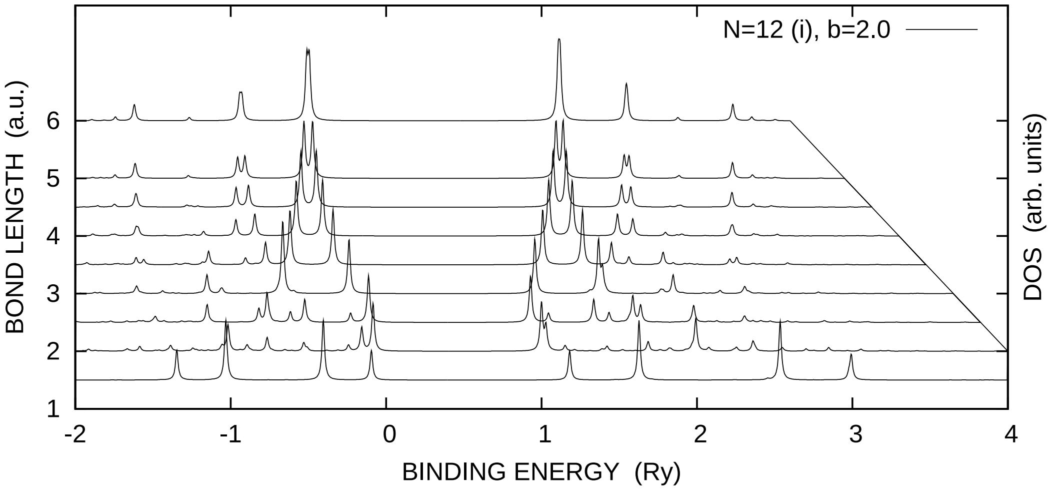

FIGURE 5.12: Density of states for the planar ladder (i) of $N = 12$ atoms with the fixed intermolecular distance $b = 2a_0$ and varying bond length a. The periodic boundary conditions (PBC) are used.

behavior in the large N limit, that we verify by estimating the Drude weight in the *next* Section. One should also note that the spectrum shown in Figure 5.12 has significantly smaller discontinuity (the charge gap) than other cases analyzed in this thesis for the same system size $N = 12$ (*cf.* Figures 3.12 and 5.11).

5.4.2 Charge stiffness

The Drude weight (charge stiffness) for the ladder is defined analogously as that for the atomic chain in Eq. (3.38), but with the current operator 3.39 replaced by

$$j_p = i \sum_{i<j,\sigma} t_{ij} (a_{i\sigma}^\dagger a_{j\sigma} - a_{j\sigma}^\dagger a_{i\sigma})(\delta_{||i,j||,2} + \delta_{||i,j||,3}), \tag{5.12}$$

where the neighbor distance $||i,j||$ is given by Eq. (5.2) and δ_{kl} denotes the Cronecker delta. We again use the *normalized* Drude weight given by Eq. (3.48), providing that the kinetic energy includes now the terms present in the current operator (5.12), namely

$$\langle \Psi_0 | H_{t_2} | \Psi_0 \rangle = t_2 \frac{\partial}{\partial t_2} E_G \qquad \text{and} \qquad \langle \Psi_0 | H_{t_3} | \Psi_0 \rangle = t_3 \frac{\partial}{\partial t_3} E_G, \tag{5.13}$$

where the Hellman–Feynman relation is applied to the ladder Hamiltonian (5.1).

The results presented in Figure 5.13 show that in the molecular–crystal range ($a = a_{\min}$) the system conductivity has a clear residual character due to the finite

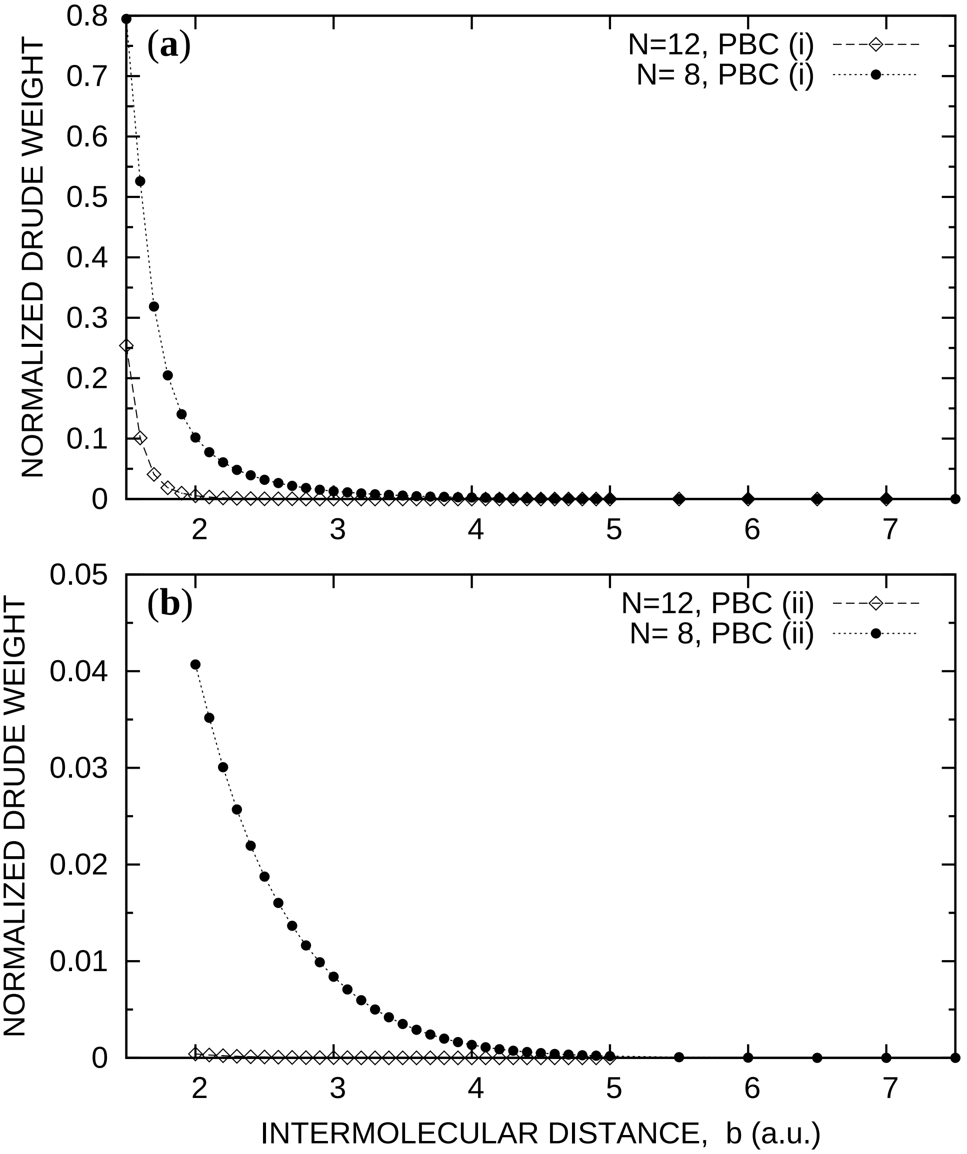

FIGURE 5.13: The normalized Drude weight for the ladder with the optimized bond length a_{min}: (a) the planar ladder geometry (i) and (b) the perpendicular molecule orientation (ii). The periodic boundary conditions (PBC) are used.

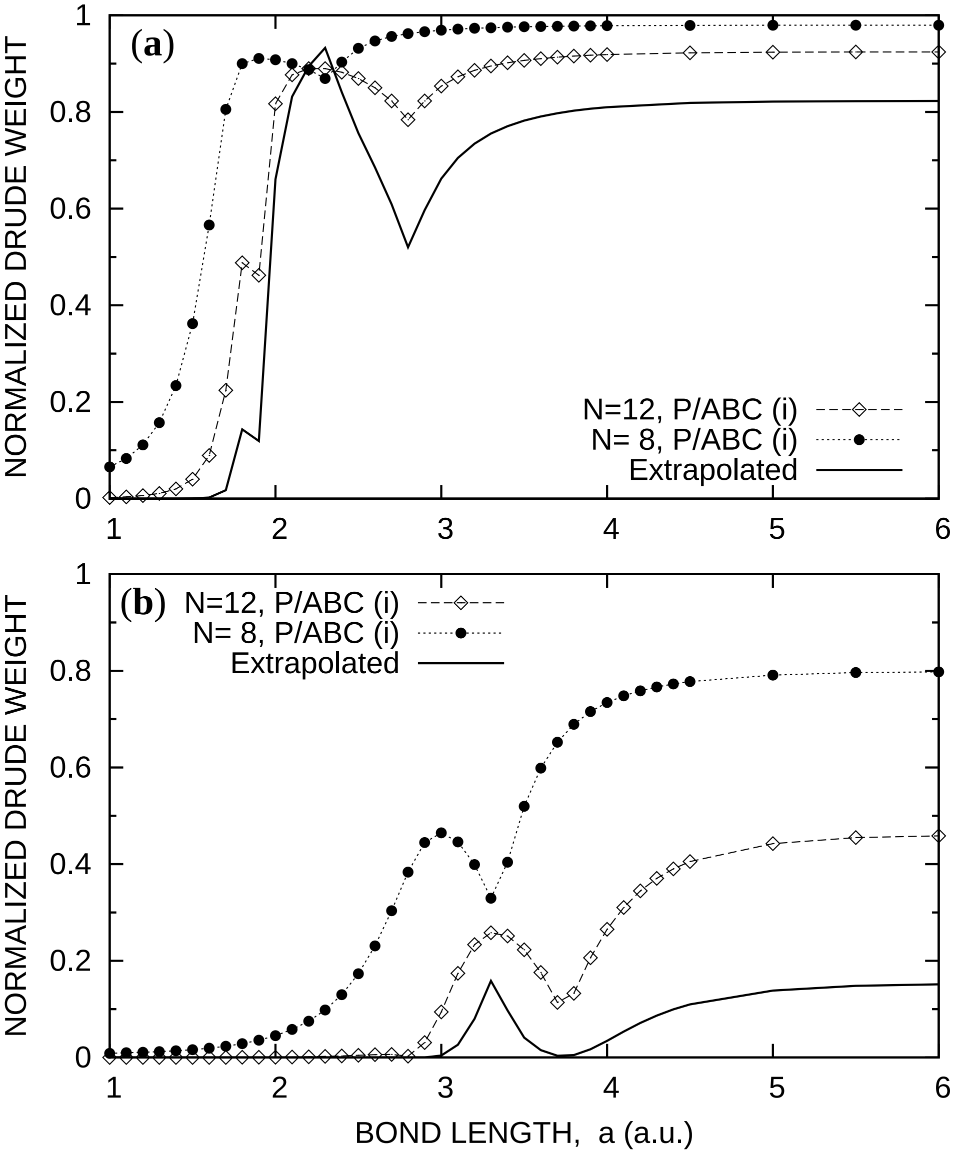

FIGURE 5.14: The normalized Drude weight for the planar ladder (i) with the varying bond length a and the fixed intermolecular distance: (a) $b = 2a_0$ and (b) $b = 3a_0$. *Solid* lines mark the finite–size scaling results for $1/N \to 0$. We use PBC or ABC to minimize the ground–state energy for a given a.

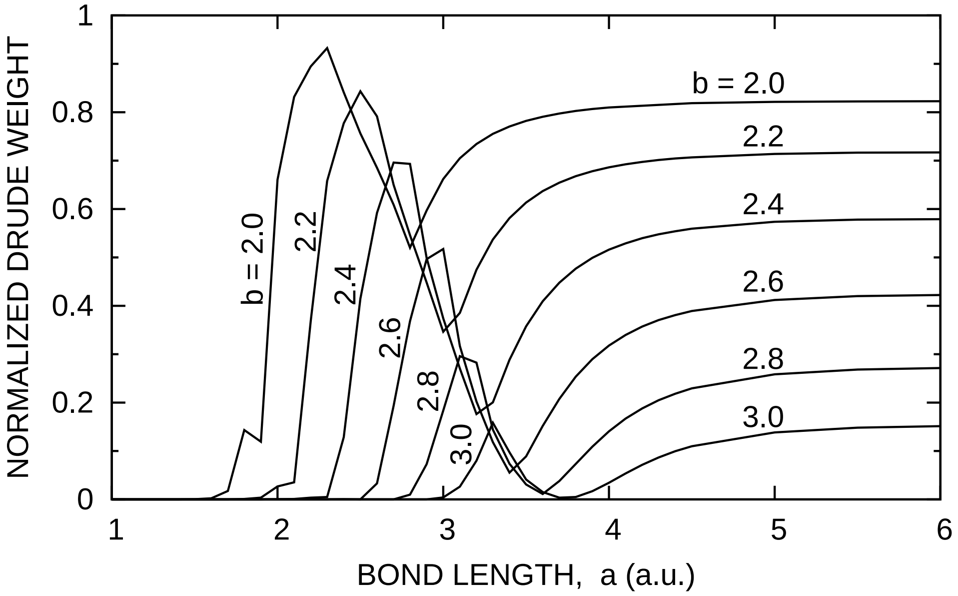

FIGURE 5.15: Evolution of the planar ladder normalized Drude weight versus a, when changing the intermolecular distance b (specified in a_0). The results are obtained through finite–size scaling with $1/N \to 0$.

system size N, and vanish with the growing N, regardless whether the parallel (i) or the perpendicular (ii) molecule orientation (*cf.* Figures 5.13a and 5.13b, respectively) has been taken. Thus, we obtain the direct confirmation, that the close–shell molecular crystal configuration (*cf.* also the density of states in Figure 5.11) corresponds to the band–insulating state.

The situation changes dramatically when we analyze the conductivity along the planar ladder as a function of the bond length a, as presented in Figure 5.14. In this case we observe the well–defined conductivity maxima around $a \approx b$, which evolves into a narrow peak when the finite size scaling of the linear form

$$\ln|D_N^*| = a + \frac{b}{N}$$

is performed with $1/N \to \infty$ (*cf.* the *solid* lines in Figures 5.14a and 5.14b). The position and the intensity of such a peak evolves gradually with a, as shown in Figure 5.15, but always remains well–separated from the residual conductivity for the Mott–insulating state ($a \gg b$), present due to the finite–size effects. The presence of the conductivity peaks around $a \approx b$ proves the existence of the dielectric catastrophe, similar to those discussed for the generalized Hubbard model with an alternating atomic energy (Resta and Sorella, 1999), present when the system switches between the band– and Mott–insulating states.

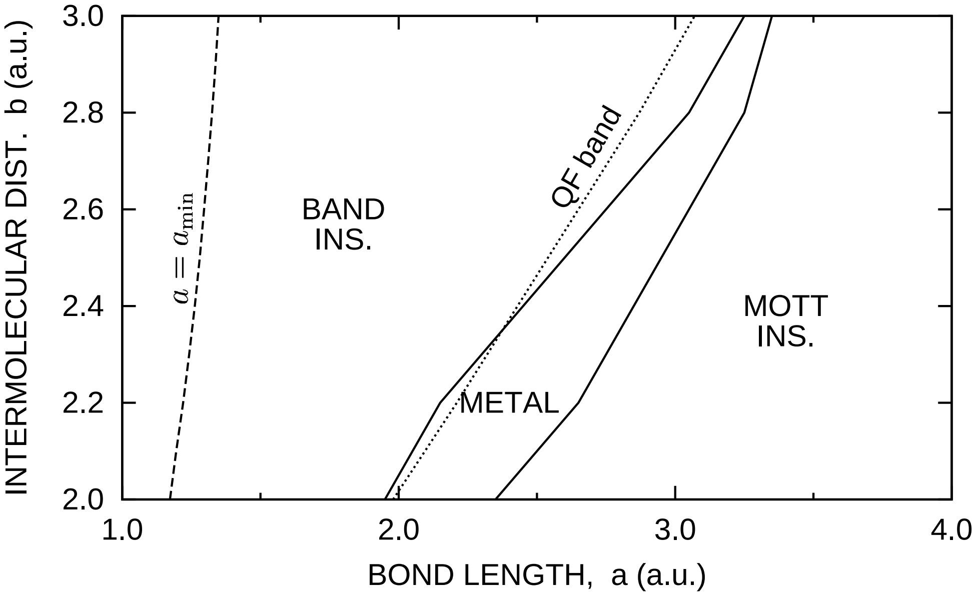

FIGURE 5.16: Phase diagram of the planar fermionic ladder. The optimal value of the bond length $a_{\min}$ is drawn as a *dashed* line. *Dotted* line marks the effective quarter–filling obtained from the noninteracting band model.

The above results for the conductivity, together with those concerning the charge gap (*cf.* Section 5.3.3) and the single–particle density of states (*cf.* Section 5.4.1), motivated us to draw phase diagram for the planar ladder as Figure 5.16. In such a system with a dielectric catastrophe, the narrow metallic phase around $a \approx b$ is sandwitched in between the band– and the Mott–type insulating phases for $a \lesssim b$ and $a \gtrsim b$, respectively. The limiting lines were obtained from the inflection points of D^* vs. a, ploted in Figure 5.15. We observe that the middle part of the metallic phase (corresponding to the maximal conductivity) is placed to the right of the *effective quarter–filling* line obtained for the band model in Section 5.3.2 (and close to the ED data concerning the effective band filling, *cf.* Figure 5.7c). This suggests that the interaction prefers the closed–shell, band–insulating configuration in the correlated state, presumably due to the smaller charge fluctuations along the ladder axis.

5.5 A brief summary

In this Chapter we applied EDABI method to the analysis of the properties of fermionic ladders as function of their geometrical parameters: the bond length a and the intermolecular distance b. The principal results presented here are the following:

- The existence of a critical intermolecular distance $b_{\text{crit}}^{(i)}$ and $b_{\text{crit}}^{(ii)}$, for which the ground–state energy of the separate atomic chains is lower that for the ladder, and the convergence of these values with the coordinational number, suggested by the comparison with the analogical results for the H_4 cluster.
- A nontrivial charge order induced by the long–range part of the Coulomb interactions regardless of the molecule orientation.
- The validity of a simple molecular–crystal perturbation approach in description of the ladder with an optimized bond length a_{min}.
- The deep charge–gap minimum and the conductivity peak for the planar ladder with varying bond length a, separating the band– and the Mott–type insulating phases.

The last result shows the presence of the dielectric catastrophe and the resulting metallic phase of the ladder, in agreement with existing studies of different parametrized models, for which the i.e. the electric polarizability become singular when the insulating order changes from the band– to the Mott–type (Resta and Sorella, 1999).

Chapter 6

Concluding remarks

In this thesis, we have analyzed the ground–state, the spectral, and the transport properties of finite nanochains, clusters, and fermionic ladders, within the novel (EDABI) method of approach to the strongly correlated electron systems. For the chains and ladders, we proposed the microscopic criteria for the *crossover* transition from a nanometal to the localized spin system in one dimension, which was analyzed in relation to spectral and transport properties obtained with the help of the Lanczos technique for an optimized Gaussian–type STO–3G basis. In the first case, the criterion based on the Tomonaga–Luttinger theory was shown to be of qualitative for the nanosystems of $N \leqslant 16$ atoms, in which the metallic and insulating features coexist for the half–filled band case. The distinction between the Fermi– and Luttinger–liquid behavior has been discussed on the example of the electron–momentum distribution in both theories. The system also shows the metal–insulator transition with the increasing lattice parameter at the quarter filling. For the case of fermionic ladders, however, an analogical criterion based on the band theory and the weak–coupling renormalization group analysis by Fabrizio (1996) proves valuable in estimating the dielectric catastrophe point, when the system transforms from the band– to the Mott–type insulating phase, showing the metallic behavior for an intermediate range of the lattice parameter. The analysis of H_4 cluster stability, together with that for the ladders, shows an interesting convergence with the coordination number, in direct correspondence to the structural transition from the molecular to the atomic phase, predicted for the solid hydrogen at ultra–high pressure.

Among the future applications of our method are the following topics:

(i) A direct treatment of the realistic 1D systems with the single–band extended Hubbard model. This most straightforward application concerns only a limited class of materials. However, as the Hilbert space of various organic conductors can be effectively reduced by choosing only the highest occupied-

(HOMO) or the lowest unoccupied (LUMO) molecular orbitals per structural unit, this direction seems realizable.

(ii) Application to other models tractable within the Lanczos technique, e.g. the $t-J$ model for planar clusters. This aspect looks very interesting due to the recently discovered superconductivity in the $\mathrm{Na}_x\mathrm{CoO}_2 \cdot y\mathrm{H}_2\mathrm{O}$ compound, providing new ideas about the effective dielectric constant modification, induced by H_2O presence.

(iii) The combination of the approximate methods of solving parametrized Hamiltonians with a simultaneous *ab initio* readjustment of the Wannier functions. This approach, i.e. for the case of Gutzwiller method (possibly combined with few Lanczos steps) will allow us to consider 3–dimensional systems of a larger size. The study of correlated electrons in materials such as the metallic hydrogen, or truly 1D systems (e.g. carbon nanotubes), seems tractable.

(iv) Closely related to the above is a combination of the dynamical–mean field treatment with *ab initio* methods, which seems promising e.g. for the study of hydrogen metallicity in 3D, as well as for other strongly correlated electron systems.

It would be also very interesting to test experimentally presented results on “toy” nanoscopic systems, such as linear chains of single–electron quantum dots (with steered gate potential), or for K/Na atoms wrapped in C_{60} fullerenes.

In conclusion, we have implemented EDABI method in a number of nanoscopic situations. The method is sound in those cases. In general, the single–particle basis readjustment *closes* the solution of the parametrized models and as such *should constitute a standard part of the approach to the strongly correlated systems*. This is simply because in those systems the interaction among the particles must be treated before each of the electrons relaxes to its final single–particle wavefunction in the many–particle correlated state. Hopefully, new methods will be developed to extend this theoretical approach to the extended systems as well.

Appendix A

The Gaussian 1*s*–like basis

In this Appendix we provide a detailed formulas for the interaction parameters calculated in the atomic basis (*primed* notation in Sections 3.1.1 and 3.1.2), when atomic $1s$–like functions are represented as Gaussian–type orbitals.

A.1 Gaussian contraction and basis optimization

We start from defining the $1s$–like orbital center on i–th lattice site as a linear combination (*contraction*) of m Gaussian functions

$$\Psi_i(\mathbf{r}) = \sum_a \beta_a \Psi_i^{(a)}(\mathbf{r}), \qquad \Psi_i^{(a)}(\mathbf{r}) = \left(\frac{2\Gamma_a^2}{\pi}\right)^{3/4} e^{-\Gamma_a^2(\mathbf{r}-\mathbf{R}_i)^2}. \tag{A.1}$$

The coefficients β_a and Γ_a ($a = 1 \ldots m$) are adjusted to minimize the atomic energy on a single site, so the contraction (A.1) takes the form close to Slater $1s$ function (*see* Appendix B) in the energy space. To perform such optimization, we consider the on–site Hamiltonian

$$H_i(\mathbf{r}) = -\nabla^2 - \frac{2}{|\mathbf{r}-\mathbf{R}_i|} \tag{A.2}$$

(in the atomic units), matrix elements of which are equal to

$$\langle \Psi_i^{(a)} | H_i | \Psi_i^{(b)} \rangle = \frac{3 \cdot 2^{5/2}(\Gamma_a\Gamma_b)^{7/2}}{(\Gamma_a^2+\Gamma_b^2)^{5/2}} - \frac{2^{7/2}(\Gamma_a\Gamma_b)^{3/2}}{\pi^{1/2}(\Gamma_a^2+\Gamma_b^2)}. \tag{A.3}$$

One should also remember about the nonorthogonality of the Gaussians composing the contraction (A.1), namely

$$\langle \Psi_i^{(a)} | \Psi_i^{(b)} \rangle = \left(\frac{2\Gamma_a\Gamma_b}{\Gamma_a^2+\Gamma_b^2}\right)^{3/2}. \tag{A.4}$$

Then, we proceed as follows. First of all, to reduce the number of degrees of freedom in Eq. (A.1) we take into account the exponential decay of $\Phi_i(\mathbf{r})$ and postulate the coefficients Γ_a in the form of geometric series

$$(\Gamma_a, a = -k \ldots k) = \left(q^{-k}\Gamma_0, \ldots, q^{-1}\Gamma_0, \Gamma_0, q\Gamma_0, \ldots, q^k\Gamma_0\right); \qquad \text{(A.5)}$$

where we suppose an odd number of Gaussians $m = 2k + 1$, and define two adjustable parameters Γ_0 and q. For a given Γ_a one can perform a simultaneous diagonalization of matrix with elements given by Eq. (A.3) and the metric form (A.4), to obtain the coefficients β_a corresponding to the ground– ($1s$) or excited–state ($2s$, $3s$, etc.) wavefunctions. Since the corresponding eigenergies depends only on two adjustable parameters Γ_0 and q, an appropriate optimization can be performed numerically.

The resulting ground–state energies of a hydrogen atom are listed in Table A.1. The results presented in this thesis were obtained for contractions of $m = 3$ Gaussians (*STO–3G basis* in quantum chemistry), which provides an accuracy on the level of 1% in the energy (*cf.* Table A.1) and requires a reasonable computational effort on calculating the interaction parameters. The corresponding ground– and first–excited state wavefunctions for $m = 3$ and $m = 7$ Gaussians are ploted in Figure A.1 and compared with the exact Slater $1s$ and $2s$ orbitals.

One additional comment should be made about introducing the inverse orbital size α. Here we define the renormalized $1s$–like orbital as

$$\Psi_i(\alpha, \mathbf{r}) = \alpha^{3/2} \sum_a \beta_a \Psi_i^{(a)}(\alpha\mathbf{r}), \qquad \text{(A.6)}$$

TABLE A.1: Ground–state energy (in Ry) for the system with $1s$–like orbital composed of m Gaussians and their deviation from the exact value (-1 Ry). The corresponding optimal contraction parameters Γ_0 and q are also provided.

m	Γ_0	q	E_G	$E_G + 1$
1	0.5319	2.0000	-0.848826	0.151174
3	0.8920	2.2092	-0.991686	0.008314
5	1.2282	1.8927	-0.999125	0.000875
7	1.6142	1.7382	-0.999874	0.000126
9	2.0685	1.6440	-0.999978	$2.20 \cdot 10^{-5}$
11	2.6036	1.5792	-0.999995	$4.48 \cdot 10^{-6}$
13	3.2275	1.5309	-0.999999	$1.03 \cdot 10^{-6}$
15	3.9443	1.4928	-1.000000	$2.69 \cdot 10^{-7}$

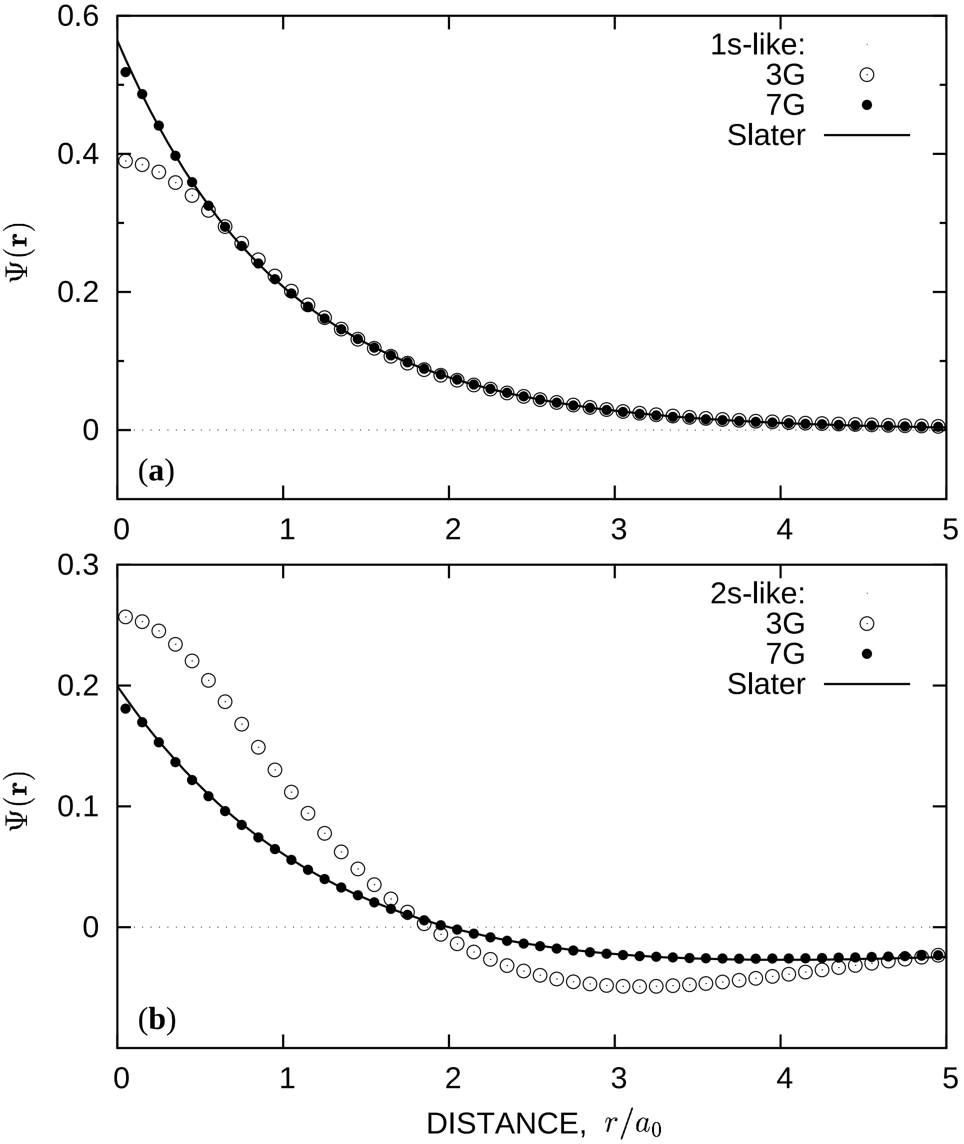

FIGURE A.1: Gaussian–type $1s$– (a) and $2s$–like (b) orbitals composed of 3 and 7 Gaussians and the corresponding *exact* Slater $1s$ and $2s$ functions.

that is equivalent to the transformation $\Gamma_a \to \alpha\Gamma_a$, whereas the coefficients β_a of the contraction (A.1) remains unchanged. One can easily check, that such transformation does not affect the overlap integrals (A.4), so the normalization of the $1s$–like orbitals defined in Eq. (A.6) is preserved for any α. Thus, provided the microscopic parameters can be determined analytically for a given α (*cf.* next Section), the corresponding ground–state energy of an interacting system is calculated and the inverse orbital size α is subsequently obtained within the framework of EDABI method (*cf.* Section 2.1).

A.2 Microscopic parameters

The scalar product of the Gaussian contractions (A.1) localized on the lattice sites i and j (the *overlap integral*) is given by

$$S_{ij} = \sum_{ab} \beta_a\beta_b \langle \Psi_i^{(a)} | \Psi_j^{(b)} \rangle \equiv \sum_{ab} \beta_a\beta_b S_{ab}(R_{ij}), \tag{A.7}$$

where $R_{ij} = |\mathbf{R}_j - \mathbf{R}_i|$, and

$$S_{ab}(R) = \left(\frac{2\Gamma_a\Gamma_b}{\Gamma_a^2+\Gamma_b^2}\right)^{3/2} e^{-\frac{\Gamma_a^2\Gamma_b^2}{\Gamma_a^2+\Gamma_b^2}R^2} = \left(\frac{g_{ab}}{G_{ab}}\right)^3 e^{-\frac{1}{2}(g_{ab}/G_{ab})^2R^2}, \tag{A.8}$$

as we define

$$g_{ab} = (\Gamma_a\Gamma_b)^{1/2}, \quad \text{and} \quad G_{ab} = \left(\frac{\Gamma_a^2+\Gamma_b^2}{2}\right)^{1/2}. \tag{A.9}$$

Here and in the following formulas we do not introduce explicitly the inverse orbital size α, as in Eq. (A.6), since $\alpha \neq 1$ corresponds to simple rescaling of the coefficient $\Gamma_a \to \alpha\Gamma_a$. Having estimated the scalar product S_{ij} in Eq. (A.7), we can define next the Wannier basis composed of the Gaussian–type orbitals by applying Eqs. (3.9), (3.10) and (3.11) for 1D chain (*note* that $S_{ij} \equiv S_{|i-j|}$) or the corresponding formulas for the systems of other geometries.

Analogously, the *hopping integral* for the sites i and j can be expressed (in the atomic basis) as follows

$$t'_{ij} = \sum_{ab} \beta_a\beta_b \langle \Psi_i^{(a)} | T | \Psi_i^{(b)} \rangle, \tag{A.10}$$

where the single–particle operator $T(\mathbf{r})$ is defined by Eq. (3.4), the matrix elements $\langle \Psi_i^{(a)} | T | \Psi_i^{(b)} \rangle$ are given by

$$\langle \Psi_i^{(a)} | T | \Psi_i^{(b)} \rangle = \tau_0 + \sum_k \tau_{ikj}, \tag{A.11}$$

where we define

$$\tau_0 = \langle \Psi_i^{(a)} | -\nabla^2 | \Psi_i^{(b)} \rangle = \left(\frac{g_{ab}}{G_{ab}} \right)^7 \left(3G_{ab}^2 - R_{ij}^2 g_{ab}^4 \right) e^{-\frac{1}{2}(g_{ab}^2/G_{ab})^2 R_{ij}^2} \tag{A.12}$$

and

$$\tau_{ikj} = \langle \Psi_i^{(a)} | \frac{2}{|\mathbf{r} - \mathbf{R}_k|} | \Psi_i^{(b)} \rangle = -2S_{ab}(R_{ij}) \frac{\mathrm{erf}(\sqrt{2} G_{ab} R_{ikj})}{R_{ikj}}. \tag{A.13}$$

The special function $\mathrm{erf}(x)$ is defined in the standard manner

$$\mathrm{erf}(x) = \frac{2}{\sqrt{\pi}} \int_0^x e^{-t^2} dt; \tag{A.14}$$

we also introduce the three–site distance

$$R_{ikj} = \left| \mathbf{R}_k - \left[\mathbf{R}_i + \frac{\mathbf{R}_{ij}}{1 + (\Gamma_a/\Gamma_b)^2} \right] \right|. \tag{A.15}$$

If $R_{ikj} = 0$, one can avoid the singularity by using the limit

$$\lim_{x \to 0} \frac{\mathrm{erf}(ax)}{x} = \frac{2a}{\sqrt{\pi}}, \tag{A.16}$$

that comes obviously from the definition of $\mathrm{erf}(x)$ in Eq. (A.14). Thus, in the case when $i = j = k$ Eq. (A.11) reduces to the form

$$\langle \Psi_i^{(a)} | T | \Psi_i^{(b)} \rangle = 3 \frac{g_{ab}^7}{G_{ab}^5} - \frac{2^{5/2} g_{ab}^3}{\pi^{1/2} G_{ab}^2},$$

that is exactly equal to Eq. (A.3) for the on–site term.

The most important feature of the Gaussian–type orbitals is their capability of calculating the three– and four– site interaction terms in the atomic basis. This is because the product of two Gaussians has still a Gaussian form, so all the integrals reduce to the form of the intersite Coulomb repulsion K. Namely, the generic four–site term

$$V'_{ijkl} = \sum_{abcd} \beta_a \beta_b \beta_c \beta_d \langle \Psi_i^{(a)} \Psi_j^{(b)} | V | \Psi_k^{(c)} \Psi_l^{(d)} \rangle \tag{A.17}$$

consists of the elements

$$\langle \Psi_i^{(a)} \Psi_j^{(b)} | V | \Psi_k^{(c)} \Psi_l^{(d)} \rangle = S_{ac}(R_{ik}) S_{bd}(R_{jl}) K(R_{ijkl}, G_{ac}, G_{bd}), \tag{A.18}$$

where the four–site distance

$$R_{ijkl} = \left| \left[\mathbf{R}_i + \frac{\mathbf{R}_{ik}}{1 + (\Gamma_a/\Gamma_c)^2} \right] - \left[\mathbf{R}_j + \frac{\mathbf{R}_{jl}}{1 + (\Gamma_b/\Gamma_d)^2} \right] \right|, \tag{A.19}$$

and the Coulomb integral for the Gaussians of the inverse sizes Γ_1 and Γ_2, centered at the distance R, is equal to

$$K(R, \Gamma_1, \Gamma_2) = \frac{2}{R} \mathrm{erf} \left[\frac{\sqrt{2}\Gamma_1\Gamma_2 R}{(\Gamma_1^2 + \Gamma_2^2)^{1/1}} \right] = \frac{2}{R} \mathrm{erf}(g_{12}^2 R / G_{12}). \tag{A.20}$$

The compact form of Eq. (A.20) was achieved with the help of the variables similar to those defined in Eq. (A.9), namely

$$g_{12} = (\Gamma_1\Gamma_2)^{1/2}, \quad \text{and} \quad G_{12} = \left(\frac{\Gamma_1^2 + \Gamma_2^2}{2} \right)^{1/2}.$$

When $R_{ijkl} = 0$ we again use the limit (A.16), obtaining e.g. the on–site Hubbard term in the form

$$U_{abcd} = \langle \Psi_i^{(a)} \Psi_i^{(b)} | V | \Psi_i^{(c)} \Psi_i^{(d)} \rangle = \frac{4}{\pi^{1/2}} \left(\frac{g_{ac} g_{bd}}{G_{ac} G_{bd}} \right)^3 \frac{g_{12}^2}{G_{12}}.$$

This completes our review of the Gaussian–type orbital approach, since one can substitute the one–particle elements in the atomic basis, defined by Eqs. (A.10–A.15) to an appropriate formula in Wannier basis (i.e. to Eqs. (3.12) and (3.13) in the case of 1D chain), and proceed analogously with the two–particle elements given by Eqs. (A.17–A.20).

Appendix B

Slater–type orbitals

In this Appendix we have collected the expressions for the matrix elements in the atomic (*primed*) basis composed of the Slater $1s$ functions defined by

$$\Psi_i(\mathbf{r}) = \left(\frac{\alpha^3}{\pi}\right)^{1/2} e^{-\alpha|\mathbf{r}-\mathbf{R}_i|}, \tag{B.1}$$

where the inverse orbital size α is the variational parameter adjusted to reach the ground–state energy minimum within the EDABI method (*cf.* Section 2.1). This Appendix follows the previous formulation of our method for the Slater–type orbitals (Spałek et al., 2000; Rycerz and Spałek, 2002).

For the sake of completeness, we start from the overlap integral of the Slater orbitals localized on the site i and j

$$S_{ij} = \langle\Psi_i|\Psi_j\rangle = e^{\alpha R_{ij}}\left(1 + \alpha R_{ij} + \frac{1}{3}\alpha^2 R_{ij}^2\right), \tag{B.2}$$

where $R_{ij} = |\mathbf{R}_i - \mathbf{R}_j|$. The above expression is used to determine the coefficients β and γ in the expansion (3.9) via Eqs. (3.10) and (3.11); one should note that for 1D chain $S_{ij} \equiv S_{|i-j|}$. Hence, the Wannier basis composed of Slater–type functions is constructed and we can estimate the microscopic parameters.

B.1 Single–particle elements

The expansion (3.9) leads to two–site terms in the atomic energy ϵ_a and to and three–site terms in the hopping integrals. Namely, in the expressions (3.12) and (3.13) the atomic energy ϵ'_a is

$$\epsilon'_a = \langle\Psi_i|T|\Psi_i\rangle = \alpha^2 - 2\alpha + \sum_{j\neq i}\left[-\frac{2}{R_{ij}} + e^{-2\alpha R_{ij}}\left(2\alpha + \frac{2}{R_{ij}}\right)\right], \tag{B.3}$$

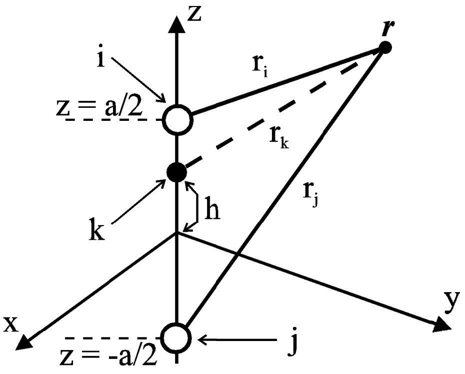

FIGURE B.1: Configuration of coordinates used to calculated the three–site terms τ_{ikj} in the hopping integral t'_{ij} for the electron transfer $j \to i$ induced by the Coulomb potential of k–th ion.

where the single–particle operator $T(\mathbf{r})$ is given by Eq. (3.4). Note the appearance of the long–range part $\sim (-2/R_{ij})$, as one would have in the classical limit.

The evaluation of t'_{ij} is not so straightforward as one can see from the expression

$$t'_{ij} = \langle \Psi_i | - \nabla^2 - \sum_k \frac{2}{r_k} | \Psi_j \rangle = \tau_0 + \sum_k \tau_{ikj}, \tag{B.4}$$

where $r_k = |\mathbf{r} - \mathbf{R}_k|$, τ_0 represent the simple part and τ_{ijk} is the three–site part. The part τ_0 is easy to calculate; since we have

$$\tau_0 = \langle \Psi_i | - \nabla^2 \, | \Psi_j \rangle = \alpha^2 e^{-\alpha R_{ij}} \left(1 + \alpha R_{ij} - \frac{1}{3} \alpha^2 R_{ij}^2 \right). \tag{B.5}$$

The three–site part is more cumbersome, as it reduces to the following integral expression

$$\tau_{ikj} = - \int d^3 r \Psi^*(\mathbf{r}_i) \frac{2}{r_k} \Psi(\mathbf{r}_j) = - \frac{2\alpha^3}{\pi} \int d^3 r \frac{e^{-\alpha(r_i + r_j)}}{r_k}. \tag{B.6}$$

To calculate the integral we introduce the spheroidal coordinates (λ, μ),

$$a\lambda = r_i + r_j, \quad a\mu = r_i - r_j, \quad d^3 r = \frac{\pi a^3}{4} (\lambda^2 - \mu^2) d\lambda d\mu, \tag{B.7}$$

where $a \equiv R_{ij}$. The regimes for λ and μ are: $1 \leqslant \lambda < \infty$, $-1 \leqslant \mu \leqslant 1$. This transformation leads to the following expression for r_k:

$$r_k = \sqrt{\frac{a^2}{4} (\lambda^2 - 1)(1 - \mu^2) + \left(\lambda \mu \frac{a}{2} - h \right)}, \tag{B.8}$$

where h is the z-coordinate of the middle point of the Coulomb potential well caused by the k–th ion (*cf.* Figure B.1). Integrating with respect to μ we obtain

$$\tau_{ikj} = -\alpha^3 a^2 \int_1^\infty d\lambda \exp(-\alpha a \lambda) \left\{ \left[\lambda^2 \left(1 + (2h/a)^2 \right) + b/2 \right] \times \right.$$

$$\times \log \frac{(2h\lambda/a-1)-\sqrt{(2h\lambda/a-1)^2+b}}{(2h\lambda/a+1)-\sqrt{(2h\lambda/a+1)^2+b}} +$$
$$+(3h\lambda/a-1/2)\sqrt{(2h\lambda/a+1)^2+b}$$
$$\left. -(3h\lambda/a+1/2)\sqrt{(2h\lambda/a-1)^2+b}\right\}, \tag{B.9}$$

where $b = (\lambda^2 - 1)\,[1-(2h/a)^2]$. This integral simplifies substantially if either $k = i$ or $k = j$, i.e. for $h = \pm a/2$. Then, taking simple limiting expression we obtain that

$$\tau_{ijk} = -2\alpha^3 a^2 \int_1^\infty d\lambda \lambda e^{-\alpha a \lambda} = -2\alpha e^{-\alpha R_{ij}}(\alpha R_{ij} + 1). \tag{B.10}$$

Substituting (B.10) to (B.4) we obtain e.g. the hopping integral for H_2 molecule (Spałek et al., 2000).

In the general case, we have to evaluate the integral (B.9) numerically. For this purpose, one makes the change of variable $\lambda = 1/t$ to integrate over the finite interval $0 < t < 1$ (one has to use a variable summation step, since the integrand is logarithmically divergent at $t = 1$). When using the Simpson method (Burden and Faires, 1985) one has to evaluate the integrand in $300 \div 400$ points to achieve the accuracy 10^{-6} Ry; this procedure requires a negligible time compared to that required to determine the ground state energy.

B.2 Interaction parameters

Two particle elements $V'_{ijkl} = \langle \Psi_i \Psi_j | V | \Psi_k \Psi_l \rangle$ can be evaluate analytically for the Slater–type orbitals only in the special cases of the *two–site* terms, as listed below (Slater, 1963)

$$V'_{iiii} \equiv U' = \frac{5}{4}\alpha, \tag{B.11}$$

$$V'_{ijij} \equiv K' = \frac{2}{R} - \alpha e^{-2\alpha R}\left(\frac{2}{\alpha R} + \frac{3}{2}\alpha R + \frac{1}{3}\alpha^2 R^2 + \frac{11}{4}\right), \tag{B.12}$$

$$V'_{iiij} \equiv V' = \alpha\left[e^{-\alpha R}\left(2\alpha R + \frac{1}{4} + \frac{5}{8\alpha R}\right) - \frac{1}{4}e^{-3\alpha R}\left(1 + \frac{5}{2\alpha R}\right)\right], \tag{B.13}$$

$$V'_{ijji} = V'_{iijj} \equiv J' = \frac{12}{5R}\left[S^2 C + S^2 \log \alpha R - 2SS'\mathrm{Ei}(-2\alpha R)\right.$$
$$\left. + (S')^2 \mathrm{Ei}(-4\alpha R)\right] + \alpha e^{-2\alpha R}\left(\frac{5}{4} - \frac{23}{10}\alpha R - \frac{6}{5}\alpha^2 R^2 - \frac{2}{15}\alpha^3 R^3\right); \tag{B.14}$$

where R is the distance between two different of the sites i, j, k, and l,

$$S = e^{-\alpha R}\left(1 + \alpha R + \frac{1}{3}\alpha^2 R^2\right), \qquad S' = e^{\alpha R}\left(1 - \alpha R + \frac{1}{3}\alpha^2 R^2\right), \tag{B.15}$$

$$C = 0.57722 \text{ is the Euler constant,} \qquad \mathrm{Ei}(-x) = -\int_x^\infty \frac{e^{-t}}{t}dt. \tag{B.16}$$

In other situation, when consider the three– or four–site terms among V_{ijkl}, the numerical integrations becomes so computationally extensive, that an application of the Gaussian–type orbitals (*cf.* Appendix A) is much efficient. An interesting approach, combining the evaluation of all possible integrals in the Slater basis and only the three– and four– site interaction terms in Gaussian, have been recently proposed (Kurzyk et al., 2003). In such a method one should, however, check carefully for the convergence with the number of Gaussians to control the errors, whereas when applying entirely the Gaussian–type orbitals, as in this thesis, one stays in the framework of variational methods that guarantee the resulting ground–state energy to be higher than or equal to its exact value.

Bibliography

Aebisher, C. (2001). *Phys. Rev. Lett.* **86**: 468.

Ahn, J. R., Kim, Y. J., Lee, H. S., Hwang, C. C., Kim, B. S. and Yeom, H. W. (2002). *Phys. Rev. B* **66**: 153403.

Anisimov, V. I., Potaryaev, A. I., Korotin, M. A., Anokhin, A. O. and Kotliar, G. (1997). *J. Phys. Condensed Matter* **9**: 7359.

Arachea, L. and Aligia, A. A. (1994). *Phys. Rev. Lett.* **73**: 2240.

Assaad, F. F. (2002). *in* J. Grotendorst, D. Marx and A. Muramatsu (eds), *Quantum Simulations of Complex Many–Body Systems: From Theory to Algorithms*, Vol. 10 of *NIC Series*, John von Neuman Institute for Computing, p. 99. Available online at http://www.fz-juelich.de/nic-series/.

Assaad, F. F., Hanke, W. and Scalapino, D. J. (1994). *Phys. Rev. B* **50**: 12835.

Assaad, F. F. and Würtz, D. (1991). *Phys. Rev. B* **44**: 2681.

Baeriswyl, D., Carmelo, J. and Luther, A. (1986). *Phys. Rev. B* **33**: 7247.

Bahn, S. R. and Jacobsen, W. (2001). *Phys. Rev. Lett.* **87**: 266101.

Barma, M. and Shastry, B. S. (1978). *Phys. Rev. B* **18**: 3351.

Blankenbecler, R., Scalapino, D. J. and Sugar, R. L. (1981). *Phys. Rev. D* **24**: 2278.

Burden, R. L. and Faires, J. D. (1985). *Numerical Analysis*, Prindle, Weber and Schmidt, Boston.

Capponi, S. and Assaad, F. F. (2001). *Phys. Rev. B* **63**: 155113.

Capponi, S., Poilblanc, D. and Giamarchi, T. (2000). *Phys. Rev. B* **61**: 13410.

Ceperley, D. and Alder, B. (1986). *Phys. Rev. B* **36**: 2092.

Chacham, H. and Louie, S. G. (1991). *Phys. Rev. Lett.* **66**: 64.

Dagotto, E. (1994). *Rev. Mod. Phys.* **66**: 763.

Dardel, B., Malterre, D., Grioni, M., Weibel, P., Baer, Y., Voit, J. and Jérôme (1992). *Europhys. Lett.* **24**: 687.

Daul, S. and Noack, R. M. (2000). *Phys. Rev. B* **61**: 1646.

de Boer, J. and Schadschneider, A. (1995). *Phys. Rev. Lett.* **75**: 4298.

Dongarra, J. J., Duff, I. S. and van der Vorst, H. A. (1998). *Numerical Linear Algebra for High–Performance Computers*, SIAM, Philadelphia.

Emery, V. J. (1979). *in* J. Devreese, R. Evrand and V. van Doren (eds), *Highly Conducting One–Dimensional Solids*, Plenum Press, New York.

Evertz, H. G., Lana, G. and Marcu, M. (1993). *Phys. Rev. Lett.* **70**: 875.

Fabrizio, M. (1996). *Phys. Rev. B* **54**: 10054.

Fahy, S. and Hammann, D. R. (1990). *Phys. Rev. Lett.* **65**: 3437.

Fisher, M. P. A. and Glazman, L. I. (1997). *in* L. L. Sohn, L. P. Kouwenhoven and G. Schön (eds), *Mesoscopic Electron Transport*, Vol. 345 of *NATO ASI Ser. E*, Kluwer Academic, Dortrecht, p. 331.

Fock, V. A. (1957). *Selected Papers on Quantum Field Theory (in Russian)*, Published by Leningrad University, Leningrad.

Fourcade, B. and Sproken, G. (1984). *Phys. Rev. B* **29**: 5096.

Frank, S. et al. (1998). *Science* **280**: 1744.

Fulde, P. (1991). *Electron Correlations in Molecules and Solids*, Vol. 100 of *Springer Series in Solid–State Sciences*, Springer Vg., Berlin/Heidelberg.

Fye, R. M., Martins, M. J. and Scalapino, D. J. (1991). *Phys. Rev. B* **44**: 6909.

Gagliano, E. and Balseiro, C. (1987). *Phys. Rev. Lett.* **59**: 2999.

Ge, F., Prasad, C., Andresen, A., Bird, J. P., Ferry, D. K., Lin, L. et al. (2000). *Ann. Phys. (Leipzig)* **9**: 1.

Georges, A., Kotliar, G., Krauth, W. and Rozenberg, M. J. (1996). *Rev. Mod. Phys.* **68**: 13.

Góra, D., Rościszewski, K. and Oleś, A. M. (1998). *J. Phys. Condensed Matter* **10**: 4755.

Graham, R. L., Knuth, D. E. and Patashnik, O. (1994). *Concrete Mathematics. A Foundation for Computer Science*, Addison–Wesley, Reading, Massachusetts, chapter 3.4. *Note* that the formal definition of modulo division leads to different results for negative operands than the corresponding operators in popular programing languages (e.g. % in C).

Ha, Z. N. C. (1996). *Quantum Many-Body Systems in One Dimension*, Vol. 12 of *Series on Advances in Statistical Mechanics*, World Scientific, Singapore.

Haldane, F. D. M. (1981). *J. Phys. C: Solid State Phys.* **14**: 2585.

Haydock, R., Heine, V. and Kelly, M. J. (1972). *J. Phys. C* **5**: 2845.

Hemley, R. J. and Ashcroft, N. W. (1998). *Psysics Today* **8**: 26.

Hemley, R. J. and Mao, H. K. (1989). *Phys. Rev. Lett.* **63**: 1393.

Hemley, R. J. and Mao, H. K. (1990). *Science* **249**: 391.

Hirsch, J. E. and Fye, R. M. (1986). *Phys. Rev. Lett.* **56**: 2521.

Hirsch, J. E., Scalapino, D. J., Sugar, R. L. and Blankenbecler, R. (1981). *Phys. Rev. B* **26**: 5033.

Hubbard, J. (1963). *Proc. R. Soc. (London) A* **276**: 238.

Hubbard, J. (1978). *Phys. Rev. B* **17**: 494.

Jacak, L., Hawrylak, P. and Wójs, A. (1998). *Quantum Dots*, Springer Vg., Berlin.

Jackson, J. D. (1975). *Classical Electrodynamics*, John Willey and Sons, New York.

Jaklič, J. and Prelovšek, P. (1994). *Phys. Rev. B* **49**: 5065.

Jaklič, J. and Prelovšek, P. (2000). *Adv. Phys.* **49**: 1.

Jarrel, M. and Gubernatis, J. E. (1996). *Physics Reports* **269**: 133.

Jarrell, M. (1992). *Phys. Rev. Lett.* **69**: 168.

Jullien, R. and Martin, R. M. (1982). *Phys. Rev. B* **26**: 6173.

Kohn, W. (1959). *Phys. Rev.* **115**: 809.

Kohn, W. (1964). *Phys. Rev.* **133**: A171.

Kondo, J. and Yamai, K. (1977). *J. Phys. Soc. Japan* **43**: 424.

Korbel, P., Wójcik, W., Klejnberg, A., Spałek, J., Acquarone, M. and Lavagna, M. (2003). *Euro. Phys. J. B* **32**: 315.

Krans, J. M., van Ruitenbeek, J. M., Fisun, V. V., Yanson, I. K. and de Jongh, L. J. (1995). *Nature (London)* **375**: 767.

Kurzyk, J., Spałek, J., Wójcik, W. and Rycerz, A. (2003). Unpublished.

Lanczos, C. (1950). *J. Res. Nat. Bur. Stand.* **45**: 255.

Landau, L. D. (1957). *Sov. Phys.–JETP* **3**: 101.

Landau, L. D. (1959). *Sov. Phys.–JETP* **8**: 70.

Lieb, E. H. and Wu, F. Y. (1968). *Phys. Rev. Lett.* **20**: 1445.

Lin, H. Q. and Hirsch, J. E. (1986). *Phys. Rev. B* **38**: 8155.

Luttinger, J. M. (1960). *Phys. Rev.* **119**: 1153.

Luttinger, J. M. (1963). *J. Math. Phys.* **4**: 1154.

Mahan, G. D. (1990). *Many–Particle Physics*, Plenum Press, New York.

Maldague, P. (1977). *Phys. Rev.* **16**: 2437.

Mao, H. K. and Hemley, R. J. (1989). *Science* **244**: 1462.

Mao, H. K. and Hemley, R. J. (1994). *Rev. Mod. Phys.* **66**: 671.

Mattis, D. C. and Lieb, E. H. (1963). *J. Math. Phys.* **6**.

Michielsen, K., De Raedt, H. and Schneider, T. (1992). *Phys. Rev. Lett.* **68**: 1410.

Millis, J. A. and Coppersmith, S. N. (1990). *Phys. Rev. B* **42**: 10807.

Mintmire, J. W., Dunplap, B. I. and White, C. T. (1992). *Phys. Rev. Lett.* **68**: 631.

Nekrasov, I. A., Held, K., Blümer, N., Potaryev, A. I., Anisimov, V. I. and Vollhardt, D. (2000). *Euro. Phys. J. B* **18**: 55.

Nellis, W. J. (2000). *Scietific American* **5**: 84.

Nozières, P. (1964). *Interacting Fermi Systems*, Benjamin, New York.

Ochnishi, H., Kondo, Y. and Takayanagi, K. (1998). *Nature (London)* **395**: 780.

Ogata, M. and Shiba, H. (1990). *Phys. Rev. B* **41**: 2326. For Hubbard model in the large–U limit charge degrees of freedom of the Bethe–ansatz wavefunction are expressed as a Slater determinant of spinless fermions, while its spin degrees of freedom are equivalent to $S = \frac{1}{2}$ Heisenberg model, so $N_{\mathrm{st}} \propto 2^N$.

Ovchinnikov, A. A. (1993). *Mod. Phys. Lett. B* **7**: 1397.

Pettifor, D. G. and Weaire, D. L. (eds) (1985). *The Recursion Methods and Its Applications*, Vol. 58 of *Springer Series in Solid–State Sciences*, Springer, Berlin/Heidelberg.

Press, W. H., Teukolsky, S. A., Vetterling, W. T. and Flannery, B. P. (1992). *Numerical Recipes in C*, Cambrige University Press, Cambridge.

Resta, R. and Sorella, S. (1999). *Phys. Rev. Lett.* **82**: 370.

Rościszewski, K. and Oleś, A. M. (1993). *J. Phys. Condensed Matter* **5**: 7289.

Rycerz, A. (2000). *M. Sc. Thesis*, Jagiellonian University, Kraków.

Rycerz, A. and Spałek, J. (2001). *Phys. Rev. B* **63**: 073101.

Rycerz, A. and Spałek, J. (2002). *Phys. Rev. B* **65**: 035110.

Rycerz, A. and Spałek, J. (2003a). *Acta Phys. Polon. B* **34**: 655.

Rycerz, A. and Spałek, J. (2003b). *in* F. Mancini (ed.), *Lectures on the Physics of Highly Correlated Electron Systems VII*, AIP Conf. Proc. To be published.

Rycerz, A., Spałek, J., Podsiadły, R. and Wójcik, W. (2002). *in* F. Mancini (ed.), *Lectures on the Physics of Highly Correlated Electron Systems VI*, Vol. 629, AIP Conf. Proc., p. 213.

Schrödinger, E. (1926). *Ann. Phys.* **79**: 361. Here we utilize the same variational procedure for the effective (renormalized) single-particle Hamiltonian.

Schulz, H. J. (1993). *Phys. Rev. Lett.* **71**: 1864.

Sekiyama, A., Fujimori, J., Aonuma, S., Sawa, H. and Kato, R. (1995). *Phys. Rev. B* **51**: 13899(R).

Shastry, B. S. and Sutherland, B. (1990). *Phys. Rev. Lett.* **65**: 243.

Shavitt, R. A. (1977). *in* H. Schaeffer (ed.), *Methods of Electronic Structure Theory*, Plenum Press, New York.

Slater, J. C. (1963). *Quantum Theory of Molecules and Solids*, Vol. 1, McGraw–Hill, New York.

Smit, R. H. M., Untiedt, C., Yanson, A. I. and van Ruitenbeek, J. M. (2001). *Phys. Rev. Lett.* **87**: 266102.

Solyom, J. (1979). *Adv. Phys.* **28**: 201.

Sorella, S. (2001). *Phys. Rev. B* **64**: 024512.

Sorella, S., Parola, A., Parrinello, M. and Tosatti, E. (1990). *Europhys. Lett.* **12**: 721.

Spałek, J., Görlich, E. M., Rycerz, A. and Zahorbeński, R. (2003). *Renormalized wave equation and multiparticle states: A combined second– and first–quantization approach to interacting fermions and bosons*. Unpublished.

Spałek, J., Görlich, E. M., Rycerz, A., Zahorbeński, R., Podsiadły, R. and Wójcik, W. (2003). *NATO Advanced Research Workshop: Concepts in Electron Correlations*, Kluwer Academic, Dortrecht. In press.

Spałek, J., Oleś, A. M. and Chao, K. A. (1981). *Phys. Status Solidi (b)* **108**: 329.

Spałek, J., Podsiadły, R., Wójcik, W. and Rycerz, A. (2000). *Phys. Rev. B* **61**: 15676.

Spałek, J. and Rycerz, A. (2001). *Phys. Rev. B* **64**: 161105(R).

Strack, R. and Vollhardt, D. (1993). *Phys. Rev. Lett.* **70**: 2637.

Tomonaga, S. (1950). *Prog. Theor. Phys.* **5**: 544.

Tsukamoto, S. and Kikuji, H. (2002). *Phys. Rev. B* **66**: 161402(R).

van der Linden, W. (1995). *Applied Physics A* **60**: 155.

Viswanath, V. S. and Müller, G. (1990). *J. Appl. Phys.* **67**: 5486.

Viswanath, V. S. and Müller, G. (1991). *J. Appl. Phys.* **70**: 6178.

Voit, J. (1995). *Rep. Prog. Phys.* **57**: 977.

White, S. R. (1998). *Physics Reports* **301**: 187.

Wigner, E. and Huntington, H. B. (1935). *J. Chem. Phys.* **3**: 764.

Yanson, A. I., Rubio Bollinger, G., van der Brom, H. E., Agraït, N. and van Ruitenbeek, J. M. (1998). *Nature (London)* **395**: 783.

Yanson, A. I., Yanson, I. K. and van Ruitenbeek, J. M. (1999). *Nature (London)* **400**: 144.

Zeiner, R., Dirl, R. and Davies, B. L. (1998). *Phys. Rev. B* **58**: 7681.